MECHANISTIC INVESTIGATION OF CARBON DIOXIDE HYDROGENATION ON BIMETALLIC IRON-COBALT SURFACES BY DENSITY FUNCTIONAL THEORY

A Thesis Submitted to
the Graduate School of Engineering and Science of
İzmir Institute of Technology
in Partial Fulfillment of Requirements for the Degree of

MASTER OF SCIENCE

in Chemical Engineering

by
Dilan TUNÇER

December, 2023
İZMİR

We approve the thesis of **Dilan TUNÇER**

Examining Committee Members:

Assist. Prof. Dr. Ali Can KIZILKAYA
Department of Chemical Engineering, Izmir Institute of Technology

Prof. Dr. Erol ŞEKER
Department of the Chemical Engineering, Izmir Institute of Technology

Assoc. Prof. Dr. Murat Oluş ÖZBEK
Department of the Chemical Engineering, Gebze Technical University

8 December 2023

Assist. Prof. Dr. Ali Can KIZILKAYA
Supervisor, Department of Chemical Engineering, Izmir Institute of Technology

Prof. Dr. Aysun SOFUOĞLU
Head of the Department of Chemical Engineering

Prof. Dr. Mehtap EANES
Dean of the Graduate School of Engineering and Sciences

ACKNOWLEDGEMENTS

First of all, I would like to express my sincere gratitude to Assist. Prof. Dr. Ali Can KIZILKAYA for his mentorship and our long conversations about academics and life, which have further ignited my passion for science and changed my perspective on life.

I would like to thank to TÜBİTAK ULAKBİM for providing computational time and scholar for all my master's process.

I want to express my gratitude to Özüm ÖZBEK for her support, invaluable friendship, and the countless moments we have shared together. My heartfelt thanks to Yağmur ÇETİN for the unforgettable and enjoyable days, as well as for believing in and supporting my goals. I also appreciate Simge KOSTİK for her support and friendship and Rafid Salah Jasim GERTANİ for making every task enjoyable and for all the support he provides from a distance. I would also like to thank to my friends Gasham HAJIYEV, Rüzgar RÜZGAROĞLU, Hicran SUBAŞI, Zehra KOCATAŞ and to many others that I could not mention here for sharing these moments with me.

I am grateful to my sister and brother, Dilay and Erhan TUNÇER, who have always supported me, made their presence felt and shared in all of my feelings, and for their deep trust and faith in me.

Finally, to my mother and father, who I know are somehow proud of what I do and the who I am, and whom I always feel by my side, since they set a great guide for me in my approach to life and taught me to stand on my feet in the face of all kinds of difficulties.

ABSTRACT

MECHANISTIC INVESTIGATION OF CARBON DIOXIDE HYDROGENATION ON BIMETALLIC IRON-COBALT SURFACES BY DENSITY FUNCTIONAL THEORY

Climate change due to the increase in global CO_2 emissions has intensified the importance of not only reducing CO_2 production but also utilizing it for the production of chemicals and fuels through catalytic CO_2 conversion. The rational design of active and selective catalysts has critical importance towards the industrial application of these processes. In this thesis, a computational study was performed to investigate the mechanism of CO_2 hydrogenation for producing of C_1 hydrocarbons and gain an atomic-level understanding of the structure-activity relationships on the (111) surface of FeCo bimetallic catalysts, to guide the design of bimetallic catalysts based on first principles.

In this thesis, the kinetics of elementary reactions of CO_2 hydrogenation to C_1 hydrocarbons on fcc-Co(111) and Fe-doped Co(111) [FeCo(111)] surfaces were compared using density functional theory (DFT). Our investigation revealed that the incorporation of Fe on the Co(111) surface slightly decreased the overall reaction rate despite promoting CO_2 activation. The FeCo(111) surface slows down hydrogenation reactions due to the lower atomic H coverages and higher activation energies, attributed to the Lewis basic character of Fe atoms. Fe-doping primarily inhibits the removal of oxygen from cobalt surfaces. Consequently, Fe doping is expected to promote the formation of oxidic phases on the bimetallic FeCo catalysts during CO_2 hydrogenation.

ÖZET

BİMETALİK DEMİR-KOBALT YÜZEYLERİNDE KARBONDİOKSİT HİDROJENASYONUNUN YOĞUNLUK FONKSİYONEL TEORİSİ'NE GÖRE MEKANİSTİK İNCELENMESİ

Küresel CO_2 emisyonundaki artışa bağlı olarak iklim değişikliği, yalnızca CO_2 üretiminin azaltılmasındaki önemi artırmakla kalmadı, aynı zamanda katalitik CO_2 dönüşümü yoluyla kimyasalların ve yakıtların üretiminde kullanılmasının önemini de artırdı. Aktif ve seçici katalizörlerin rasyonel tasarımı, bu proseslerin endüstriyel uygulamalarına yönelik kritik öneme sahiptir. Bu tezde, C_1 hidrokarbonların üretimi için CO_2 hidrojenasyonunun mekanizmasını araştırmak ve FeCo bimetalik katalizörlerin (111) yüzeyindeki yapı-aktivite ilişkisinin atomik düzeyde anlaşılmasını sağlamak ve tasarıma rehberlik etmek için ilk prensiplere dayalı hesaplamalı bir çalışma yapıldı.

Bu tezde, fcc-Co(111) ve Fe-katkılı Co(111) [FeCo(111)] yüzeyleri üzerinde CO_2 hidrojenasyonunun C_1 hidrokarbonlara verdiği temel reaksiyonların kinetiği, yoğunluk fonksiyonel teorisi (YFT) kullanılarak karşılaştırıldı. Araştırmamız Fe'nin Co(111) yüzeyine eklenmesi ile birlikte, CO_2 aktivasyonunu desteklemesine rağmen genel reaksiyon hızını hafifçe azalttığını ortaya çıkardı. 1 ML Fe-katkılı Co(111) yüzeyinin daha düşük atomik H kapsamaları ve daha yüksek aktivasyon bariyerleri nedeniyle hidrojenasyon reaksiyonlarını engellemesi Fe'nin Lewis bazik karakterine atfedilmiştir. Fe'in katılması temel olarak kobalt yüzeylerinden oksijenin ayrılmasını engellemektedir. Bu nedenle, Fe katkısının, CO_2 hidrojenasyonu sırasında bimetalik FeCo katalizörleri üzerinde oksidik fazların oluşumunu teşvik etmesi beklenmektedir.

TABLE OF CONTENTS

LIST OF FIGURES viii

LIST OF TABLES xii

CHAPTER 1. INTRODUCTION 1

1.1. Climate Change and CO_2 Emissions 1

1.2. Challenges in CO_2 Conversion 2

1.3. Fundemantals of Catalysis 4

1.4. Catalysis for CO_2 Conversion 6

1.4.1. Heterogeneous Catalysts for CO and CO_2 hydrogenation 8

1.5. Fischer-Tropsch Synthesis 12

1.6. CO_2-based Fischer Tropsch Synthesis 15

1.7. CO and CO_2-based FTS Catalysts 16

1.7.1. Iron-based Catalysts 18

1.7.2. Cobalt-based Catalysts 19

1.7.3. Bimetallic Iron-Cobalt Catalysts 20

1.8. Computational Quantum Chemistry and Catalyst Design 21

1.8.1. Basics of Computational Quantum Chemistry 23

1.8.2. Density Functional Theory 24

1.8.3. Kohn-Sham Method 25

1.8.5. Exchange-Correlation Functional 26

1.8.6. Pseudopotentials 27

1.8.7. Climbing Image Nudged Elastic Band (CI-NEB) Method 27

1.8.8. Vibrational Frequency Analysis 28

1.9. Surface Science Approaches in Quantum Chemical Modeling of Catalytic Systems 28

1.10. Objectives of the Study 29

CHAPTER 2. LITERATURE SURVEY 31

2.1. Active Phases and Surface Structures of Bimetallic Fe-Co Catalysts 31

2.2. Catalytic Performance of Fe-Co Catalysts in CO- and CO_2-based FTS 36

CHAPTER 3. COMPUTATIONAL METHODOLOGY 40

3.1. Overview of the Methodology....40
3.2. Preparation and Optimization of the Bulk Structure....42
3.3. Preparation and Optimization of the Slabs....42
3.4. Calculation of the Adsorption Energies and the Kinetic Parameters of Elementary Reactions....43

CHAPTER 4. RESULTS & DISCUSSION....45
4.1. The Selection of the Catalyst Surface Model....45
4.1.1 Effect of Iron Coverage in the Electronic Charge of the Bare FeCo(111) Surface....46
4.1.2. Effect of Iron Coverage on the Adsorption Strength of Surface Species on the FeCo(111) Surface....47
4.2. Adsorption Energies of Surface Species Involved in CO_2 Hydrogenation to C_1 Products on the 1 ML Fe-Doped Co(111) Surface....48
4.3. Elementary Reactions of CO_2-FTS on Co(111) and FeCo(111) Surfaces....54
4.3.1. H_2 Dissociation....55
4.3.2. CO_2 Dissociation....58
4.3.3. CO Dissociation....66
4.3.4. CH_4 Formation....71
4.3.5. CH_3OH Formation....74
4.3.6. H_2O Formation....79
4.4. Bader Charge Analysis....84

CHAPTER 5. CONCLUSIONS....89

REFERENCES....91

APPENDICES
APPENDIX A. GAS PHASE ENERGIES....101
APPENDIX B. COMPARISON OF ADSORPTION ENERGIES ON COBALT SURFACES....102
APPENDIX C. COMPARISON OF ACTIVATION AND REACTION ENERGIES ON COBALT SURFACES....103

LIST OF FIGURES

Figure **Page**

Figure 1. Molecular structure of carbon dioxide. 3
Figure 2. The formation Gibbs free energy of several molecules including CO_2. Adapted from [7]. 3
Figure 3. The reaction energy profiles for catalyzed and non-catalyzed reactions involving CO_2 as the reactant [10]. 4
Figure 4. Catalytic cycle including adsorption, reaction and desorption. Adapted from [12]. 5
Figure 5. Catalytic CO_2 hydrogenation process [16]. 7
Figure 6. The Sabatier principle with the volcano-type plot [22]. 10
Figure 7. 3-Dimensional potential energy surface (PES) with local minimum, global minimum point, first order and high order saddle points [23]. 11
Figure 8. Anderson-Schulz-Flory (ASF) model for FTS [31]. 13
Figure 9. The conceptual representation of FTS in reactor using heterogeneous catalyst, along with the reaction pathways within the reactor. Adapted from [32]. 14
Figure 10. Transition metals and their properties in FTS [37]. 17
Figure 11. Illustration of the bottom-up steps for multiscale catalysis, from computational modeling to reactor-scape applications [52]. 22
Figure 12. The triangular consept of the catalyst design [37]. 22
Figure 13. The Wulff equilibrium shape of hcp cobalt (left) and fcc cobalt (right) as determined through DFT calculations by Liu et al [59]. 29
Figure 14. HRTEM images of pure Fe, pure Co and Fe-Co bimetallic catalysts. 32
Figure 15. HAADF-STEM image of alumina supported FeCo bimetallic catalyst (a), elemental mapping of cobalt (b) and iron (c) catalysts [63]. 33
Figure 16. XRD image of CNT supported FeCo catalyst after LTFT and HTFT [64]. .. 34
Figure 17. The inner structure of a core-shell structure of bimetallic Fe-Co nanoparticle, as obtained using HRTEM [48]. 35
Figure 18.The catalytic performance of bimetallic FeCo catalaysts for CO_2 hydrogenation varies with space velocity (a) and reaction temperature (b), affecting conversion, selectivity and hydrogen distribution. Adapted from [34]. 37

Figure 19. Four steps for computational modeling of catalyst systems. 41
Figure 20. Representative image of bulk fcc cobalt. 42
Figure 21. A 3x3 FeCo(111) unit cell view from the x-direction (a), y-direction (b), and z-direction (c) and the view of gas phase CO molecule in vacuum (d). 43
Figure 22. The side and top views of various FeCo(111) surfaces. 45
Figure 23. The electronic charge of the individual iron atoms on the various iron covered cobalt surfaces and the charges of the topmost two layers specified within parantheses. 46
Figure 24. The adsorption sites investigated on Co(111) and FeCo(111) surfaces. 49
Figure 25. Relative adsorption energies of H, C, O, OH, and CO on top, fcc, and hcp sites of FeCo(111) with respect to their most stable site. 49
Figure 26. Example of the difference in adsorption sites and geometry of CH (a) and HCO (b) intermediates on Co(111) and FeCo(111) surfaces. 50
Figure 27. The most stable adsorption configurations of species on the Co(111) surface. Gray, red, white, blue, and dark red spheres represent C, O, H, Co, and Fe atoms, respectively. 52
Figure 28. The most stable adsorption configurations of species on the FeCo(111) surface. Gray, red, white, blue, and dark red spheres represent C, O, H, Co, and Fe atoms, respectively. 53
Figure 29. Potential energy diagram for H_2 dissociation on Co(111) and FeCo(111) surfaces. 56
Figure 30. IS, TS and FS for the first step of H_2 dissociation on Co(111) and FeCo(111) surfaces. 57
Figure 31. IS, TS and FS for the second step of H_2 dissociation on Co(111) and FeCo(111) surfaces. 57
Figure 32. Potential energy diagram for CO_2 dissociation via the direct mechanism on Co(111) and FeCo(111) surfaces. 59
Figure 33. IS, TS and FS for the CO_2 dissociation via direct mechanism on Co(111) and FeCo(111) surfaces. 60
Figure 34. Potential energy diagram for CO_2 dissociation via carboxylate mechanism on Co(111) and FeCo(111) surfaces. 61
Figure 35. IS, TS and FS for the CO_2 dissociation via carboxylate mechanism on Co(111) and FeCo(111) surfaces. 62

Figure 36. Potential energy diagram for CO_2 dissociation via formate mechanism on Co(111) and FeCo(111) surfaces. 63
Figure 37. IS, TS and FS for the CO_2 dissociation via formate mechanism on Co(111) and FeCo(111) surfaces. 64
Figure 38. Calculated activation energies for reaction pathways of CO_2 dissociation on two surfaces. 65
Figure 39. Potential energy diagram for CO dissociation via direct mechanism on Co(111) and FeCo(111) surfaces. 67
Figure 40. IS, TS and FS for the CO dissociation via direct mechanism on Co(111) and FeCo(111) surfaces. 67
Figure 41. Potential energy diagram for CO_2 dissociation via H-assisted mechanism on Co(111) and FeCo(111) surfaces. 69
Figure 42. IS, TS and FS for the CO dissociation via H-assisted mechanism on Co(111) and FeCo(111) surfaces. 69
Figure 43. Calculated activation energies for reaction pathways of CO dissociation on two surfaces. 70
Figure 44. Potential energy diagram for CH_4 formation on Co(111) and FeCo(111) surfaces. 72
Figure 45. IS, TS and FS for the CH_4 formation on Co(111) and FeCo(111) surfaces. 73
Figure 46. Potential energy diagram for H_3COH formation on Co(111) and FeCo(111) surfaces. 75
Figure 47. IS, TS and FS for the H_2CO formation on Co(111) and FeCo(111) surfaces. 76
Figure 48. IS, TS and FS for the H_3CO formation on Co(111) and FeCo(111) surfaces. 76
Figure 49. IS, TS and FS for the H_3COH formation on Co(111) and FeCo(111) surfaces. 77
Figure 50. Potential energy diagram for formation and dissociation of H_2CO intermediate on Co(111) and FeCo(111) surfaces. 77
Figure 51. IS, TS and FS for the H_2CO dissociation on Co(111) and FeCo(111) surfaces. 78
Figure 52. Potential energy diagram for H_2CO (a) and H_3CO (b) formation via CH_x oxidation on Co(111) and FeCo(111) surfaces. 78

Figure 53. Potential energy diagram for H_2O formation via the hydrogenation of atomic O on Co(111) and FeCo(111) surfaces. 80
Figure 54. IS, TS and FS for the H_2O formation via hydrogenation of atomic oygen on Co(111) and FeCo(111) surfaces. 81
Figure 55. Potential energy diagram for formation H_2O via OH coupling on Co(111) and FeCo(111) surfaces. 82
Figure 56. IS, TS and FS for the H_2O formation via OH coupling on Co(111) and FeCo(111) surfaces. 82
Figure 57. All the modeled reactions and their activation energies for both pure and Fe-doped Co(111) surfaces. 83
Figure 58. The electronic charge distribution of clean and iron doped (1 ML) cobalt surfaces without adsorbate. 86
Figure 59. The electronic charge distribution of clean and 1 ML iron-doped cobalt surfaces with adsorbed CO molecule. 87

LIST OF TABLES

Table **Page**

Table 1. The change in adsorption energies (kJ.mol^{-1}) of key adsorbates (H, O, C, and CO) with the change in iron coverage of the surface. 48

Table 2. Calculated adsorption energies (kJ.mol^{-1}) with adsorption sites of all intermediates in CO_2 hydrogenation on Co(111) and FeCo(111) surfaces. 51

Table 3. The activation and reaction energies (kJ.mol^{-1}) of examined elementary reactions on Co(111) and FeCo(111) surfaces. 55

Table 4. Total Bader charges (q) on adsorbates on Co(111) and FeCo(111) surfaces, along with the calculated difference (Δq). 85

Table 5. Electronic charges on Co(111) vs FeCo(111) surfaces under adsorbate coverages. 88

Table 6. Gas phase energies for various adsorption species. 101

Table 7. Comparison of the adsorption energies (kJ.mol^{-1}) of the adsorbates examined on the surface of the Co(111) catalyst in the literature. 102

Table 8. Comparison of the activation energies (kJ.mol^{-1}) and reaction energies (kJ.mol^{-1}) of the reactions examined on the surface of the Co(111) catalyst in the literature. 103

To my dear brother and sister, for their inifinite support

and making this journey a joy

CHAPTER 1

INTRODUCTION

1.1. Climate Change and CO_2 Emissions

Greenhouse gases, such as carbon dioxide, water vapor, methane and ozone, are known to have harmful environmental effects by trapping the heat of the sun, leading to climate change [1]. For instance, the frequency of massive hurricanes and wildfires is increasing, sea levels are rising more rapidly, and many regions are facing dangerous heatwaves. Among greenhouse gases, carbon dioxide is considered as the most significant greenhouse gas due to its abundance and its long atmospheric life, spanning thousands years, making it a subject of particular concern. Carbon dioxide is released into the atmosphere through various processes, leading to its increasing presence in the atmosphere which threatens the sustainability of world with global warming.

Carbon dioxide is emitted into the environment through multiple sources, including the combustion of fossil fuels, iron and steel industries, cement production, power plants, oil refineries, ammonia and etylene oxide processes leading to a steady increase in its concentration in the atmosphere [2,3]. The utilization of fossil fuels such as natural gas, coal, and oil for urbanization, industrialization and technological progress has resulted in an ongoing increase in atmospheric CO_2 levels. It is worth noting that the demand for fossil fuels is growing along with their use, as a result of the increased demand for energy. In other words, as the energy demand increases, the carbon footprint and its negative impacts increase.

Based on the annual report from the National Oceanic and Atmospheric Administration (NOAA) Global Monitoring Laboratory, the average value for global CO_2 emissions in the atmosphere was recorded as 417.06 ppm in 2022, which was 2.13 ppm higher than the previous year. In the absence of mitigation actions, the concentration of CO_2 in the atmosphere is expected to reach approximately 570 ppm by the end of the 21st

century [4]. Due to the increase in the number of unavoidable CO_2 sources, it is crucial that the level of the CO_2 concentration is reduced in the atmosphere.

To mitigate carbon dioxide emissions, three significant strategies can be employed: CO_2 storage, CO_2 utilization, and CO_2 emissions reduction [3]. In the context of the CO_2 storage strategy, effective carbon dioxide capture relies on the use of advanced capturing and sequestration technologies. Regarding the CO_2 utilization strategy, the conversion of carbon dioxide into valuable chemicals and fuels is performed through chemical reactions. As for the last strategy, CO_2 emissions reduction, it involves the switching from fossil fuels to renewable energy and improving energy efficiency. As the reduction of CO_2 emissions necessitates long-term strategies, the technologies associated with CO_2 storage and its utilization remain relevant and vital nowadays.

Carbon capture and store (CCS) and utilization (CCU) techniques are utilized to reduce the carbon dioxide emissions from the atmosphere with some advanced engineering technologies. CCS has been considered as the effective technology to reduce carbon dioxide emissions, however, due to certain drawbacks, such as long-term liability and limited storage capacity, this technology is not considered to be sufficient for long-term applications [5]. Therefore, instead of storing it, the conversion of carbon dioxide into valuable chemicals and fuels serves the dual purpose of reducing emissions and generating value-added products, effectively addressing two challenges with one solution, often referred to as "hitting two birds with one stone".

1.2. Challenges in CO_2 Conversion

Despite the abundance of CO_2 in the atmosphere, the main challenge in converting this molecule lies in its inertness during reactions. As depicted in Figure 1, the triatomic CO_2 molecule consists of a carbon (C) atom at the center, bound to two oxygen (O) atoms through two linear double bonds, comprised of both σ- and π-bonds. Due to differences in electronegativity, the carbon atom becomes partially positive charged, while the oxygen atoms become negatively charged. This polarity contributes to the Lewis acidic and basic behavior of CO_2 molecule. Additionally, CO_2 is a non-polar molecule due to its linear geometry and opposing dipole moments [6].

Figure 1. Molecular structure of carbon dioxide.

The formation Gibbs free energy of several molecules is given in Figure 2. This figure demonstrates that CO_2 is highly stable among the other molecules and, requiring relatively more energy (ΔG_f^0 = -394 kJ.mol^{-1}) to break its bonds. This stability is often misinterpreted as if carbon dioxide is "unreactive", suggesting that any chemical conversion of it would inevitably require a substantial input of energy.

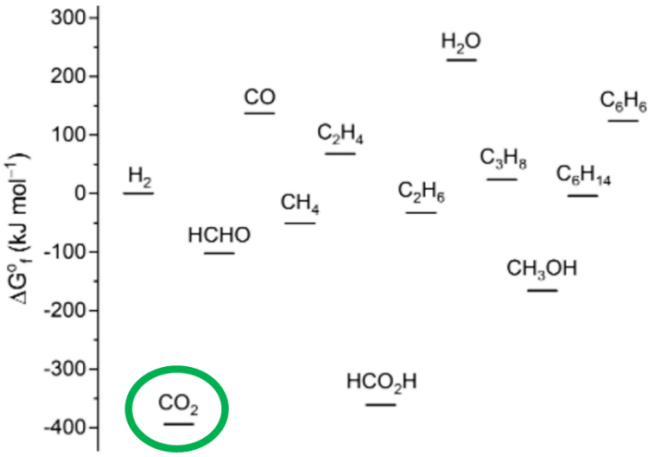

Figure 2. The formation Gibbs free energy of several molecules including CO_2. Adapted from [7].

Moreover, due to the highest oxidation state of carbon in CO_2, this molecule is thermodynamically stable. The dissociation energy of C=O bond of carbon dioxide is 750 kJ.mol^{-1}, significantly higher than C-O bond dissociation energy of carbon monoxide, which is 327 kJ.mol^{-1}. Additionally, the dissociation energy of C-C and C-H bonds are 336 kJ.mol^{-1} and 441 kJ.mol^{-1}, respectively [8]. This indicates that the reduction of carbon dioxide is not only non-spontaneous but also the dissociation of CO_2 is more challenging compared to the dissociation of CO and CH_x species.

Consequently, due to the thermodynamic and kinetic limitations of carbon dioxide, the carbon dioxide conversion represents a significant challenge and attracts considerable attention. Due to the remarkable stability of carbon dioxide, the usage of a catalyst is an essential means for converting carbon dioxide into value-added products while minimizing energy requirements. This is a major rationale for employing catalysts in CO_2 utilization, as they activate CO_2 for chemical reactions. The catalysis of CO_2 is elaborated in more detail in the subsequent sections.

1.3. Fundemantals of Catalysis

In the chemical industry, catalysis plays a crucial role, contributing to over 35% of the global gross domestic products, and catalytic processes are integral to 80% of all manufactured goods [9].

Catalysis is broadly defined as the process of the facilitating a reaction on the catalyst surface with high efficiency and minimal energy requirement. Intrinsic kinetics can be selectively changed by an effective catalyst. A catalyst enhances the rate of a chemical reaction by lowering the activation energy required for the process, and it remains unconsumed during the reaction. The manner in which catalysts lower the energy needed along the path from reactants to products is illustrated in Figure 3.

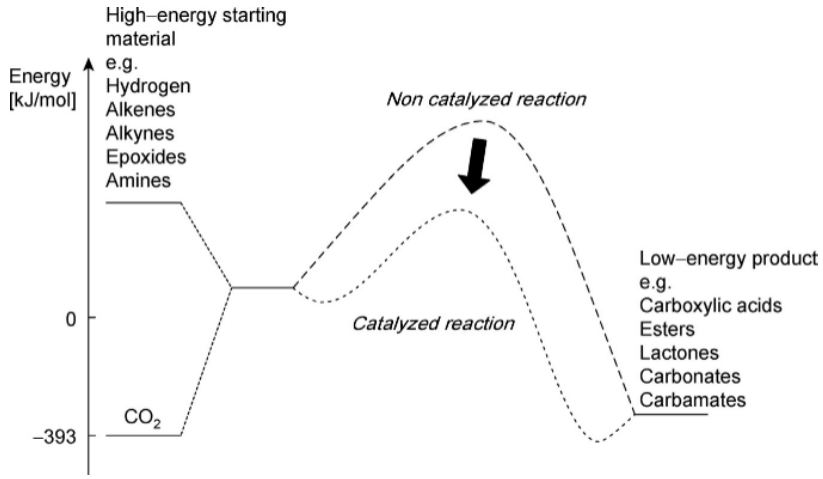

Figure 3. The reaction energy profiles for catalyzed and non-catalyzed reactions involving CO_2 as the reactant [10].

Catalysis can be categorized based on the phase of the system in which catalysis occurs. According to this classification, catalysis can be divied into two main branches: homogeneous and heterogeneous catalysis.

Homogeneous catalysis refers to a type of catalysis where the catalyst, reactants and products all exist in the same phase, typically in gas or liquid phase. Enzymes are an example of homogeneous catalysis. Furthermore, some industrial applications such as the oxidation of toluene to benzoic acids and aldeyhde production from the hydroformylation of olefins are mainly performed via homogeneous catalysis. Homogeneous catalysts are known for their high product selectivity compared to the heterogeneous catalysts. However, one of the major drawbacks of homogeneous catalysis is the challenge of separating it from products, making it less practical in some industrial processes. In addition to this drawback, the limited thermal stability of homogeneous catalysis is another challenge that reduces its efficiency.

Heterogeneous catalysis refers to a type of catalysis where the catalyst, reactants and products all exist in the different phases, typically with reactants in the gas phase and catalyst in the solid or liquid phase. Unlike homogeneous catalysis, the separation of catalyst from the products is not a problem in the heterogeneous catalysis due to the absence of different phases in the system. This attribute renders heterogeneous catalysts more practical and widely applicable in industrial processes. Many industrial applications involve heterogeneous catalysis. For instance, the production of ammonia and methanol are catalyzed by heteogeneous catalysts. Therefore, this thesis focuses on heterogeneous catalysis due to its prevalence in industrial applications [11].

In heteogeneous catalysis, the catalytic cycle comprises adsorption of species, reaction on the catalyst surface and finally desorption of products as demonstrated in Figure 4.

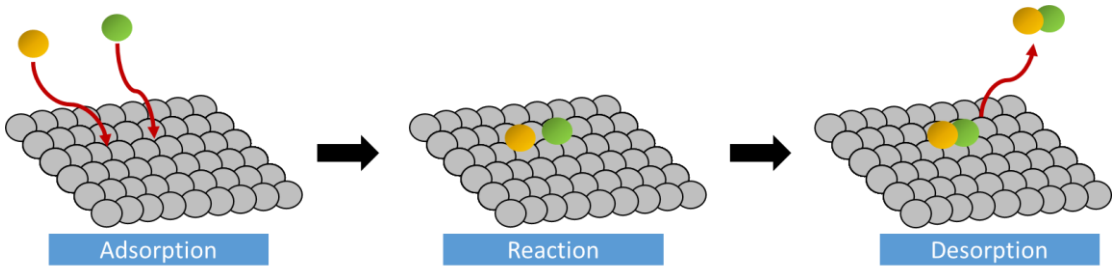

Figure 4. Catalytic cycle including adsorption, reaction and desorption. Adapted from [12].

The reaction equation in the catalytic cycle, including adsorption, reaction and desorption are provided in Equation 1.1, 1.2, and 1.3, respectively. A and B represent the input (reactant) of the catalytic reaction and C represents the output (product) of the catalytic reaction, while * represents the vacant site on the surface of the catalyst. All these elementary reactions have their own individual kinetics that contribute to the overall reaction rate.

$$A + * \rightleftharpoons A* \quad (1.1)$$

$$A* + B* \rightleftharpoons C* \quad (1.2)$$

$$C* \rightleftharpoons C + * \quad (1.3)$$

1.4. Catalysis for CO_2 Conversion

Industrial processes for the utilization of carbon dioxide were developed as early as the 1880s and 1890s for various applications, including urea synthesis, the soda Solvay process, and the synthesis of carbonates and salicylic acid [13]. Diverse routes for carbon dioxide conversion through catalysis are available, encompassing conventional, electrocatalytic, photocatalytic, biocatalytic and solar-thermal processes [10]. The transformation of CO_2 can be widely performed via electrochemical, thermal or photochemical reduction. Due to the small-scale application of electrochemical route and the low efficiency of photochemical route, these routes have led to limited usage in industry. Therefore, thermal reduction of carbon dioxide has garnered a significant attention.

The Sabatier reaction, which was the first CO_2 hydrogenation reaction to be developed industrially and produce methane in the 1910s, has had a major influence on our understanding of the fundamentals of contemporary catalysis [14]. After the discovery of Fischer-Tropsch Synthesis (FTS) in the 1920s by Frans Fischer and Hans Tropsch, this technological investigation becomes less industrially relevant. Carbon dioxide, which is an abundant carbon-containing chemical, can be used to synthesize various valuable chemicals such as diesel (C_{10}-C_{20}) and gasoline (C_5-C_{10}) via FTS.

Figure 5 illustrates the process of catalytic CO_2 hydrogenation, encompassing the capture of CO_2, its reaction with H_2, and the obtained value-added products like methane, methanol, olefin, formic acid, jet fuel, diesel, and gasoline. However, carbon dioxide is generally used in producing single carbon products (such as CO, CH_4, H_3COH etc.) and these products are widely studied in the literature [15].

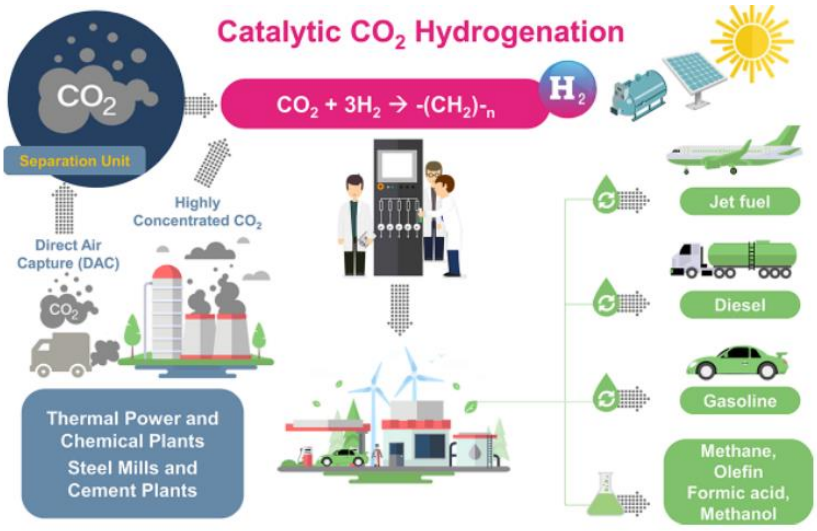

Figure 5. Catalytic CO_2 hydrogenation process [16].

The hydrogen required for the reduction of CO_2 can be sourced from the electrolysis of water, utilizing electricity generated from geothermal energy. Furtermore, the external energy required for the catalytic reaction can be supplied from geothermal energy sources locally available in the region. Hence, it is feasible to achieve economical utilization of carbon dioxide captured from flue gases with minimal adverse effects on the environment.

In addition to the FTS mechanism, carbon dioxide can be converted with methane to produce carbon monoxide and hydrogen through dry reforming of methane (DRM) at high temperatures (800-1000^oC) with assistant of supported catalysts [17]. Moreover, other strategies for reducing CO_2 include methanation and reverse water-gas shift reactions, in which hydrogen serves as a reductant [18]. For all these reduction strategies, the selection and utilization of suitable catalysts have a great importance to overcome the kinetic energies associated with the CO_2 conversion.

1.4.1. Heterogeneous Catalysts for CO and CO_2 hydrogenation

The primary advantage of using heterogeneous catalysts, which are typically based on metals and/or metal oxides, is their ease of separation from the products. There are various classes of heterogeneous catalysts, which include zeolites, transition metals, and metal-organic frameworks (MOFs). Among the other classes, the fact that transition-metal catalysts are useful in industries for several high-volume processes suggests that discovering novel types could have significant implications for the economy. Hence, this study focuses on the examination and discussion of transition metal catalysts.

1.4.1.1. Monometallic Catalysts

Numerous studies performed for understanding the catalytic performance of various monometallic catalysts in chemical reactions. A single type of metal serves as the catalytically active component in monometallic catalysts. Their activity is determined by the properties of their single-type metal and their different active phases. Monometallic catalysts are used in a wide range of reaction such as hydrogenation, oxidation and isomerization processes in the industry.

Monometallic catalysts have several advantages compared to the relatively more complex bimetallic catalysts including simplicity, well-understood mechanisms, stability and durability. Since they only need one kind of metals, they can be easier to scale-up in industrial applications and have lower production costs.

1.4.1.2. Bimetallic Catalysts

Bimetallic catalysts contain at least two distinct metal types, which can be chemically or physically mixed to produce active sites with unique characteristics. While

all of the bimetallic catalysts in these investigations exhibit some superior characteristics over monometallic ones, some properties are diminished.

Recently, bimetallic catalysts have demonstrated significant benefits for industrial use in CO_2 hydrogenation, surpassing the limitation of conventional monometallic catalysts. These catalysts can modify the properties of the catalyst, enhancing activity and product selectivity while inhibiting carbon deposition and metal sintering. Due to the synergistic effects between two distinct metals in the bimetallic catalysts, the catalytic performance is enhanced and modify the reaction rate.

In the literature, various monometals are used in various combination to obtain bimetallic catalysts. For instance, Co-Ni bimetallic catalysts are both experimentally and computationally studied in dry reforming of CO_2 by Fan et al. [19]. Ni-Fe and Ni-Co catalysts have been also utilized in various chemical reactions including the formation of methane and liquid fuels [20,21]. While all of the bimetallic catalysts in these studies exhibit some superior properties than monometallic ones, some properties are reduced. Further details regarding bimetallic catalysts are discussed in the following sections.

1.4.1.3. Sabatier Principle

In 1920, the relationship between adsorption strength of intermediate and rate of reaction was demonstrated by Paul Sabatier [22]. This connection between bond strength and reaction rate is depicted in Figure 6. According to this plot, the optimum bond strength corresponds to the point where the maximum catalytic reaction rate is achieved. This principle is known as the “Sabatier Principle”. This principle leads to the formation of a volcano-type relationship and has proven to be very useful in providing an understanding of where the optimum catalyst should be located. Accoding to this principle, the ideal catalyst should exhibit neither excessively strong nor excessively weak interactions with adsorbates in catalysis. It should possess an optimum bond strength between adsorbate and adsorbent.

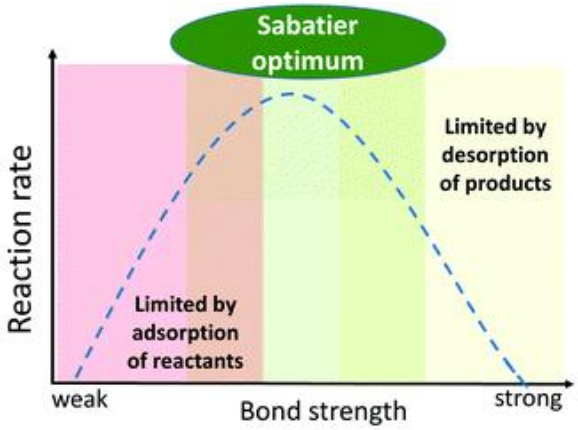

Figure 6. The Sabatier principle with the volcano-type plot [22].

1.4.1.4. Transition State Theory

Before the transition state theory (TST), the Arrhenius equation was generally employed to mathematically decribe the rate of a chemical reaction. Due to the empirical basis of the Arrhenius equation, new concepts such as the pre-exponential factor and the activation energy for a elementary reaction was discussed independently by Henry Eyring, Gwynne Evans and Michael Polanyi. The Arrhenius equation is given in Equation 1.4.

$$k = \nu . \, exp\left(\frac{-E_{act}}{RT}\right) \tag{1.4}$$

which ν is the pre-expontential factor and E_{act} is activation energy for a chemical reaction.

The time scales for atomic-scale modeling to reactor-scale rates exhibit variations. Approximately 10^{-15} seconds (femtoseconds) are required for molecular events to occur, implying that trillions of calculations would be needed to simulate an event that takes place every second through brute-force methods. This is solved by TST, which assumes a quasi-equilibrium between reactant states and the transition-state. This Eyring-Polanyi equation is shown in Equation 1.5.

$$k_i = \left(\frac{k_B T}{h}\right) exp\left(\frac{-\Delta G_a}{k_B T}\right) \quad (1.5)$$

where h is Plack's constant, k_B is Boltzmann's constant, and ΔG_a is the Gibbs free energy of activation. Due to the change in the rate constant, in the transition state theory, the reaction rate is represented as shown in Equation 1.6.

$$r_{TST} = \Gamma\left(\frac{k_B T}{h}\right) exp\left(\frac{-\Delta G_a}{k_B T}\right) \quad (1.6)$$

where Γ is the transmission coefficient.

A potential energy surface (PES) describes how the energy of a chemical system fluctuates as reactants assume different spatial positions in space. As the potential energy varies with the both spatial coordinate and reaction coordinates, the actual PES should be three-dimensional, as illustrated in Figure 7. There is no other way to calculate this potential energy surface except through quantum chemical calculations.

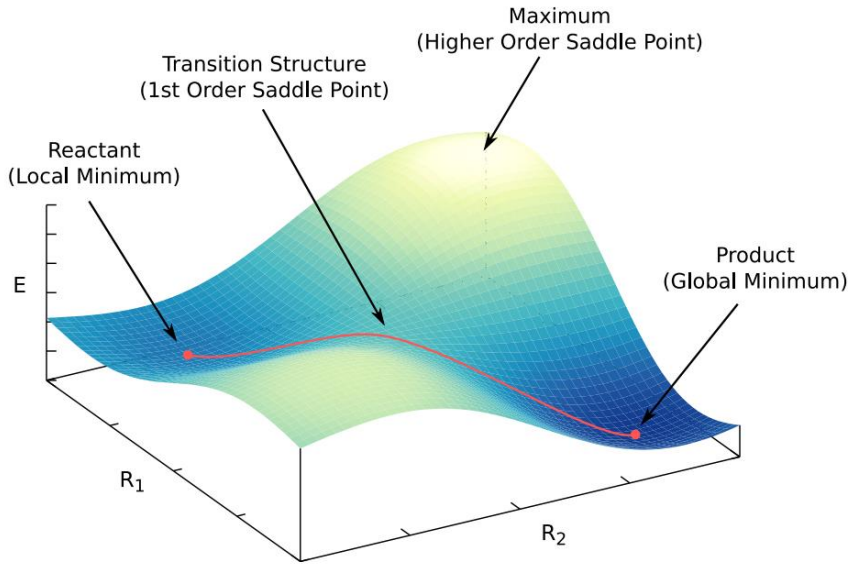

Figure 7. 3-Dimensional potential energy surface (PES) with local minimum, global minimum point, first order and high order saddle points [23].

In Figure 7, minima on the PES relate to mechanically stable configurations of a molecule, such as distinct confirmational isomers of a molecule or the initial state and final state of a reaction. The red line in the Figure 7 represents the pathway for a chemical reaction that occurs with the relatively minimum energy.

1.5. Fischer-Tropsch Synthesis

In 1923, the synthesis of synthetic oil compounds (synthol) from synthesis gas, which is the mixture of CO and H_2, over alkali promoted iron catalyst was discovered by Franz Fischer and Hans Tropsch. Briefly, Fischer-Tropsch Synthesis (FTS) is used as a technology to convert synthesis gas into mix of hydrocarbons [24]. In this tecnhology, synthesis gas (syngas) can be produced from any carbon-containing feedstock such as coal, natural gas, and biomass via gasification. Depeding on the raw material, the final products comprises various $H_2/CO/CO_2$ ratios [25]. Due to the limited petroleum reserves and environmental constraints, FTS technology is the focus of intensive research in both industry and academia, with numerous experimental and theoretical studies available [26–28].

FTS involves three steps including initiation, where reactants are converted into monomers, chain-growth, and ultimately termination to form products, such as olefin, paraffin, oxygenates [24,29,30]. Syngas can be utilized to generate predominantly linear-chain hydrocarbons, from methane to waxes. However, in practice, this reaction mechanism involves a high number of elementary reaction steps and produces valuable products with carbon chains ranging in length from 1-40. In FTS, the adsorbed oxygen can be removal as water or carbon dioxide in the catalytic cycle as the water-gas shift (WGS) reaction takes place [29]. Therefore, it mainly produces by-products, namely water and carbon dioxide, due to the occurrence of the water-gas shift (WGS) reaction. Due to the high exothermic nature of WGS reaction, it generates a large amount of heat during the process [31]. The reaction equations for FTS and WGS are provided in Equation 1.7 and 1.8, respectively.

$$\textbf{FTS:}\quad CO + 2H_2 \rightleftharpoons -CH_2- + H_2O \qquad \Delta H_{298} = -165\ kJ.mol^{-1} \qquad (1.7)$$

WGS: $CO + H_2O \rightleftharpoons CO_2 + H_2$ $\Delta H_{298} = -42\ kJ.mol^{-1}$ (1.8)

Reaction 1.7 represents the CO hydrogenation and the polymerization of carbon-containing species with a distribution in various molecular weights. In FTS, the goal is to obtain the desired product(s).Therefore, the ability to selectivity control plays a key role in this process.

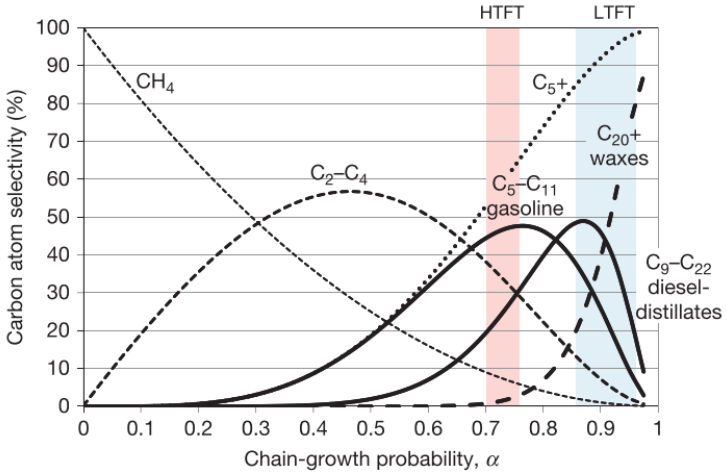

Figure 8. Anderson-Schulz-Flory (ASF) model for FTS [31].

In FTS, C-O bond in the CO molecule must be broken and C-C and/or C-H bonds need to be formed in order to obtain carbon-containing products during the process. In this mechanism, the formation of C-C bonds is responsible for the chain growth of the products. Therefore, the formation of new C-C bonds and increase in the chain-growth are desired for producing long-chain hydrocarbon products. The Anderson-Schulz-Flory (ASF) α value, representing the probability of growth, is used to predict the product spectrum in FTS. High α values indicate that the resulting products will consist predominantly of heavy hydrocarbons, while low α values imply a high proportion of light hydrocarbons such as methane. This relationship is demonstrated in Figure 8. By choise of the suitable catalyst, reactor and operating conditions, the spectrum of the products can be manipulated. To control the product selectivity and achieve high yields of desired products, it is essential to use of suitable catalysts during the reaction.

The overall FTS process is commonly referred to based on the original source of synthesis gas and its conversion into liquid products as “gas-to-liquid”, “coal-to-liquid”, and “biomass-to-liquid”. The general concept of the FT process is illustrated in Figure 9 and is discussed further below.

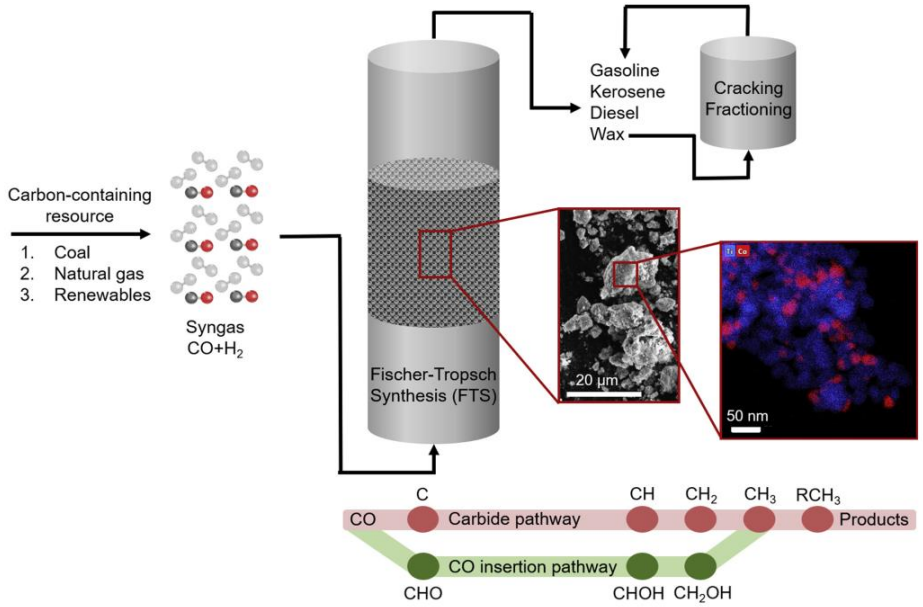

Figure 9. The conceptual representation of FTS in reactor using heterogeneous catalyst, along with the reaction pathways within the reactor. Adapted from [32].

In the first step of the FTS process, the carbon-containing source is converted to syngas through gasification. Solid carbon sources such as coal and biomass are typically gasified using a noncatalytic method. This method involves partial oxidation with oxygen which provides the required heat for the gasification and reaction with steam [31]. When natural gas is utilized as a carbon source, it can be converted into syngas in the presence of oxygen and steam. In the second step, the syngas is catalytically converted to a range of products including linear hydrocarbons via FTS in the reactor. In the last step of the process, the final products are further processed through hydrocraking of waxes to achieve middle distillate range components such as diesel (C_9-C_{22}) and jet fuel (C_9-C_{15}). FTS has been performed in two main regimes: low temperature Fischer-Tropsch (LTFT) and high temperature Fischer-Tropsch (LTFT). The low-temperature FT and high-temperature FT synthesis can be conducted at temperatures of 200-250°C and 320-350°C,

respectively. These two processes can occur under pressures ranging from 10 to 50 bar in fixed-bed, fluidized-bed, and slurry reactors [31,33]. In a HTFT, iron-based catalysts are mostly used and mainly linear low molecular mass olefins and gasoline are obtain as products, while mainly high molecular mass linear waxes are produced in iron or cobalt catalyzed LTFT process.

1.6. CO_2-based Fischer Tropsch Synthesis

Carbon dioxide can be used as a main carbon-containing reactant with hydrogen and carbon monoxide as mixture to produce liquid fuels in FTS mechanism, which is called CO_2-based FTS [5]. In this process, air or combustion waste gases can be source of CO_2 and the source of H_2 are typically renewable sources.

CO_2-based FTS is an established technology, which not only produce high value-added chemicals (such as liquid hydrocarbons, alcohols, olefins) but also mitigate the greenhouse effect by reduction of CO_2 [15]. Additionally, the conversion of CO_2 in the syngas may offer an opportunity to boost total yields. For example, removing H_2O during FTS can be achieved by the addition of external hydrogen.

The hydrogenation of carbon dioxide consists of two-process pathways, namely reverse water-gas shift (RWGS) reaction and FT synthesis. The reaction equation of RWGS and FTS are given in Equation 1.9 and 1.10, respectively. Due to the presence of additional RGWS reaction, more hydrogen is required in this tandem reaction compared to the conventional FTS. Moreover, this leads to the formation of more water as by-product in CO_2-based FTS. As indicated in Equation 1.9, carbon monoxide is primarily generated through the RWGS reaction when aiming to generate carbon-containing products.

$$\textbf{RWGS:}\quad CO_2 + H_2 \rightleftharpoons CO + H_2O \qquad \Delta H_{298} = +42\ kJ.mol^{-1} \tag{1.9}$$

$$\textbf{CO}_\textbf{2}\textbf{-FTS:}\quad CO_2 + 2H_2 \rightleftharpoons -CH_2- + H_2O \qquad \Delta H_{298} = -152\ kJ.mol^{-1} \tag{1.10}$$

In industrial applications, the methanation of CO_2 or CO is undesirable due to its negative impacts on the economic viability of the process. Consequently, the formation of methane is less favored when compared to the production of liquid hydrocarbons [34]. Due to the high stability of CO_2, its hydrogenation is challenging, resulting in low reaction conversions. Nevertheless, significant progress has been made in converting CO_2 to single carbon products, such as carbon monoxide, methane, and methanol. Therefore, the catalysis of CO_2 into C_1 products has been extensively studied in the literature [14,35].

While active and selective catalysts are well-established for conventional FTS, optimizing the activity, selectivity, and stability of catalysts for CO_2-based FTS remains an ongoing challenge and a vital academic research area. Therefore, designing high-performance catalysts for CO_2-based FTS is of paramount importance to produce the desired products, including heavy hydrocarbons, while minimizing the generation of undesired by-products. As CO_2-based FTS occurs in two sequential reactions, namely RWGS and FTS, the suitable catalyst must be active in both the RWGS and FTS reactions.

1.7. CO and CO_2-based FTS Catalysts

In CO_2-based Fischer-Tropsch Synthesis (FTS), the cleavage of the C-O bond is a critical step for both CO and CO_2 dissociation, as well as the formation of CH_x species on the catalyst surface. Certain transition metals have the ability to dissociate carbon monoxide and carbon dioxide and are commonly employed as FTS catalysts. Despite the similar electronic structures, the selection of transition metal catalyst, influenced by factors such as the filling of the d-band, results in the production of significantly different products in the reaction. The filling of d-band, which represents the energy band associated with the d orbitals of transition metals, increases as one moves from left to right in the periodic table.

As illustrated in Figure 10, transition metal groups can be categorized based on their distinct properties such as catalytic activity, the adsorption strength of CO or H_2, and whether they are reducible oxides during the reaction. Among transition metals, the most active catalysts for FTS are mainly known to be ruthenium (Ru), nickel (Ni), cobalt (Co)

and iron (Fe) due to their good FT activity and dissociative CO adsorption properties [36]. In addition to the transition metals, some noble metal catalysts, such as Rh and Ru, are catalytically active and stable in the FTS reaction. However, they are not prefered choices due to their limited availability, making their use in a large-scale applications challenging.

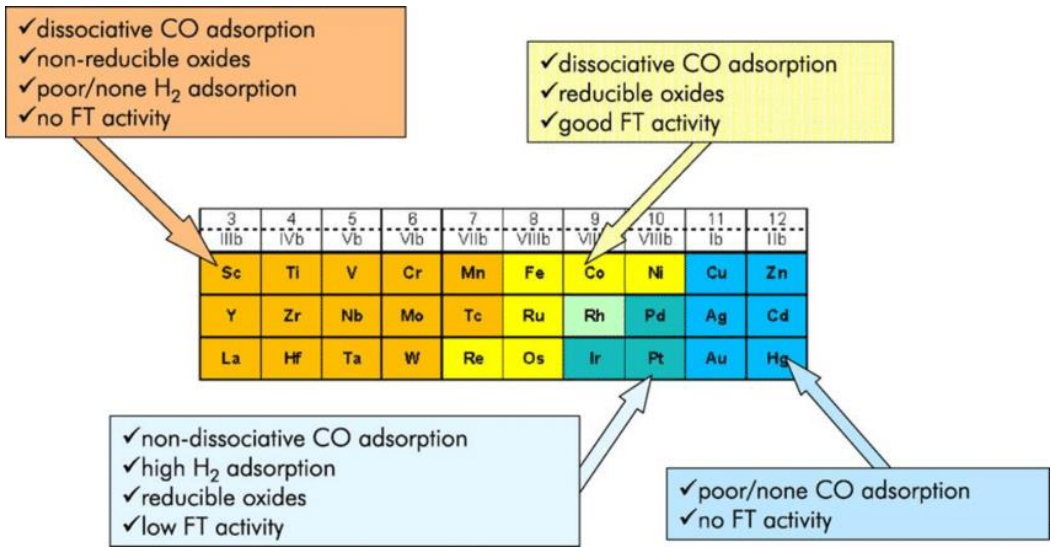

Figure 10. Transition metals and their properties in FTS [37].

While Fe, Co and Ru mainly produce long-chain hydrocarbons in FTS, Ni mainly produces methane as a product. However, due to the high selectivity of nickel towards methane and the scarcity and cost of ruthenium, they are not good candidates for FTS. Therefore, Co- and Fe-based catalysts are primarily employed for FTS.

Typically, FTS catalysts consist of metal oxide nanoparticles such as cobalt oxide (Co_3O_4) and iron oxide (Fe_2O_3) before the catalytic reaction. Metal oxides are converted by treated with H_2 or CO/synthesis gas to obtain active form of the catalyst. During the actual reaction conditions, both oxidic and metallic phases coexist on the catalyst surface.

The type of active sites, supports, particle size, and quantity of active sites on the surface all have a significant impact on the activity and selectivity of catalysts. The active sites on a catalyst's surface are impacted by varying preparation and pretreatment conditions, which can result in a catalyst with varying activity and selectivity toward the production of particular products. Furthermore, the ratio of feed gas also affects the product selectivity of the catalytic reactions. For instance, different feed gas compositions

are required for iron- and cobalt-based FT catalysts due to their distinct reactivity and selectivity profiles.

Regarding CO_2-based FTS, the effect of CO_2 in the FTS have been studied with various catalysts. In the following sections, iron- and cobalt-based catalysts are examined within both conventional and CO_2-based FTS.

1.7.1. Iron-based Catalysts

Fe-based catalysts have been extensively studied for CO_2 hydrogenation due to active sites they offer for both RWGS and FTS, which are the two catalytic reactions involved in CO_2 hydrogenation to form value-added products [38]. Although Fe-based catalysts are active for RWGS, they are also active catalysts for WGS, which is the reverse reaction. These catalysts exhibit promising effects for CO_2 hydrogenation to long-chain hydrocarbons when CO in the feed gas is replaced by CO_2, while they exhibit selectivity towards olefins and oxygenates when feed gas contains CO [39].

Since iron-based catalysts exhibit high activity towards RWGS and FTS reactions, they stand out in CO_2-based FTS [26,40]. Due to the relatively high activity in RWGS, iron catalysts are favored over cobalt catalysts. In the context of the active phases of iron-catalysts, it is known that for RWGS reaction and CO hyrogenation, the active phases are known as iron oxide (Fe_3O_4) and Hägg carbide (x-Fe_5C_2) over iron-based catalysts.

In iron catalysts, active sites are formed the mixture of iron oxide and iron carbide, formed by exposing a mixture of CO and H_2 into iron oxide. Some experimental studies including XRD analysis have shown that RWGS reaction occurs on the surface of oxidic iron phases, while FTS takes place on the surface of iron carbides. When iron carbide was not formed on iron oxide catalysts through carburization at CO_2-based FTS conditions, high RWGS and low FTS activity was observed in the several studies [39,41]. At high temperatures, the catalytic activity of iron-based catalysts increases, facilitating the conversion of carbon monoxide into carbon dioxide through the water-gas shift (WGS) reaction [33]. Therefore, water and carbon dioxide can be obtained as by-products in the iron catalyzed FTS reaction. Due to its high activity towards WGS, it is often utilized for feedstocks with an H_2:CO ratio of 1, such as coal and biomass [32].

The primary advantage of iron as a FT catalyst, in comparison to most other transition metals except for nickel, is its abundant availability and cost-effectiveness. Another notable advantage of iron catalysts is that iron-based catalysts exhibit a relatively lower sensitivity to variations in temperature and pressure, in contrast to cobalt catalyst. Also, they can be used to produce a variety of products in FTS. Iron catalysts generally exhibit selectivity towards olefins and oxygenates and can be operated in a wider temperature range (200-350^{o}C). The catalytic performance of the iron-based FT catalysts can highly be tuned by promoters, such as K, Mn, Ce and Na [42,43]. The addition of promoters on iron are also used to form bifunctional nanocrystals containing iron oxide and carbide phases. Fe-based catalysts exhibit excellent activity in the formation of hydrocarbons, particularly with the use of effective promoters, specifically potassium [44]. Moreover, the ratio of CO/CO_2 in the reactant gas affects the performance of the catalyst due to the different activities of these reactants on cobalt and iron catalysts. In the case of Fe-based catalysts, shifting the feedstock from CO to CO_2 increases the selectivity for hydrocarbons.

1.7.2. Cobalt-based Catalysts

In contrast the Fe-based catalysts, cobalt-based catalysts are widely used in the industrial FTS applications and produce selectively alcohols and hydrocarbons [25]. These catalysts demonstrate high activity and stability under FTS conditions with high H_2 ratios, while exhibiting limited effeciency in CO_2 hydrogenation. However, they also come with a higher cost compared to iron-based catalysts.

Due to their long lifespan, a good balance between performance and cost can be achieved with cobalt catalysts. The activity of cobalt-based catalysts at low reaction temperatures is higher than that of the iron-based catalysts. Moreover, cobalt catalysts are relatively low active for WGS compared to the iron catalysts. Due to its low activity towards WGS, it is often utilized for feedstocks with an H_2:CO ratio of 2, such as natural gas [32]. However, it is highly sensitive to poisoning with sulfur and it is still remain a challenge in cobalt-based catalysts [45]. When switching of synthesis gas from CO to CO_2, the selectivity of the Co-based catalysts are extensively changed. Due to their strong

hydrogenation ability and low RWGS activity, cobalt catalysts primarily exhibit selectivity towards methane when CO_2 is used as feedstock. Furthermore, cobalt catalysts can enhance the adsorption of carbon dioxide, thereby inhibiting carbon deposition on the surface and carbon removal. Nevertheless, cobalt-based catalysts exhibit low carbon deposition and are recognized for their greater carbon resistance compared to Ni catalysts [17].

Among the various phases of cobalt catalysts, the metallic Co phase is recognized as the most active phase in FTS conditions. Especially, the metallic cobalt phase (Co^0) is attributed to the dissociation of CO and the coupling of C-C, resulting the formation of long-chain products in FTS. However, this phase is also known to increase the selectivity towards methane, which may not be desired product in FTS. Furthermore, the dissociation of CO on metallic cobalt leads to the formation of water as a by-product [46]. Regarding the RWGS activity, cobalt oxide phases are mainly enhanced the activity towards RWGS compared to the metallic cobalt phase [47].

1.7.3. Bimetallic Iron-Cobalt Catalysts

As both iron and cobalt catalysts have some advantages and disadvantages in CO_2 hydrogenation into hydrocarbon products, bimetallic Fe-Co catalysts have received considerable attention in the literature for enhancing their catalytic performance, leading to the development of high-performance catalysts for both CO and CO_2 conversion. Due to the presence of the synergistic effect, which arises from the combination of multiple metals resulting in a combine effect beyond their individual contributions, iron and cobalt metals can form an alloy phase. Additionally, various phases including monometallic phases may be presence on the bimetallic nanoparticle, which can influence and alter the catalytic performance.

In bimetallic Fe-Co catalysts, strong interaction between Co and Fe affect the adsorption of main intermediate, namely CO, and reducibility of metals. Fe catalysts appear to exhibit a bcc crystal phase, while Co catalysts appear to have hcp or fcc phases. However, the active crystal phase of bimetallic Fe-Co catalysts depends on the concentration of Fe and Co metals. At higher Fe contents, the lattice of the bimetallic

catalyst becomes Fe rich and switches to a more compact the bcc phase, whereas with low Fe concentration, the bimetallic catalyst is typically found in the hcp or fcc phases [48]. This effect of Fe concentration on lattice has also been observed in Ni-Fe catalysts [36].

In recent studies, the catalytic performance of bimetallic FeCo catalysts and the effect of each metals have been a subject of ongoing discussion. In the context of the CO and CO_2 hydrogenation, the experimental and computational investigations have revealed that bimetallic FeCo catalysts can yield a range of products. Some studies revealed that bimetallic Fe-Co catalyst produce higher proportion of gasoline and olefin and a lower proportion of methane and wax in the product distribution compared to the monometallic Co and/or Fe catalysts [49,50], while others suggest that bimetallic Fe-Co catalysts exhibit low selectivity towards long-chain hydrocarbons [51]. Hence, further research is essential to gain a comprehensive understanding of the effects and potential of bimetallic FeCo catalysts.

1.8. Computational Quantum Chemistry and Catalyst Design

The substantial economic impact of the chemical industry has improved the importance of enhancing the efficiency of catalysts. From the nanoscale to macroscale investigations, different techniques are required for each scale, which means that there is no single technique for this area. While kinetic data is experimentally collected for reactions at the macroscale, computations of system properties at the atomic scale are conducted to gain insight into reactions at the nanoscale. The design of a catalyst often involves a trial-and-error process in experimental approaches. Under experimental reaction conditions, the identification of the active phases of catalysts is a promising approach for developing and synthesizing catalysts that exhibit higher selectivity for the desired products. Nevertheless, computational methods play a cruical role in the design and development of suitable catalysts, owing to the increase in advanced computing power over the last two decades. As the catalyst design through computational methods has various dominant advantages compared to experimental methods, the utilization of computational methods remains challenging. Modeling of complex real catalysts and the

effect of the support on realistic nanoparticles can be considered as significant challenges of this approach.

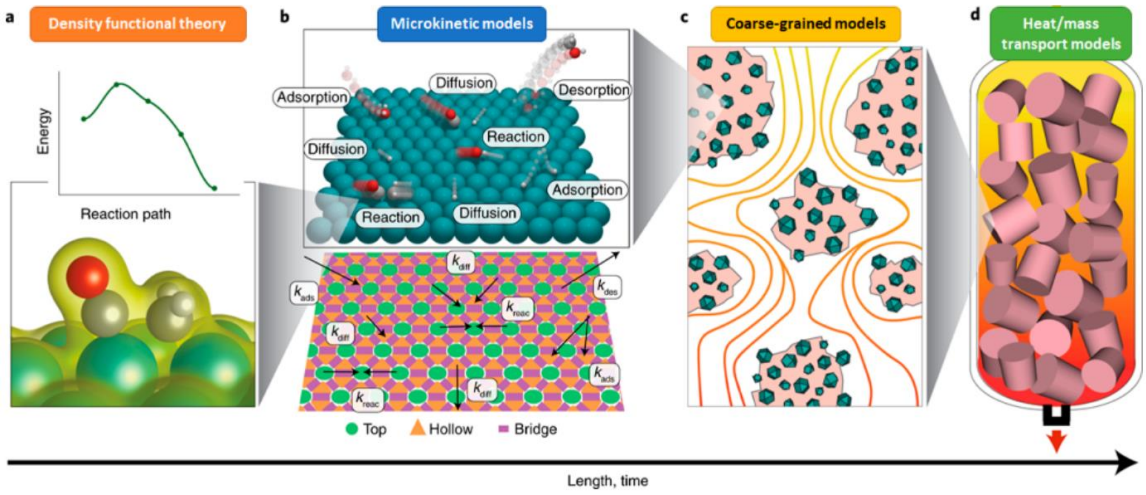

Figure 11. Illustration of the bottom-up steps for multiscale catalysis, from computational modeling to reactor-scape applications [52].

The design of high-performance catalysts with multiscale models consists of several steps, as shown in Figure 11. Additionally, the design of catalyst consists of three interdependent properties, namely catalytic properties, chemical-physical characteristic and mechanical properties of the catalyst. These three properties are so-called “triangular concept”, which is proposed by Anderson and adapted to this reaction by Ferrauto and Bartholomew in 1997 [12].

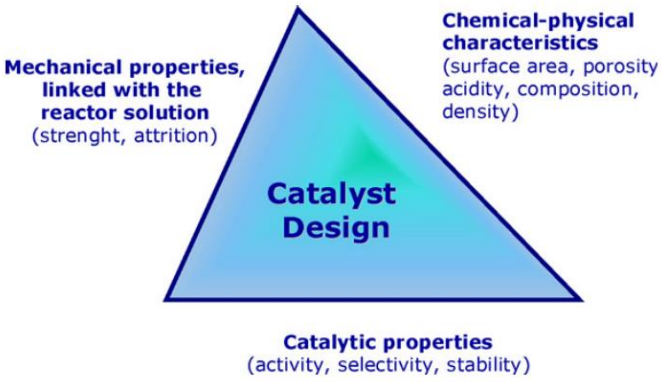

Figure 12. The triangular consept of the catalyst design [37].

To enhance the selectivity for desired products, it is essential to have a comprehensive understanding of the reaction mechanisms responsible for the formation of products. In both conventional and CO_2-based FTS reactions, the mechanism involving the scission of C-O bond and the formation of C-C coupling are essential to understand the behaviour of the reaction.

Consequently, computational methods are recognized as a cornerstone of the modern catalysis and surface science, and their importance has been growing, paralleling the increasing expansion of their application areas.

1.8.1. Basics of Computational Quantum Chemistry

The Nobel Prize for the discovery of new productive forms of atomic theory was awarded to Erwin Schrödinger and Paul Dirac in 1933, and this discovery is based on the famous Schrödinger equation as described in Equation 1.11.

$$i\hbar \frac{\partial}{\partial t}\psi = \hat{H}\psi \qquad (1.11)$$

where $\hat{H}$ is Hamiltonian operator, ψ is the wave function. The Hamiltonian is an operator whose properties are determined by the physical system being described. A Hamiltonian that accounts for the interaction of numerous electrons with multiple nuclei and with each other is required to represent the chemistry that governs heterogeneous catalysis, or chemistry in general.

The time-independent Schrödinger equation (Equation 1.12) is the simplified version of the Schrödinger equation that describes systems with energy levels and stationary states, where the wave function does not vary with time due to the time-independent Hamiltonian.

$$\hat{H}\psi = E\psi \qquad (1.12)$$

where E is the total energy of the system. As this equation seems more basic than that of original version of it, it is still complex and difficult to solve. The wave function of a system contains all information about that system, including details about the ground state energy and the probability distribution of its electrons. The time-independent Schrödinger equation (TISE) can be analytically solved for relatively simplest system such as atomic hydrogen, however, more complicated systems cannot be solved analytically due to the intricate interactions arising from the many-body electron-electron interactions.

The Schrödinger equation for a single (for particle i) describing a non-interacting electrons of a system is given in Equation 1.13.

$$\left(-\frac{\hbar^2}{2m}\nabla^2 + \hat{V} + \hat{V}_H + \hat{V}_{XC}\right)\varphi_i = \varepsilon_i\varphi_i \qquad (1.13)$$

which φ_i and ε_i represents the wave function and energy for each non-interacting electron, respectively.

This method provides an approach to obtain information about the system such as energy, structure, and properties of molecules and atoms by introducing a system to resemble the real many-body system. It accomplishes this by creating an approximation that divides the problem into an effective potential and a non-interacting electron model.

1.8.2. Density Functional Theory

As an alternative method for solving Schrödinger equation for complex systems including many-body electron-electron interactions, Density Functional Theory (DFT) is performed as a powerful quantum chemical method [52]. This method utilizes the electron density of the system to provide us the properties of the ground states [53]. This method presents several opportunities, including the ability to conduct atomic-level examinations of the catalyst structure, model surface species that may or may not have been observed experimentally, and predict the energy of reactions that align with experimental findings based on the chosen functionals.

The number of computational studies on DFT and its importance in various scientific subjects is growing rapidly by the year. These studies encompass the design of catalytic processes, drug design, and many other issues in science and technology [53]. Due to the large number of atoms in a heterogeneous catalyst system, the computational cost of modeling the catalyst increases significantly.

1.8.3. Kohn-Sham Method

Kohn-Sham method is a basic framework for quantum mechanics that is used to compute the electronic structure of the system consisting of atoms and molecules. It was developed by Kohn and Sham in 1965 [54]. Since then, computational chemistry has heavily relied on this approach. As suggested by Kohn and Sham, the ground state energy of the system can be represented as a function of the charge density, as follows:

$$G[n] = T_s[n] + E_{xc}[n] \tag{1.14}$$

where $T_s[n]$ is the kinetic energy of the sistem with the electron density n(r). This method define E_{xc} as the exchange and correlation energy.
After the derivations, the final form of the equation is as follows:

$$E = \sum_1^N \epsilon - \frac{1}{2}\iint \frac{n(r)n(r')}{|r-r'|} drdr' + E_{xc}[n] - \int v_{xc}(r)n(r)dr \tag{1.1.5}$$

The only limititon that hinders to the direct application of this method is that the $E_{xc}[n]$ and v_{xc} are not known. There is no DFT theory that offers an exact exchange corelation functional, however, various approximations have been employed.

1.8.4. Born-Oppenheimer Approximation

The ground state energy is the result of combining several contributions. One approach to partitioning it is to factor in energy contributions from both the atomic nuclei and the electrons.

$$E_{tot} = E_{elec} + E_{nucl} \tag{1.16}$$

Equation 1.16 represents the total energy (E_{tot}) which is the sum of energy of electrons (E_{elec}) and nuclei (E_{nucl}). Nuclei are significantly more massive than the electrons orbiting around them. Therefore approximating the electrons as moving while the nuclei remain fixed is a reasonable assumption. With this approximation, the total energy calculations also account for the energy contribution from the nuclei [55].

1.8.5. Exchange-Correlation Functional

Due to the approximate treatment of the exchange-correlation term in the Kohn-Sham method, this method cannot be used for the exact solution of the many-body Schrödinger equation. It can be determined the same ground state density by mapping the fully interacting system to the auxiliary non-interacting system. Therefore, exchange-correlation functional which is given in Equation 1.17 should be used [56].

$$E_{xc}[n(\vec{r})] = \Delta E_{ee}[n_2(\vec{q},\vec{r})] + \Delta E_T[\psi(\vec{r_1},\dots,\vec{r_N})] \tag{1.17}$$

where E_{ee} is Pauli-repulsion, and E_T is kinetic energy of the non-interaction Kohn-Sham orbitals. The last piece of energy functional is the exchange-correlation energy. While it is technically a consequence of the Kohn-Sham orbitals, it's evident that optimizing it in

relation to the Kohn-Sham orbitals is synonymous with optimizing it with respect to the density.

The success of DFT is based on the exchange-correlation functional that describes the complex many-body effects within single particle and utilizes the electron density formalism. With the choice of appropriate exchange-correlation functional for DFT calculations, the outputs can be highly accurate and consistent with experimental results.

1.8.6. Pseudopotentials

Computing of electronic properties of the system contains many electrons requires a significant amount of computational power. As the number of electrons in the system increases, the power and time required for calculations will gradually increase. To prevent this, Helmann developed a pseudopotential to consider the influence of valence electrons on the properties of the system [57].

Although this method may have lower accuracy, it is surprisingly effective in the simulating the results of all electron calculations. It also has significantly reduced the computational costs associated with the heavy atoms or molecules.

1.8.7. Climbing Image Nudged Elastic Band (CI-NEB) Method

Based on the initial and final states of the elementary reaction, the highest energy of these two states which is called transition state (TS) or a saddle point in the energy landspace can be found using nudged elastic band (NEB) method [58]. As can be understood form the name of the method, this method is like an imaginary elastic band that you gently move along a pathway connecting two states (initial and final) of a system. This allows the system to relax and investigation the energetically favourable route referred to as the minimum energy pathway. This method involves minimizing an elastic band, during which the perpendicular component of the spring force and the parallel component of the true force are extracted or projected out.

By the Henkelman et al., the NEB method was improved with additions that allow the obtain more accurate determination of saddle points with fewer images than the original NEB method. This improved method is called climbing image nudged elastic band (CI-NEB) method [58].

1.8.8. Vibrational Frequency Analysis

To clarify the transition state of each elementary reactions, the convergence of the CI-NEB calculations are not enough in computational calculations. The aim of the CI-NEB is the find a point close to the transition state but it should be determined that after CI-NEB calculations the found point is a TS or not. Therefore, it is essential to conduct the vibrational frequency analysis to validate that all vibrational frequencies are real-valued numbers, meaning they correspond to a positive force constants. Nevertheless, there should be single imaginary frequency, meaning it corresponds to a negative force constant, which aligns with the direction of the reaction coordinate for the saddle point of the elementary reaction.

1.9. Surface Science Approaches in Quantum Chemical Modeling of Catalytic Systems

Due to the excesive number of atoms on the realistic catalyst nanoparticles, the calculations are performed on systems with limited number of atoms. To limit the number of atoms, two basic type of methods are used: Cluster and slab methods.

The cluster model involves selecting a small cluster of atoms to represent the active site of the surface or the system of interest. This cluster contains the atoms that directly participate in the reaction or adsorption process. In contrast, the slab model represents the entire surface is represented as a periodic slab with a repeating unit cell structure in the slab approach. Within the surface of this unit cell, there are many layers of atoms. Slab model is particularly suitable for represent the surfaces.

Cobalt can exist in two different crystallographic structures, face-centered cubic (fcc) and hexagonal closed packed (hcp) phases, in FTS operating conditions. As shown in Figure 13, hcp and fcc Co phases offer six and four different facets, respectively. These phases offer different facets and activities for catalytic reactions.

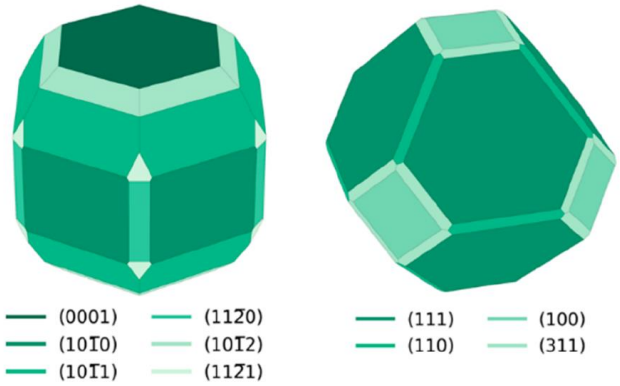

Figure 13. The Wulff equilibrium shape of hcp cobalt (left) and fcc cobalt (right) as determined through DFT calculations by Liu et al [59].

1.10. Objectives of the Study

The objectives of the study are summarized in two key points as follows:

- To investigate the activity, selectivity and stability of the Fe-doped Co(111) [FeCo(111)] surface in comparison to the pure Co(111) surface for CO_2-based FTS,
- To investigate the structure-activity relationship for Fe-Co bimetallic catalysts and gain a comprehensive understanding of the catalytic cycle on Fe-Co bimetallic catalysts.

The modeling of the Fe-doped Co(111) metallic surface is of high importance, given that numerous experimental and theoretical studies have observed and confirmed the significant role of the catalyst surface in influencing catalyst selectivity.

To achieve these objectives, the first step is the computational design of stable and realistic surface models for both monometallic Co and bimetallic FeCo surfaces, based on the literature. Then, investigation of all elementary steps on both pure and Fe-doped

cobalt surfaces to gain insight on the bimetallic catalyst at the atomic-scale with DFT calculations.

Through this comparative study, it becomes possible to gain a clearer understanding of the reactions occurring on the same surface, the electronic structure of the surface, and the alterations in the interaction of adsorbates with the surface resulting from the addition of iron in the cobalt surface.

CHAPTER 2

LITERATURE SURVEY

2.1. Active Phases and Surface Structures of Bimetallic Fe-Co Catalysts

FTS is acknowledged as structure-sensitive reaction, indicating that the structure of catalyst nanoparticles has a significant impact on the catalytic performance. It is widely accepted that the formation of chain growth through C-C bond formation, which represents a crucial step in the production of desired long-chain products, is structure-sensitive [44]. The differences in catalytic activities on various crystal surfaces can be attributed to variations in the coordination numbers of the surface atoms. Specifically, significant changes in the binding energy or strength of an adsorbate when it is situated at surface sites with lower coordination, like step and kink sites on the surface.

The surface structure of the bimetallic catalysts has been extensively studied, both experimentally and theoretically, and various surfaces have been proposed and characterized under various reaction and synthesis conditions [60–62]. In this computational study, the selection of the bimetallic catalyst surface model is crucial and was developed with reference to previous studies in the literature. Therefore, in this section, the bimetallic Fe-Co surfaces characterized in previous studies are discussed in detail.

On the catalyst surface, various active phases can coexist and participate in catalytic reactions, collectively contributing to the catalytic performance of the catalyst. Therefore, determining the active phases on the catalyst surface and understanding their effects in catalytic cycle are crucial for designing high-performance catalysts. For both Co- and Fe-based catalysts, their structure is relatively well-understood due to the extensive research efforts. However, the structure of the bimetallic catalysts, particularly FeCo catalysts, are more complex due to the distinct properties of metals and their interactions between themselves in the bimetallic nanoparticle. For instance, Gnanamani et al. revealed a comprehensive relationship between structure and product selectivity of unsupported Co,

Fe and Fe-Co bimetallic catalysts with various metal ratios in CO_2-based FTS conditions, specifically at 10 bar and within the temperature range of 220-270°C [51]. As shown in Figure 14, various phases, including *x*-Fe_5C_2, metallic FeCo, Fe_3O_4 and $CoFe_2O_4$, were identified on the catalyst surface using high-resolution transmission electron microscopy (HRTEM) technique, while monometallic cobalt catalysts were mainly consist of metallic fcc Co phase.

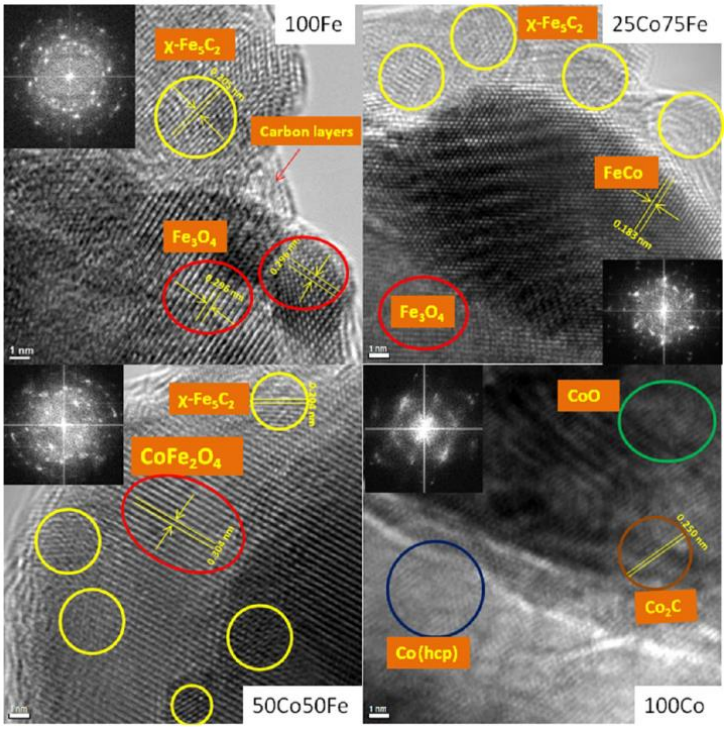

Figure 14. HRTEM images of pure Fe, pure Co and Fe-Co bimetallic catalysts.

The distribution of Fe and Co metal atoms in the synthesized bimetallic FeCo catalyst was demonstrated through high-angle annular dark-field scanning transmission electron microscopy (HAADF-STEM) with elemental mappings of Fe and Co by Sandupatla et al [63]. As shown in Figure 15, their findings confirmed the formation of an alloy phase, which plays a role in facilitating methane formation and decreasing CO formation on the bimetallic catalyst compared to the monometallic Co and Fe catalysts, while reducibility of the Co catalyst was enhanced by the presence of Fe atoms.

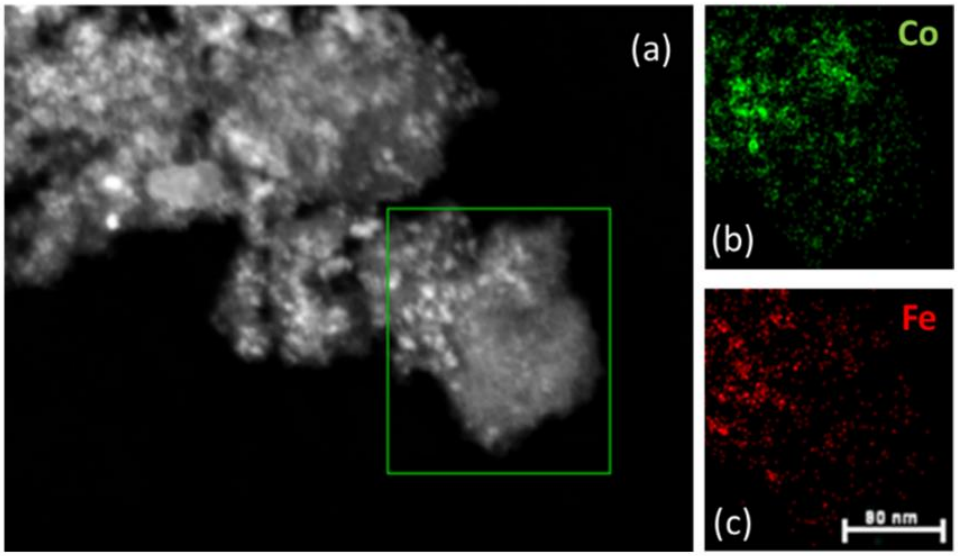

Figure 15. HAADF-STEM image of alumina supported FeCo bimetallic catalyst (a), elemental mapping of cobalt (b) and iron (c) catalysts [63].

In another study, bimetallic FeCo nanoparticles on a support material were synthesized and investigated under FTS conditions by Ismail et al. [64]. They observed that these miscible metals were homogeneously mixed during the synthesis of catalyst. After the reduction of the catalyst, CNT supported bimetallic FeCo catalysts were performed at LTFT (1 bar and 220^{o}C) and HTFT (1 bar and 350^{o}C) conditions. As shown in Figure 16, the characteristic peaks of the phases on the nanoparticles were observed, indicating that the metallic CoFe phase is the dominant phase after LTFT. Furthermore, after the reduction, the structure of the bimetallic catalyst shifted from homogeneous structure to core-shell structure. The core was composed of the FeCo alloy, whereas the shell was primarily comprised of the iron oxide phase. It is evident that the presence of Fe enrichment bimetallic FeCo surfaces. Furthermore, the oxidic iron phase on the shell was attributed to the contact with air during the TEM analysis.

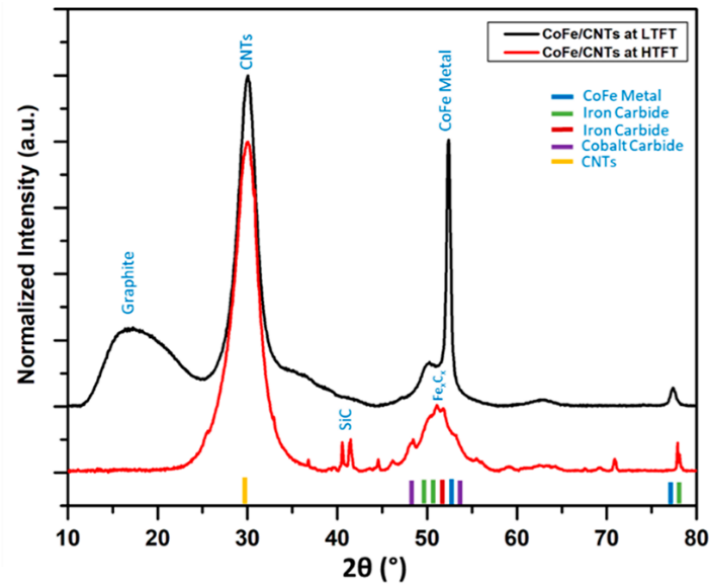

Figure 16. XRD image of CNT supported FeCo catalyst after LTFT and HTFT [64].

The similar core-shell model of bimetallic Fe-Co nanoparticle was observed under FTS conditions by Calderone et al [48]. As can be seen in Figure 17, which is a HRTEM image of this bimetallic nanoparticle, it is evident that the cobalt concentration in the shell is greater than that in the core, while the iron is found in the core on the bimetallic nanoparticles. Furthermore, it was proposed that Fe segregated to the topmost layers of the cobalt surface, and that leading electronic modification was the likely cause of differences in selectivity in FeCo catalysts compared to cobalt catalysts. Similarly, the synthesis of bimetallic FeCo nanoparticles involved the thermal decomposition of organometallic complexes, as described by Mourdikoudis [60]. The composition of these nanoparticles, featuring an FeCo alloy core and an oxidic FeCo phase ($CoFe_2O_4$), was confirmed through HRTEM and XRD techniques. They did not find any evidence of the existence of monometallic metal phases in the bimetallic iron-cobalt nanoparticles. However, they observed an increase in the oxidized layer of bimetallic FeCo nanoparticles after exposure to air, and further increases in the oxidized layers were observed with extended the storage in the air. This led to the degradation of magnetic properties of the bimetallic FeCo catalyst.

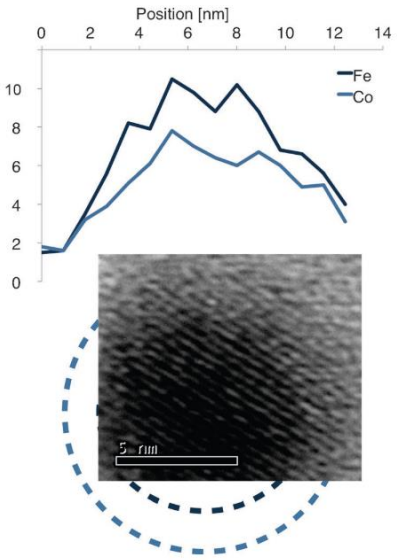

Figure 17. The inner structure of a core-shell structure of bimetallic Fe-Co nanoparticle, as obtained using HRTEM [48].

To overcome the experimental challenges, DFT calculations are extensively employed to establish relationship between catalytic activity and the structures of metal surfaces. In the case of bimetallic FeCo catalysts, distinct active phases can be obtained through variations in metal concentrations, catalyst preparation methods, and activation conditions of the catalysts. As a computational study, the alloy of Fe and Co was investigated using DFT calculations with Perdew-Wang 91 (PW91) functional by Rochana and Wilcox [66]. They utilized both body-centered cubic (bcc) and FeCo(100)-Co, which represents the Co atoms comprising the top layer, and FeCo(100)-Fe, which represents the Fe atoms comprising the top layer of the catalyst. They found that FeCo(100)-Fe surface is more stable than FeCo(100)-Co at the zero temperature and pressure conditions. Additionally, they demonstrated that the formation of bimetallic FeCo alloy phase occurred with bulk atomic Fe concentrations ranging from 25 to 75% at temperatures of 200-350ºC. They demonstrated bimetallic FeCo nanoparticles adopt the fcc phase of cobalt that for low iron concentrations.

The effect of metal ratio on activity and selectivity of carbon nanotube (CNT) supported bimetallic FeCo catalysts in FTS was investigated by Tavasoli et al [67]. Their study revealed the formation of Fe-Co alloys within the carbon nanotubes and the reduction ability of small amounts of iron in bimetallic catalyst. The preparation and reduction procedures of catalysts have a significant impact on both the bulk and the surface properties [68]. Furthermore, several experimental studies indicate that the

structure of the catalyst highly depends on the gas mixture used in the activation process [60,69].

The diverse conditions lead to the formation of different phases on the catalyst and, in turn, varying yields of products. This has been extensively investigated with a range of parameters in previous studies. For instance, Numpilai et al. revealed that the calcination temperature had an substantial effect on the catalyst structure and its product selectivity in CO_2 hydrogenation [44]. Furthermore, a calcination temperature of 400^oC was determined to yield of high CO_2 conversion (49%), a substantial yield of CH_4 (23%) and light olefins (18.1%), and a low yield of CO (9.4%) when compared to higher calcination temperatures. These outcomes were attributed to the formation of small metal oxide nanoparticles and the enhanced reducibility of iron oxides. Consequently, this led to the formation of shorter activation periods due to a higher formation of the iron carbide phase.

2.2. Catalytic Performance of Fe-Co Catalysts in CO- and CO_2-based FTS

In catalysis, the catalytic performance of a catalyst can be characterized by several key properties of the catalyst, including activity, selectivity and stability. The catalytic behaviour of monometallic Co- and Fe-based catalyst in CO and CO_2 hydrogenation have been extensively studied in the literature. For instance, Riedel and Schaub investigated the catalytic performance of K-promoted Fe catalyst in CO_2 hydrogenation [39]. Based on their results, paraffin and olefin products were obtained in the range of 300-360^oC. They also demonstrated that CO_2 hydrogenation occured through two steps: CO_2 reduction to CO and hydrocarbon production from CO on the iron catalysts.

In some studies, researchers have observed that bimetallic FeCo catalsyts display high activity and high selectivity towards valueable products. For instance, Toncón-Leal et al. conducted research on mesoporous silica (SBA-15) supported FeCo bimetallic catalysts and found that they enhanced catalytic activity under FTS conditions [49]. This was accompained by a decrase in methane selectivity and an increase in the production of gasoline and C_{10+} hydrocarbons in comparison to monometallic iron and cobalt catalysts, while lowering the formation of coke. In another study, Zhang et al. investigated

the catalytic performance of Na-promoted CoFe alloy catalysts in CO_2 hydrogenation [34]. They found that when the Na concentration reached to 0.81%, the highest selectivity toward jet-fuel was achieved at 64.2%, while methane selectivity decreased. They also demonstrated that as increase in the space velocity of feed gas, the selectivity towards C_{8+} and CO_2 conversion were substantially enhanced, as shown in Figure 18a. Concerning the variation in reaction temperature during CO_2 hydrogenation, it was observed that the catalytic activity decreased with a reduction in reaction temperature. In contrast, the selectivity towards C_{8+} increased, reaching a high selectivity at 240°C and 3 MPa. They also suggested that CoFe alloy phase was responsible for the formation of C_{2+} products from CO, through both experimental and computational results.

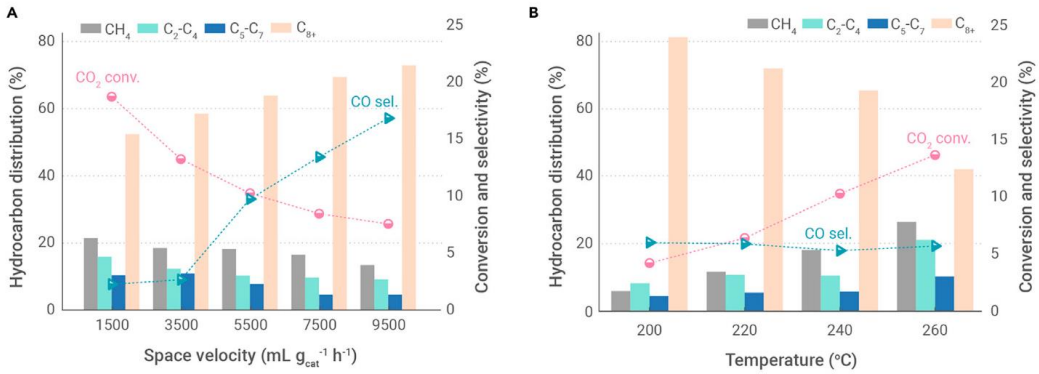

Figure 18. The catalytic performance of bimetallic FeCo catalaysts for CO_2 hydrogenation varies with space velocity (a) and reaction temperature (b), affecting conversion, selectivity and hydrogen distribution. Adapted from [34].

In another study, Satthawong et al. conducted an investigation on alumina supported bimetallic FeCo catalysts with different metal ratios for CO_2 hydrogenation, utilizing a CO_2:H_2 ratio of 1:3 at 573 K and 1.1 MPa [70]. They noted that an increase in the Co content within bimetallic FeCo catalysts led to an enhanced CO_2 conversion and methane yield, while decreasing the yields of CO and C_{2+} products. Furthermore, it was observed that the utilization of K as a promoter in bimetallic catalysts resulted in enhanced CO_2 conversion, increased yields of C_{2+} products, and reduced yields of methane and CO products. This was observed in comparison to the unpromoted bimetallic catalysts with the same metal ratio in the same study. In another study, same authors

demonstrated that the addition of potassium led to a decrease in the adsorption strength of hydrogen while enhancing the strength of CO_2 adsorption on bimetallic FeCo catalyst surface [71]. This led to improved CO_2 conversion and an increased yield of light olefins.

Due to the distinct catalytic properties of phases on the bimetallic catalysts, Gnanamani et al. demonstrated that the ratio of the metals significantly affected catalyst performance, inducing varied effects on the reaction kinetics [51]. With the addition of 10% Fe to cobalt-based catalysts, there was a notable increase in paraffin (C_2-C_5) selectivity, rising from 4% to 20%. However, when 50% Fe was added, selectivities for CO and oxygenates increased, while methane selectivity decreased. They also observed that when Fe ratio exceeded 50%, the positive impact on product selectivity decreased. This indicated a shift in selectivity from relatively heavy hydrocarbons toward lighter hydrocarbons. Therefore, they suggested that the optimal composition for the bimetallic Fe-Co catalyst was 50% Co and 50% Fe.

Bimetallic FeCo nanoparticles including high iron contents are commonly represented by iron oxide or carbide phases. Therefore, the effect of cobalt doping on iron catalysts was investigated both experimentally and computationally by Wang et al [65]. They proposed that Co-doping on K-promoted Fe-based catalysts modify the catalytic performance by increasing activity and selectivity towards CH_4, olefins, and C_{5+} hydrocarbons. The authors also investigated the adsorption energies of key intermediates, including CO_2, CO and H_2, on both pure and Co-doped Fe and K-promoted Fe oxide/carbide surfaces by DFT modeling in the same study. These surface phases have commonly been considered for bimetallic FeCo catalysts with a substantial iron concentration in the literature. They found that binding strength of CO_2 and CO was increased with cobalt doping on iron surface, while decreased the binding of H_2 on iron oxide surfaces. In the context of the iron carbide phase, Co-doping resulted in an increase in the adsorption strength of H_2 in contrast to the iron oxide phase. They demonstrated the hydrogen dissociation is increased by the addition of Co. However, the main effect contributing to the enhanced C_{5+} hydrocarbon selectivity was attributed to the presence of K as a promoter. This effect was achieved by increasing surface basicity and promoting the formation carbide and oxide phases of iron. In another computational study, Wong et al. suggested that predominance of C-C coupling over CO formation was responsible for the initiation of carbon graphitization on fcc Co(111) surface [17].

In another study, Sandupatla et al. demonstrated that 10% Fe-doped cobalt catalysts supported on alumina increased yield of methane while reducing CO yield at 250^{o}C and

1 bar pressure [63]. According to the XRD and TPR results, the addition of Fe on Co enhanced the reducibility of cobalt oxides to metallic phase of cobalt. They also conducted DFT calculations for the direct dissociation of CO_2. The presence of 0.11 ML Fe on Co(111) surface resulted in a 13 $kJ.mol^{-1}$ increase in activation energy, shifting it from 34 $kJ.mol^{-1}$ to 47 $kJ.mol^{-1}$, as determined through DFT calculations. In another experimental study, Ischenko et al. investigated the effect of iron on cobalt catalysts in the CO_2 methanation. They found that Fe-doping resulted in a decrease in catalytic activity, while shifting the product selectivity from methane into CO on the bimetallic surface. Furthermore, Wang et al. suggested that the fcc Fe facets played significant role in the formation of key intermediates and in changing the reaction pathways for the conversion of carbon dioxide. This finding showed that the equilibrium of co-adsorption of carbon dioxide and hydrogen was crucial for activation of reactants. In the same study, (111) and (211) facets of monometallic Fe nanoparticle were found as more suitable surfaces for CO_2 adsorption.

Until recently, the effect of Fe on Co surface in terms of selectivity has been a topic of controversy. Experimental studies demonstrate that various product selectivities can be obtained in CO_2-based FTS with FeCo bimetallic catalysts. However, experimental determination of the specific facets responsible for the observed product selectivity, as well as the identification of facets prone to yield the desired target products, remains unsolved. Since these bimetallic catalysts have different facets, morphology and phases exhibit different activity, stability and selectivity due to the different electronic structures of the catalyst surface. In the literature, XRD techniques are used to gain insight into the phases of the catalyst nanoparticles. This reveales that bimetallic FeCo catalysts can exist within FeCo alloy, metallic phase, oxidic phase, and carbide phases of the metals under reaction conditions. As mentioned, several experimental studies have reported enriched selectivity to different products on bimetallic iron-cobalt (FeCo) catalysts for CO_2 hydrogenation [39,65,70]. However, the selectivity behavior observed in different studies contradicts each other, and the structure of catalytically active phases and surface structures are poorly understood. In line with this scientific need, the aim of this study is to identify the relationships between the structure of bimetallic FeCo catalysts at the atomic scale and their selectivity behavior.

CHAPTER 3

COMPUTATIONAL METHODOLOGY

3.1. Overview of the Methodology

All quantum chemical calculations were performed using periodic spin-polarized density functional theory (DFT) calculations with the projector-augment wave (PAW) method, using the Vienna *Ab-Initio* Simulation Package (VASP) [56,72]. The exchange-correlation energy was calculated with the revised Perdew-Burke-Ernzerhof functional (revPBE) including the non-local van der Waals density functional (vdW-DF) correlation [73]. The usage of vdW-DF allowed for the accurate calculation of the adsorption energy of CO_2 and also enabled the prediction the experimentally observed adsorption site and energy for adsorbed CO on the cobalt surface [74]. The kinetic energy cutoff for the plane wave basis set was established at 500 eV. A Monkhorst-Pack mesh k-points of (3x3x1) was used for the fcc surface slabs [75]. To prevent dipole-dipole interactions between the supercells in the z-direction on Co(111) and FeCo(111) surface slabs, calculations were carried out mirrored over the xy-directions. Therefore, a 15 Å vacuum region was place above the slabs.

The fcc phase which has been experimentally observed in Co particles which dimensions less than 100 nm was selected [76]. The lattice parameter of the optimized bulk surfaces, obtained using the vdW-DF functional, was found to be 3.56 Å, in agreement with the experimental value of 3.55 Å and the computationally derived value of 3.56 Å, which was optimized using vdW-DF functional. The terrace (111) plane, which represents the predominant plane within the p(3x3) fcc was adopted as a catalyst model [45].

In terms of the bimetallic surface model, cobalt-rich bimetallic FeCo catalysts were modeled using an fcc lattice. This choise is based on the literature survey, which indicates that cobalt-rich bimetallic FeCo catalysts preserve the crystalline structure of cobalt catalysts. Since it has been proven by characterization methods in experimental studies

that bimetallic FeCo catalysts containing low Fe content have a Fe-enrichment surface, a model was created in the bimetallic surface model, including the top layer Fe atoms, as will be detailed in the following sections [48,60,64]. The catalytic effects of the bimetallic surface were examined in detail by changing the Fe coverage in this study. Moreover, the four-layer Co(111) and 1 ML Fe Co(111) surface models were chosen, which have been demonstrated to be reasonable for investigating the adsorption and reaction mechanisms. Zero point energies (ZPE) were not included in the activation and reaction energies, as their impact was found to be negligible.

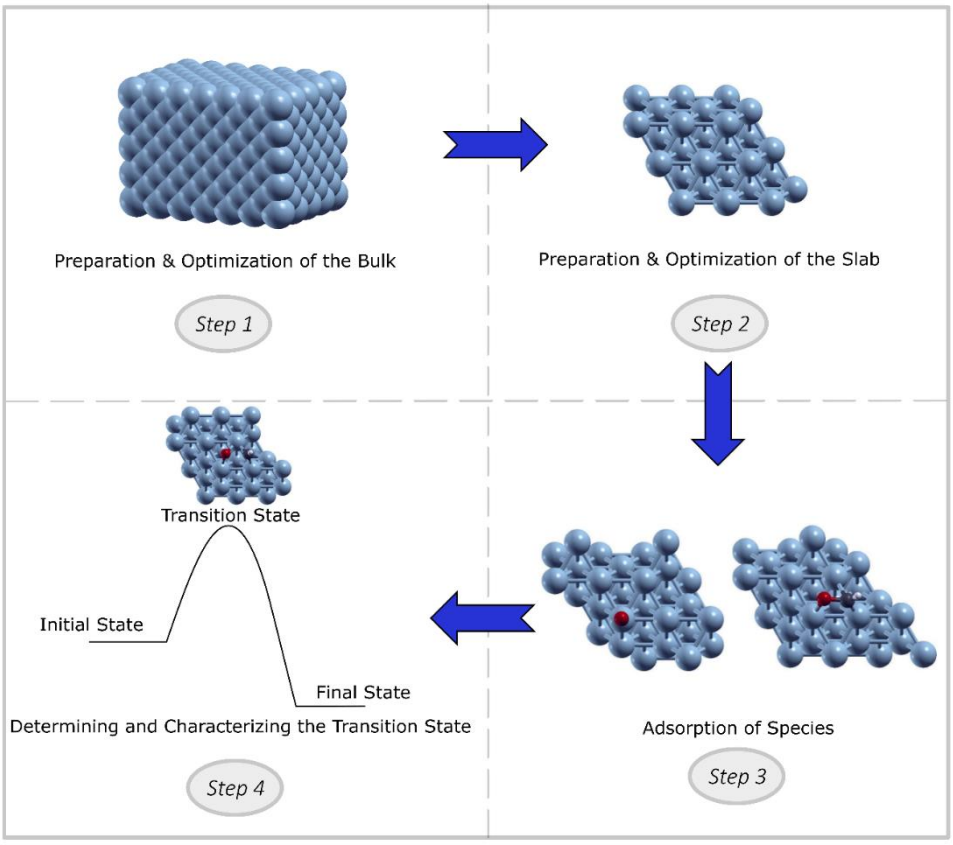

Figure 19. Four steps for computational modeling of catalyst systems.

For computational calculations of catalyst systems, the process begins with the computational preparation and optimization of the bulk catalyst. Subsequently, a catalyst surface is extracted from the bulk metal catalyst and further optimized using a specific DFT functional. On the optimized surface, the adsorption of species is modeled. Then, transition states for each elementary reaction are identified using initial and final state geometries. Vibrational frequency analysis is then conducted for each transition state

geometry to identify a single imaginary frequency, signifying the formation or breaking of a chemical bond. The general procedure steps for the calculations of the catalyst systems are summarized in Figure 19.

3.2. Preparation and Optimization of the Bulk Structure

The fcc cobalt crystal bulk structure with a lattice parameter of 3.56 Å (a=b =c) was used for the preparation of monometallic and bimetallic surfaces. From this bulk system, surface models can be constructed for conducting DFT calculations. Figure 20 illustrates the fcc cobalt phase as a representative image.

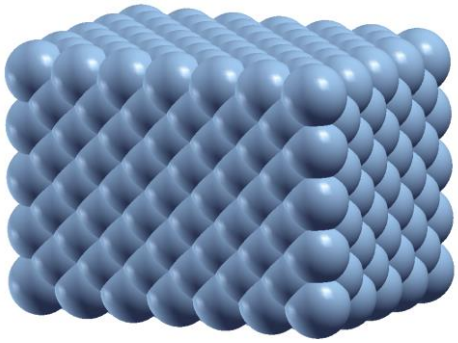

Figure 20. Representative image of bulk fcc cobalt.

3.3. Preparation and Optimization of the Slabs

The periodic slab models are good approximations for large metal nanoparticles that are higher than almost 5 nm [52]. These models are the mainstay for the model of heterogeneous catalysts.

In computational studies in the literature, generally 4 or 5 catalysts layers are used to form the metal catalyst surface model [77,78]. The optimization of the number of atomic layers was conducted based on the adsorption energy of carbon monoxide on the (111) facet of the cobalt catalyst. Therefore, Co(111) and FeCo(111) surfaces with four atomic layers were modeled in this study.

The view of unit cell of FeCo(111) slab in three dimensions is given in Figure 21. A vacuum region was employed to inhibit interactions between repeated unit cells in the z-direction. In all DFT calculations conducted in this study, the bottom two layers of the slab were held fixed, while the other layers (top two layers) were allowed to relax.

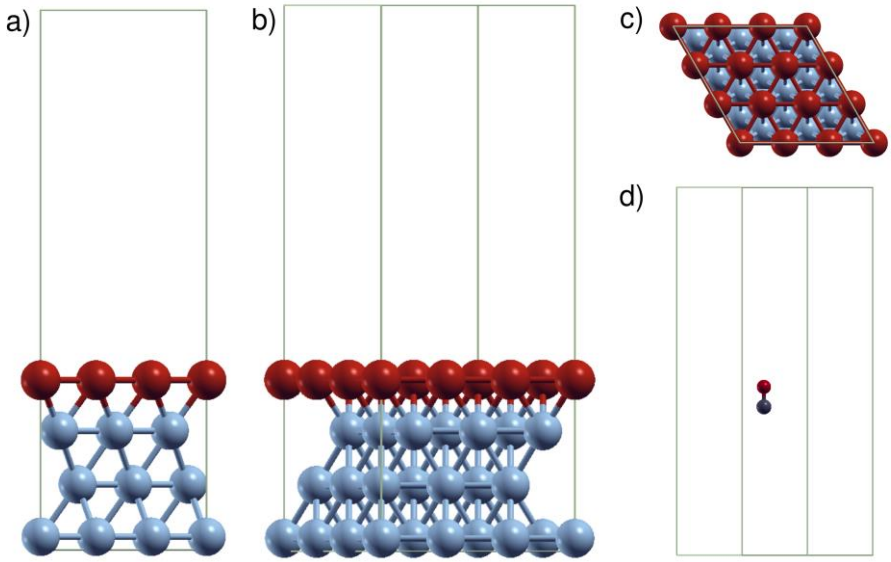

Figure 21. A 3x3 FeCo(111) unit cell view from the x-direction (a), y-direction (b), and z-direction (c) and the view of gas phase CO molecule in vacuum (d).

3.4. Calculation of the Adsorption Energies and the Kinetic Parameters of Elementary Reactions

Adsorption is the process in which molecules or atoms from a gas or liquid adhere to the solid surface. The interaction between adsorbate and adsorbent can be either physical or chemical, depending on the strength of the bonds involved. Coadsorption occurs when two or more adsorbates are located on the catalytic surface.

In this study, the adsorption energy (E_{ad}) and the coadsorption energy ($E_{co\text{-}ad}$) was calculated using Equation 3.1 and 3.2. The adsorption and coadsorption energies are defined as following:

$$E_{ad} = E_{A\text{-}M} - E_M - E_A \quad (3.1)$$

$$E_{co\text{-}ad} = E_{A/B\text{-}M} - E_M - E_A - E_B \quad (3.2)$$

where $E_{A\text{-}M}$, $E_{A/B\text{-}M}$, E_M, E_A, and E_B were calculated energies of the individual adsorption of species on the slab, the coadsorption of species on the slab, the energy of the pure slab, and the energy of adsorbate in the gas phase, respectively.

In catalysis, the reaction energy (ΔE) and the activation energy (E_a) on the catalyst surface can be calculated using Equation 3.3 and 3.4, respectively.

The reaction and activation energies are defined as following:

$$\Delta E = E_{FS} - E_{IS} \quad (3.3)$$

$$E_a = E_{TS} - E_{IS} \quad (3.4)$$

where ΔE, E_{IS}, E_{TS}, and E_{FS} represent the reaction energy, the energies of the initial state, transition state, and final state, respectively. Specifically, the initial state corresponds to the presence of reactants on the surface, the transition state represents the minimum energy point during the reaction between surface species, and the final state corresponds to the state of the reactants.

Transition state (TS) calculations were performed using the climbing nudged elastic band (CI-NEB) method as implemented in VASP by Henkelman et al. [41]. The convergence criteria was set to be less than 0.1 eV/Å. All transition states are further validated by vibrational frequency analysis showing a single imaginary vibrational frequency. During the vibrational frequency analysis, the atoms were displaced from their equilibrium positions by 0.015 Å.

CHAPTER 4

RESULTS & DISCUSSION

In this study, the conversion of CO_2 into C_1 products was investigated on Co(111) and FeCo(111) surfaces based on DFT modeling. Single carbon products are not only clean fuels (e.g. methanol and formic acid) but also building blocks to generate heavy hydrocarbon products. In this perspective, the reactions of the formation of C_1 products that are CO, methane, formic acid, and methanol were examined in this computational study.

4.1. The Selection of the Catalyst Surface Model

The choice of realistic catalyst model has an significant importance to obtain experimentally observable results. The model should accurately represent a surface that either exists or can be feasibly produced under experimental conditions.

To explore the effect of Fe coverage on the surface, 0 ML, 0.11 ML, 0.33 ML and 1 ML Fe covered surfaces were examined. As presented in Figure 22, these surfaces contain 0, 1, 3, and 9 iron atoms on the topmost layer of the slab, respectively.

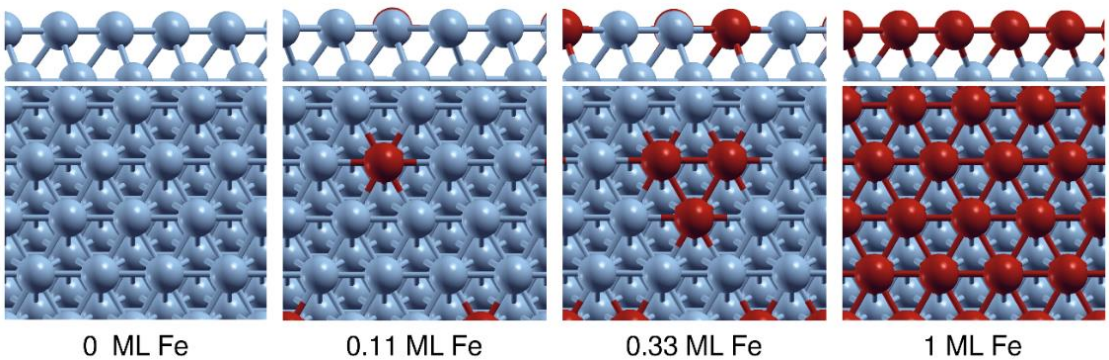

Figure 22. The side and top views of various FeCo(111) surfaces.

On these catalysts models, the adsorption strength of major adsorbates (i.e. CO, H, C, and O) and the change in the electronic charge of the surfaces were examined as a function of Fe coverage to determine an optimum surface model for bimetallic FeCo catalyst. Details about these are explained in the following sections.

4.1.1 Effect of Iron Coverage in the Electronic Charge of the Bare FeCo(111) Surface

The surface charge of Fe or Co atoms on the surface plays an important role in the selectivity and activity of the catalyst. Therefore, Bader charge analysis was performed to investigate the electronic properties of adsorbates and adsorbents [43–45]. Moreover, the total Bader charges of pure Co(111) and Fe doped with 0.11 ML, 0.33 ML and 1 ML Co(111) surfaces were calculated to understand the how charge distribution changes with varying Fe coverage on the cobalt catalyst surface.

The surfaces presented in Figure 23 exhibit different electronic charge on the slab surface due to variability in the electronic properties of iron atoms. As can be seen Figure 23, the electronic charge on individual iron atoms changed with the variation in iron coverage.

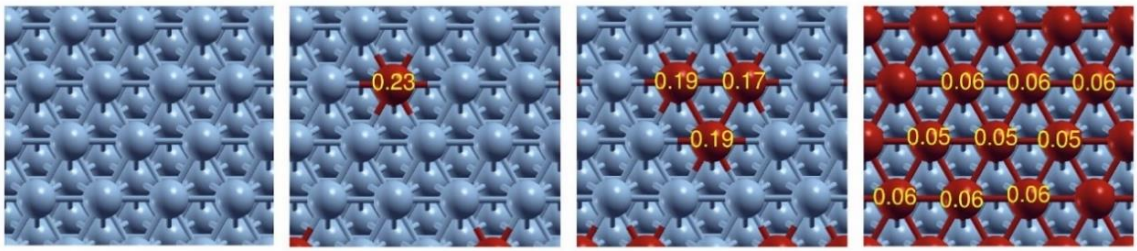

Figure 23. The electronic charge of the individual iron atoms on the various iron covered cobalt surfaces and the charges of the topmost two layers specified within parantheses.

Due to the relatively high electronegativity of Co, Fe atoms donated their electrons to Co, in other words, Co atoms attracted valence electrons from Fe atoms. Therefore, the alteration in the charge of the surfaces was occured in the bimetallic FeCo surfaces, as seen in Figure 23. This figure also demonstrates that the electronic charge of individual Fe atoms on Fe-doped cobalt surfaces is shown with different Fe ratios. It was found that the Fe atoms became positively charged on the Co surface, and the charge value of the individual Fe atoms increased as the Fe coverage on the surface increased. Furthermore, the total charge of the topmost two layers of the catalyst slab, which interact almost completely with the adsorbates and determine their charges, increased with an increase in the Fe coverage, from 0 ML to 1 ML.

4.1.2. Effect of Iron Coverage on the Adsorption Strength of Surface Species on the FeCo(111) Surface

The alteration in the charge density of the slab influences the adsorption strength (or adsorption energy) during catalysis. Therefore, the change in the adsorption energies of major intermediates such as CO, H, O, and C was calculated on bimetallic surfaces with different Fe ratios. The adsorption energies of these species on bimetallic surfaces were collected in Table 1. It was observed that as the iron coverage increased from 0 ML to 1 ML, the adsorption energy of H and O also gradually increased. Although the same behavior in adsorption energy was observed for C and CO, it showed a decrease on the 0.11 ML Fe-doped Co(111) surface. Thus, the highest adsorption energies of these species were obtained on the 1 ML Fe-doped Co(111) surface, which has the highest number of electron-donating Fe atoms. These results clearly show that there is a relationship between surface coverage and adsorption energy. In particular, an increase in the adsorption strength of CO on Fe atoms leads to an increase in the adsorption of CO molecules on the bimetallic FeCo(111) surface compared to the monometallic Co(111) surface. With the increase in the surface CO coverage, CO molecules enhance the surface segregation of Fe atoms on the cobalt catalyst.

Table 1. The change in adsorption energies (kJ.mol^{-1}) of key adsorbates (H, O, C, and CO) with the change in iron coverage of the surface.

Adsorbates	E_{ad} on Fe-doped Co(111) Surfaces			
	0 ML	0.11 ML	0.33 ML	1 ML
H	-277	-280	-290	-303
O	-564	-568	-607	-622
C	-617	-595	-622	-675
CO	-132	-123	-135	-173

Consequently, bimetallic FeCo surface model was optimized by exploring various ratios of iron covered surfaces and investigating the connection between adsorption energy of key species and surface coverage of iron. Based on these results, the surface model containing 1 ML Fe surface coverage for the Co-rich bimetallic FeCo catalyst was determined in this study.

4.2. Adsorption Energies of Surface Species Involved in CO_2 Hydrogenation to C_1 Products on the 1 ML Fe-Doped Co(111) Surface

The catalytic performance and active sites of the catalyst are affected by surface species on the surface of catalyst. Therefore, the adsorption energies of the intermediates formed during the reactions mentioned in the next section were calculated on the selected model, the 1 ML Fe-doped Co(111) surface. These examined intermediates are H, C, O, OH, CO, CO_2, H_2O, CH, CH_2, CH_3, CH_4, HCO, COOH, HCOO, H_2CO, H_3CO, and H_3COH. To model elementary reactions, the first step is to identify the most stable adsorption sites for these intermediates on both Co(111) and FeCo(111) surfaces. On the (111) surface, there are four possible adsorption sites: top, fcc, hcp, and bridge sites, as shown in Figure 24. A bridge site is also available on the (111) facet. However, the bridge site was not found to be stable for intermediates investigated in this study.

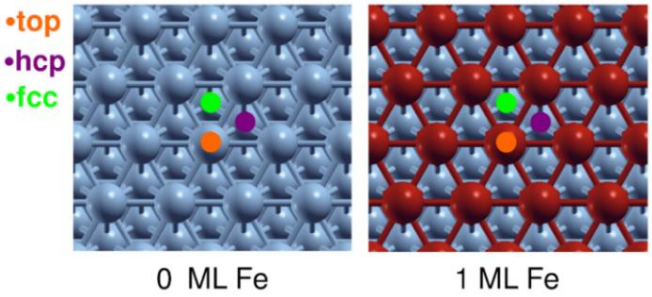

Figure 24. The adsorption sites investigated on Co(111) and FeCo(111) surfaces.

Adsorption energies of the surface species were computed at all four possible sites to determine the most stable site for each species. Figure 25 illustrates the relationship between the adsorption site and adsorption energy based on the stable site. Among all the surface species, H, C, O, OH, and CO are considered key species as they constitute the building blocks of all other species involved in the elementary reactions of CO_2 hydrogenation.

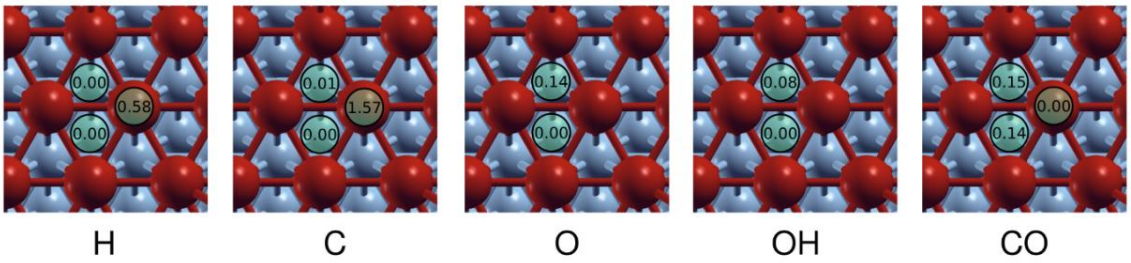

Figure 25. Relative adsorption energies of H, C, O, OH, and CO on top, fcc, and hcp sites of FeCo(111) with respect to their most stable site.

Due to its stability on the sites, atomic hydrogen was favored to adsorb on hollow sites, namely the hcp and fcc sites on the FeCo(111) surface. The migration of atomic hydrogen from a hollow site to the less stable top site required an energy of 58 $kJ.mol^{-1}$. Regarding the adsorption of atomic carbon, the migration of the atom from a more stable hollow site to the less stable top site required an energy of 157 $kJ.mol^{-1}$. For the adsorption of atomic oxygen and hydroxyl, the top site was not favored because it is highly unstable compared to the hollow sites. In terms of the adsorption of carbon monoxide, the fcc site required an energy of 14 $kJ.mol^{-1}$, while the hcp site required an energy of 15 $kJ.mol^{-1}$ for

migration from the stable top site. The most stable sites for the key intermediates were found to be consistent both on the Co surface and the bimetallic surface, as shown in Table 2.

Moreover, the most stable adsorption site or geometries may also change in some intermediates, namely CH and HCO, due to the change in the charge of the bimetallic catalyst slab. Figure 26b shows that the atoms of the HCO molecule tended in different directions on bimetallic FeCo surface compared to the monometallic Co surface.

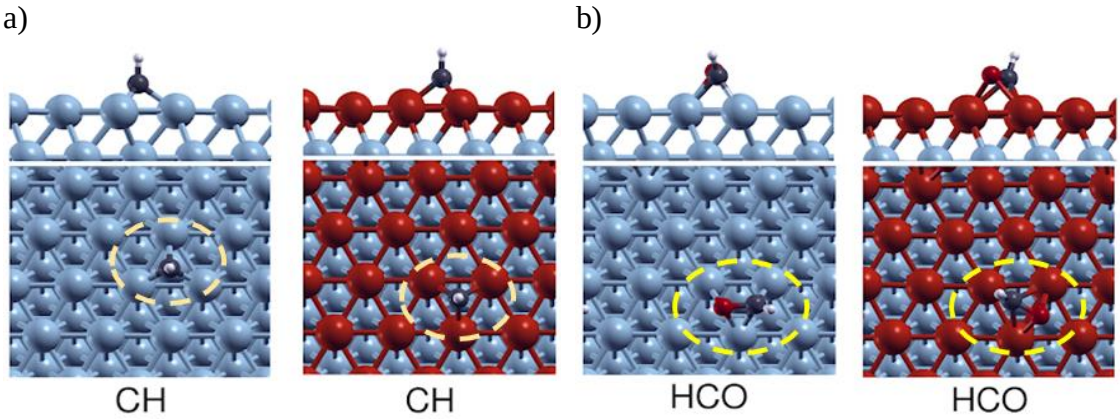

Figure 26. Example of the difference in adsorption sites and geometry of CH (a) and HCO (b) intermediates on Co(111) and FeCo(111) surfaces.

As shown in Table 2, the introduction of 1 ML Fe on the Co(111) surface resulted in increased adsorption energies of all the chemisorbed and physisorbed surface species, except the adsorption energy of physisorbed H_2. The difference in E_{ad} for physisorbed species ($\leq$ 40 kJ.mol^{-1}), such as H_2 was found to be lower than that of chemisorbed species. For instance, CH_4 was physically adsorbed at the identical adsorption site on the FeCo(111) surface with the equivalent adsorption energy to that observed on the Co(111) surface.

Table 2. Calculated adsorption energies ($kJ.mol^{-1}$) with adsorption sites of all intermediates in CO_2 hydrogenation on Co(111) and FeCo(111) surfaces.

Species	Co(111)	FeCo(111)	ΔE(%)
H	-278 (fcc)	-302 (fcc)	9
C	-671 (hcp)	-675 (hcp)	9
O	-564 (hcp)	-635 (fcc)	13
CO	-132 (top)	-173 (top)	31
CO_2	-19 (bridge via C)	-29 (bridge via C)	53
H_2	-6 (top)	-6 (top)	0
OH	-329 (hcp)	-368 (fcc)	12
CH	-561 (hcp)	-615 (fcc)	10
CH_2	-362 (fcc)	-413 (fcc)	14
CH_3	-166 (hcp)	-198 (fcc)	19
CH_4	-14 (top)	-14 (top)	2
H_2O	-28 (top)	-47 (top)	68
HCO	-187 (bridge via O)	-255 (hcp via O)	36
COOH	-211 (bridge via C)	-257 (bridge via C)	22
HCOO	-311 (bridge via C)	-364 (bridge via C)	17
H_2CO	-58 (fcc via O)	-125 (fcc via O)	116
H_3CO	-284 (hcp)	-330 (fcc)	16
H_3COH	-39 (top via O)	-62 (top via O)	59

In the context of the adsorption energies for H, C, and O, the difference in adsorption energies of monoatomic intermediates between Co(111) and FeCo(111) was found to be insignificant, increasing by 9%, 9% and 13%, respectively. The adsorption energy for CH on Co(111) and FeCo(111) was calculated to be -561 and -615 $kJ.mol^{-1}$, respectively, representing a change of 10%. In terms of the adsorption of the CO molecule, which is one of the key surface species, a 31% increase was calculated with the presence of iron on cobalt. The highest increase in adsorption energy was observed for H_2CO intermediate, where the adsorption energy with a 116% increase for the FeCo(111) compared to Co(111). For HCO, COOH, and HCOO, the adsorption energies increased by 36, 22, and 17%, respectively. The increase in the adsorption energy of CO_2 by 53% on FeCo(111) showed that the addition of iron on the cobalt surface increased the strength of the adsorption of the feed gas. Regarding the adsorption strength of H_2O, a relatively high increase was observed by 68% with the addition of Fe on Co(111) surface. These results indicate that the binding strength of oxygenated intermediates, such as CO_2 and H_2O, is increased with the additive Fe on the catalyst surface. On the other hand,

hydrogenated species such as OH and CH_x exhibit a relatively modest increase in the adsorption energy on the bimetallic catalyst, ranging from 10% to 19%.

Both top and side images of the adsorption geometries corresponding to the adsorption energies calculated for Co(111) and FeCo(111) surfaces in Table 2 are given in Figures 27 and 28, respectively.

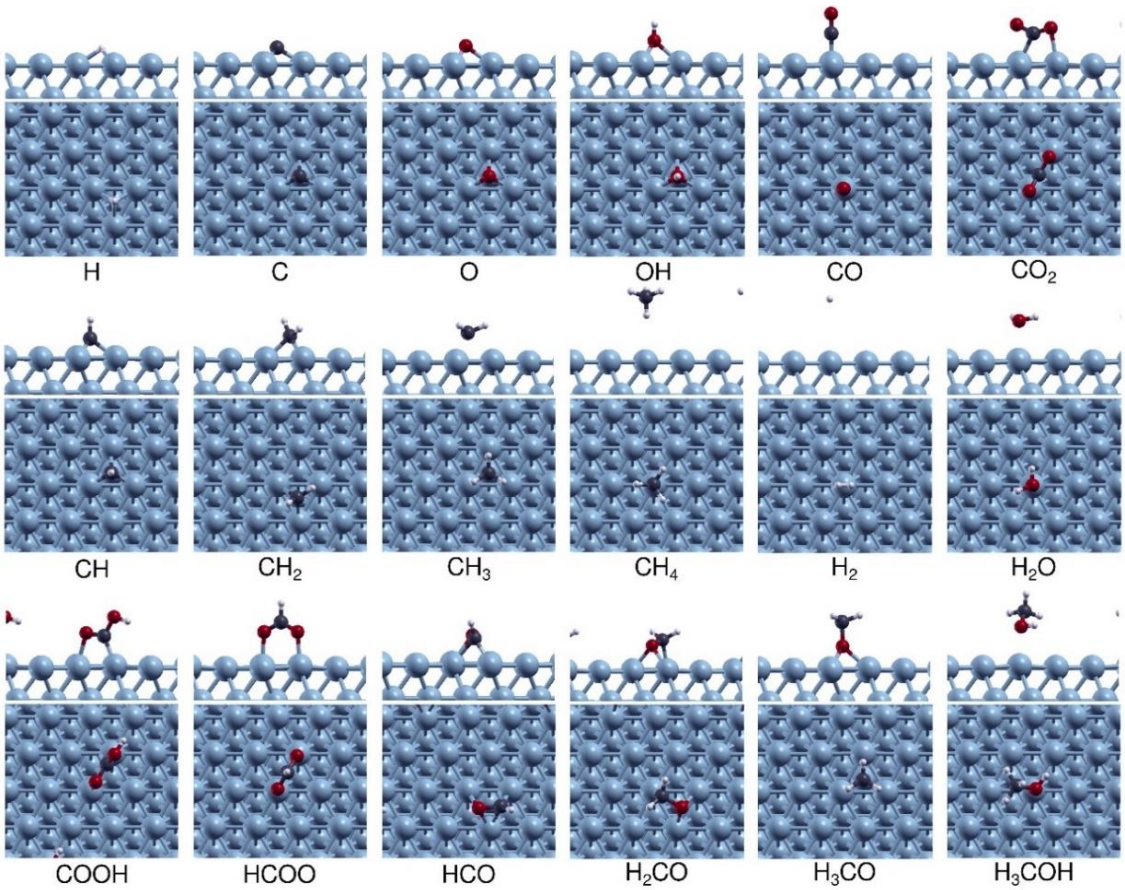

Figure 27. The most stable adsorption configurations of species on the Co(111) surface. Gray, red, white, blue, and dark red spheres represent C, O, H, Co, and Fe atoms, respectively.

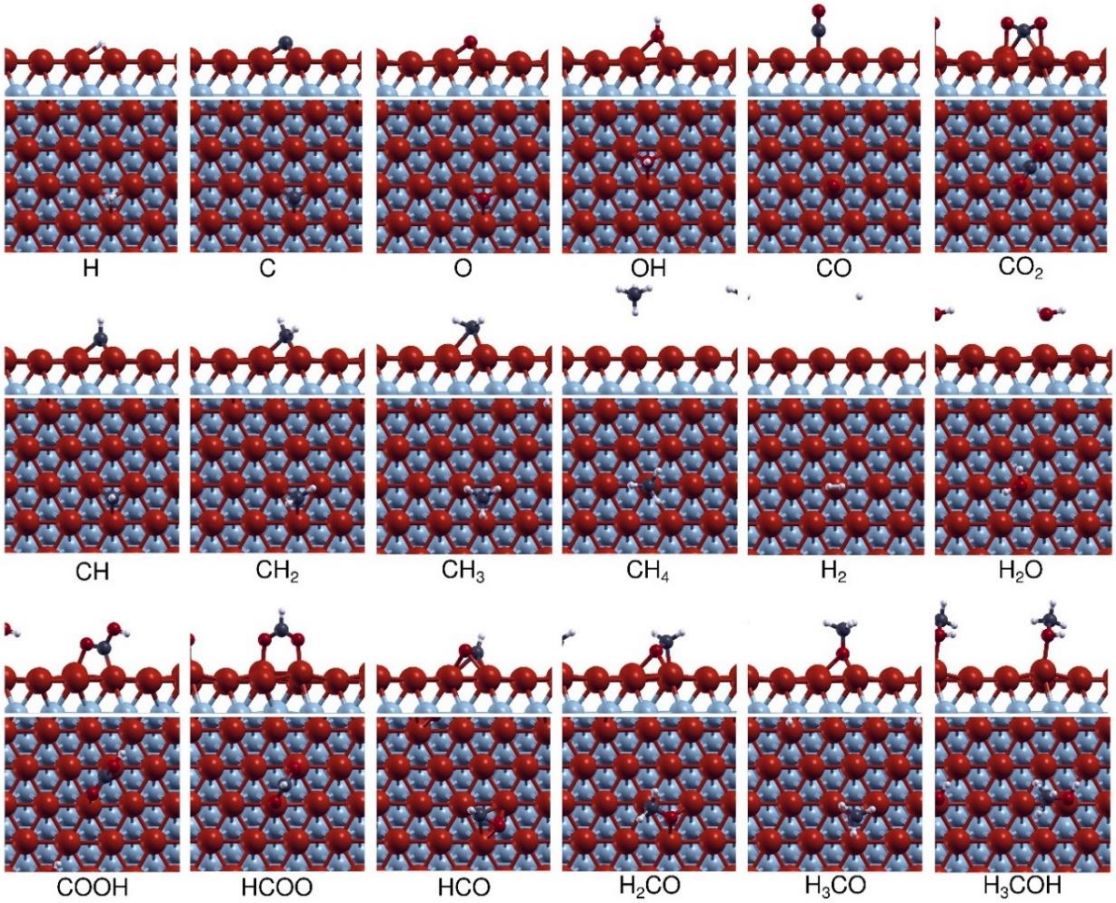

Figure 28. The most stable adsorption configurations of species on the FeCo(111) surface. Gray, red, white, blue, and dark red spheres represent C, O, H, Co, and Fe atoms, respectively.

As physisorption is the weak interaction between the surface and adsorbate, it can be easily seen from the side images of the Figure 27 and 28 that the distance between the surface and the physisorbed species, such as methane, water and methanol, was higher than other chemisorbed species.

For OH intermediate, the hcp and fcc sites were found the most stable sites on Co(111) and FeCo(111) surfaces, respectively. The adsorbed CO preferred to adsorb on top site for both surfaces. Similarly, CO_2 was adsorbed on both catalyst surfaces, with C atom occupying the bridge and two O atoms occupying the top sites. A stable CH configuration was found at the hcp site on Co(111) surface, while the most stable site of CH was found at the fcc site on FeCo(111) surface. Adsorbed CH_2 intermediates were observed on fcc sites for both Co(111) and FeCo(111) surfaces, while H_2O intermediates adsorbed on top sites. The adsorption site of CH_3 intermediate shifted from hcp to fcc as

the surface changed from pure surface to the Fe doped surface. For the physisorbed intermediates, namely CH_4 and H_2, the stable adsorption site was found to be the top site. In the case of the adsorption position of the HCO on the FeCo surface, O was positioned on the hcp site while O was positioned on the bridge site on the pure surface. For H_3CO intermediate, the stable site shifted from hcp to fcc as the surface changed from pure surface to the Fe doped surface. In contrast, the stable adsorption sites of COOH, HCOO, H_2CO and H_3COH intermediates remained unchanged with the alteration of the catalyst surface. As previously mentioned, the low energy difference between the hollow sites suggested that, in general, the addition of Fe on the Co surface did not alter the adsorption sites of the intermediates. Nevertheless, the adsorption energies changed considerably with the addition of Fe to the pure Co(111) surface.

These results demonstrate that the surface coverage of CO_2 and CO would increase on the FeCo(111) surface, while the surface coverage of hydrogen and other hydrogenated species would decrease. As surface H and CO coverage depend on each other, an increase in the adsorption energy for CO results in an increase in the CO/H concentration on the catalyst surface.

4.3. Elementary Reactions of CO_2-FTS on Co(111) and FeCo(111) Surfaces

The addition of Fe on Co is anticipated to alter the kinetics of the elementary reactions on the bimetallic catalyst. In this computational study, the mechanism of CO_2-based FTS was examined, encompassing 24 elementary reactions, to investigate the formation of C_1 products. This mechanism involves the dissociation of reactants (carbon dioxide and hydrogen), formation of single carbon products (methane, methanol, formaldehyde and carbon monoxide) and formation of water.

Each elementary reaction was examined on both pure and Fe-doped cobalt surfaces, and the results were compared in terms of activation energy and reaction energy to understand the effect of iron on cobalt catalyst. The activation energies and reaction energies for CO_2-based FTS into C_1 products on Co(111) and FeCo(111) surfaces are given in Table 3. The details of these reactions are provided in the following sections.

Table 3. The activation and reaction energies (kJ.mol^{-1}) of examined elementary reactions on Co(111) and FeCo(111) surfaces.

No	Elementary Reaction	E_a		ΔE	
		Co(111)	FeCo(111)	Co(111)	FeCo(111)
R1	$H_2 \rightarrow H_2$	26	14	13	-9
R2	$H_2 \rightarrow H + H$	28	8	-59	-89
R3	$CO_2 \rightarrow CO + O$	61	17	-77	-154
R4	$CO_2 + H \rightarrow COOH$	94	149	-18	41
R5	$COOH \rightarrow CO + OH$	53	74	-112	-142
R6	$CO_2 + H \rightarrow HCOO$	71	51	-74	-55
R7	$HCOO \rightarrow HCO + O$	107	101	52	6
R8	$CO \rightarrow C + O$	267	173	104	17
R9	$CO + H \rightarrow HCO$	111	114	96	97
R10	$HCO \rightarrow CH + O$	75	45	-43	-114
R11	$O + H \rightarrow OH$	124	168	6	50
R12	$OH + H \rightarrow H_2O$	153	178	44	86
R13	$OH + OH \rightarrow H_2O$	48	40	2	6
R14	$C + H \rightarrow CH$	68	86	-49	-11
R15	$CH + H \rightarrow CH_2$	48	67	12	48
R16	$CH_2 + H \rightarrow CH_3$	45	65	-39	2
R17	$CH_3 + H \rightarrow CH_4$	90	110	-52	0
R18	$HCO + H \rightarrow H_2CO$	44	72	2	22
R19	$CH_2 + O \rightarrow H_2CO$	124	150	48	86
R20	$H_2CO \rightarrow CH_2 + O$	76	73	-48	-71
R21	$H_2CO + H \rightarrow H_3CO$	42	51	-83	-50
R22	$CH_3 + O \rightarrow H_3CO$	141	166	-4	49
R23	$H_3CO + H \rightarrow H_3COH$	160	177	56	94
R24	$CH_3 + OH \rightarrow H_3COH$	196	238	42	89

4.3.1. H_2 Dissociation

The dissociation of H_2 on cobalt surfaces occurs through two sequential elementary reactions. In the first elementary reaction, the far-physisorbed state of H_2 molecule must migrate to a close-physisorbed state on the catalyst surface. In the second elementary reaction, the close-physorbed H_2 dissociates to two hydrogen atoms. These two steps are given in the Equation 4.1 and 4.2, respectively.

$$H_{2\ (far)} \rightarrow H_{2\ (close)} \quad (4.1)$$

$$H_{2\,(close)} \rightarrow H + H \qquad (4.2)$$

The calculated activation energies for the first step on Co(111) and FeCo(111) surface were found as 26 kJ.mol^{-1} and 14 kJ.mol^{-1}, respectively. This suggested that the addition of Fe led to a reduction in E_a for this elementary reaction. Futhermore, this endothermic reaction (13 kJ.mol^{-1}) became an exothermic reaction (-9 kJ.mol^{-1}) with the addition of Fe on cobalt. Regarding the second elementary reaction of H_2 dissociation, the activation energy on FeCo(111) was calculated to be 8 kJ.mol^{-1}, which was 20 kJ.mol^{-1} lower than that on the Co(111) surface, leading to an increase in the exothermicity of the reaction by 30 kJ.mol^{-1}. These E_a and ΔE values are provided in Table 3 and the potential energy diagram (PED) for H_2 dissociation are given for Co(111) and FeCo(111) surfaces in Figure 29.

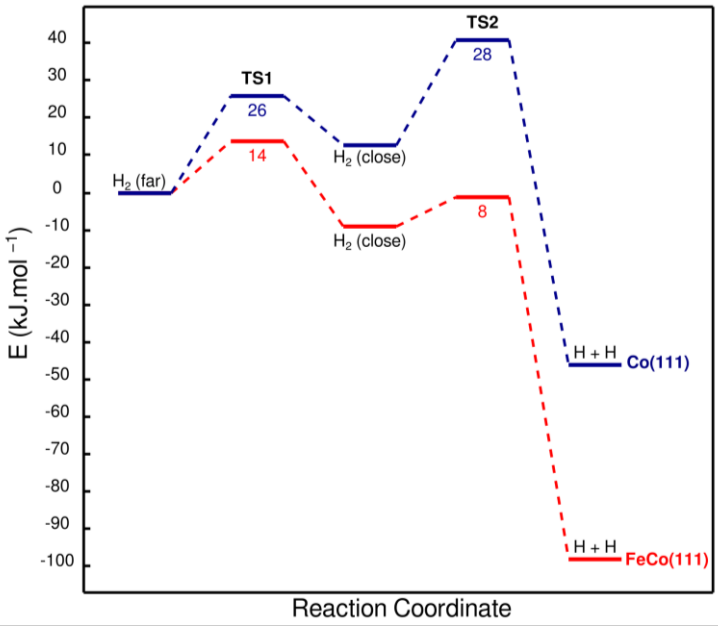

Figure 29. Potential energy diagram for H_2 dissociation on Co(111) and FeCo(111) surfaces.

The initial state (IS), transition state (TS) and final state (FS) geometries of these elementary reactions on both Co(111) and FeCo(111) surfaces are provided in Figure 30 and 31, respectively.

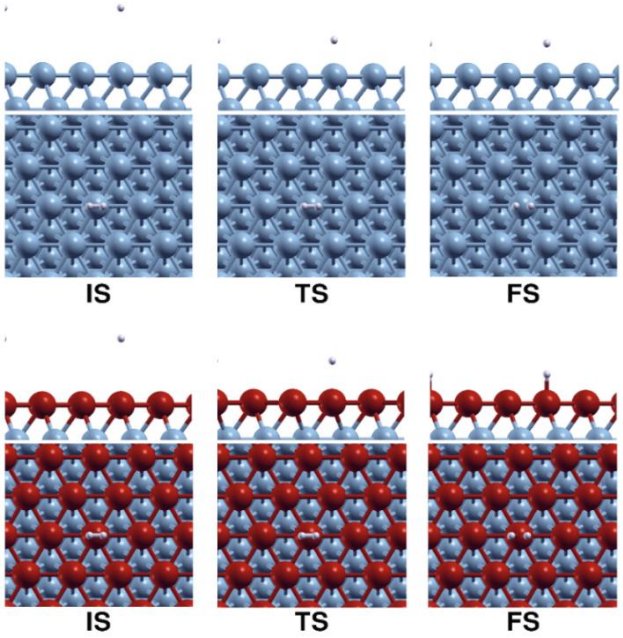

Figure 30. IS, TS and FS for the first step of H_2 dissociation on Co(111) and FeCo(111) surfaces.

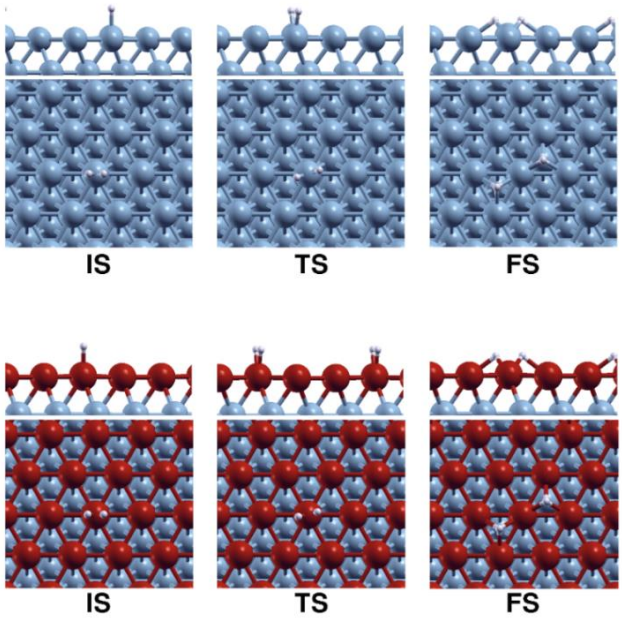

Figure 31. IS, TS and FS for the second step of H_2 dissociation on Co(111) and FeCo(111) surfaces.

These results indicate that H_2 dissociation occured on Fe-doping on Co(111) via the same configurations and mechanims as on Co(111) surface. For this reason, a significant

decrease in the activation energy for H_2 dissociation can be explained by the strong adsorption of hydrogen on bimetallic surface, leading to a increase in exothermicity of these reactions. Consequently, due to the alteration in the activation energies, H_2 dissociation was promoted by FeCo(111) surface. It is important to note that the dissociation of H_2 and its surface coverage is highly depend on the surface coverage of CO on the surface [79,80]. Hence, in this study, the surface ratio of CO/H is an important parameter to comprehend the influence of iron on cobalt catalyst during the catalytic reaction.

4.3.2. CO_2 Dissociation

In the CO_2–based FTS, the primary and crucial step is the dissociation of CO_2, which must occur before it can be converted into hydrocarbons. Carbon dioxide, which is the main reactant and carbon source of this reaction, can be dissociated via direct and H-assisted dissociation mechanisms on cobalt surface [81,82]. The reaction mechanisms and the results of the calculations conducted on these two surfaces are elaborated upon in the subsequent sections.

4.3.2.1. CO_2 Dissociation via Direct Mechanism

In the direct CO_2 dissociation mechanism, the first step involves the dissociation of CO_2 to CO molecule and atomic O, as given in Equation 4.3. This mechanism is also referred as the redox mechanism in the literature.

$$CO_2 \rightarrow CO + O \qquad (4.3)$$

Energy profiles for the direct mechanism of CO_2 dissociation on Co(111) and FeCo(111) surfaces are shown in Figure 32. On the Co(111) surface, this mechanism proceeded with an activation energy of 61 kJ.mol^{-1} and a reaction energy of -77 kJ.mol^{-1}. On the FeCo(111) surface, the activation energy decreased to 17 kJ.mol^{-1}, while the exothermicity of the reaction increased to -154 kJ.mol^{-1}. These results demonstrated that Fe-doping on Co(111) surface promoted the dissociation of CO_2 via the direct mechanism.

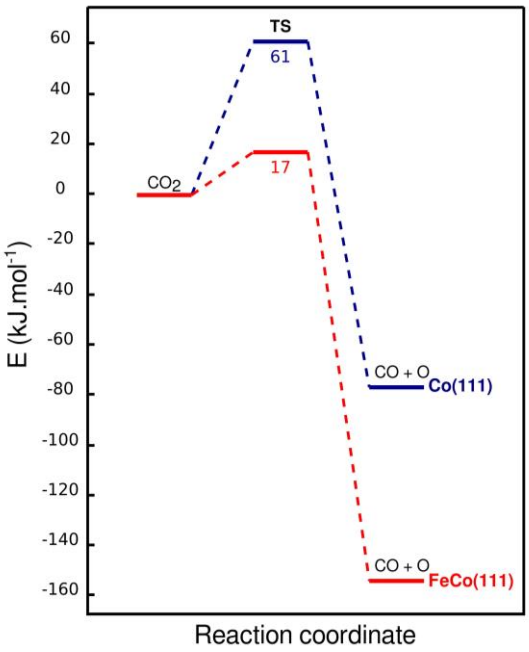

Figure 32. Potential energy diagram for CO_2 dissociation via the direct mechanism on Co(111) and FeCo(111) surfaces.

The IS, TS, and FS geometries of the direct mechanism of CO_2 dissociation on Co(111) and FeCo(111) are provided in Figure 33.

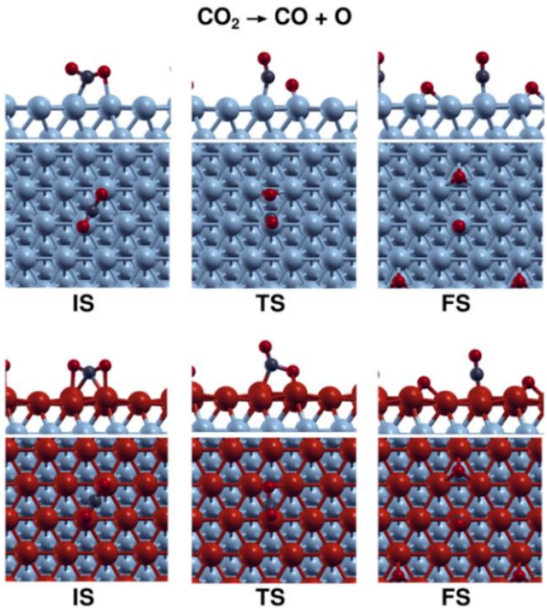

Figure 33. IS, TS and FS for the CO_2 dissociation via direct mechanism on Co(111) and FeCo(111) surfaces.

4.3.2.2. CO_2 Dissociation via H-assisted Mechanism

H-assisted mechanism involves carboxylate mechanism and formate mechanism. These reaction mechanisms and corresponding results on those surfaces are provided below.

The reaction equations of carboxylate mechanism including COOH formation an its dissociation are provided in Equation 4.4 and 4.5, respectively.

$$CO_2 + H \rightarrow COOH \quad (4.4)$$

$$COOH \rightarrow CO + OH \quad (4.5)$$

Figure 34 shows that the activation energy for COOH formation increased from 94 kJ/mol for Co(111) to 149 kJ/mol for FeCo(111). The increase in the activation energy was also consistent with the change in reaction energy from -18 kJ/mol (exothermic) for Co(111) to 41 kJ/mol (endothermic) for FeCo(111). These results suggest that the rate of the carboxylate mechanism on the FeCo(111) surface is expected to be significantly lower

than the redox mechanism. Furthermore, the implementation of the redox mechanism is expected to be more prominent on the FeCo(111) surface when compared to the Co(111) surface. Due to the high activation energy for COOH formation on the bimetallic surface, this elementary reaction is not expected to take place within the temperature range of 210-240°C which is typically used for CO_2 hydrogenation on cobalt catalysts.

The COOH intermediate is expected to dissociate into CO and OH molecules on the catalyst surface. On the Co(111) surface, this mechanism proceeded with an activation energy of 53 kJ.mol^{-1} and a reaction energy -112 kJ.mol^{-1}. On the FeCo(111) surface, the activation energy increased to 74 kJ.mol^{-1}, while the exothermicity of the reaction increased to -142 kJ.mol^{-1}. Thus, with the addition of iron on cobalt catalyst, the activation energy increased, and the reaction became more exothermic.

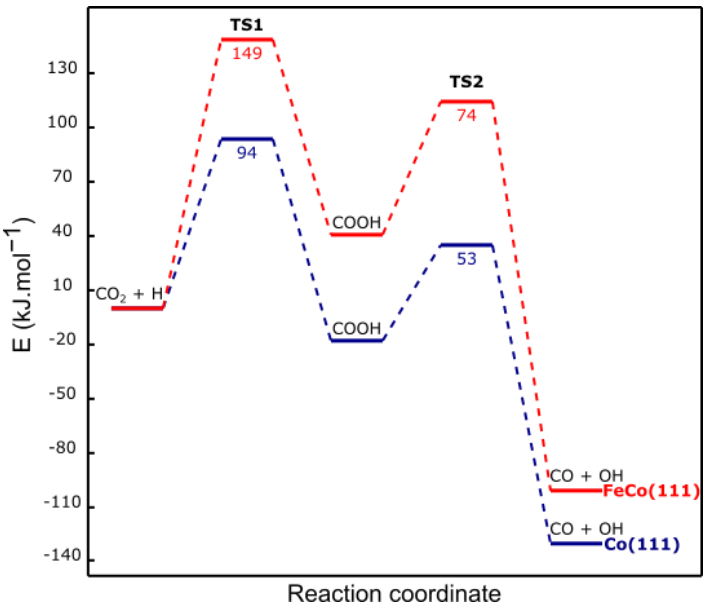

Figure 34. Potential energy diagram for CO_2 dissociation via carboxylate mechanism on Co(111) and FeCo(111) surfaces.

The corresponding IS, TS, and FS geometries of CO_2 dissociation via carboxylate mechanism and the dissociation of COOH into CO and OH on Co(111) and FeCo(111) surfaces are provided in Figure 35.

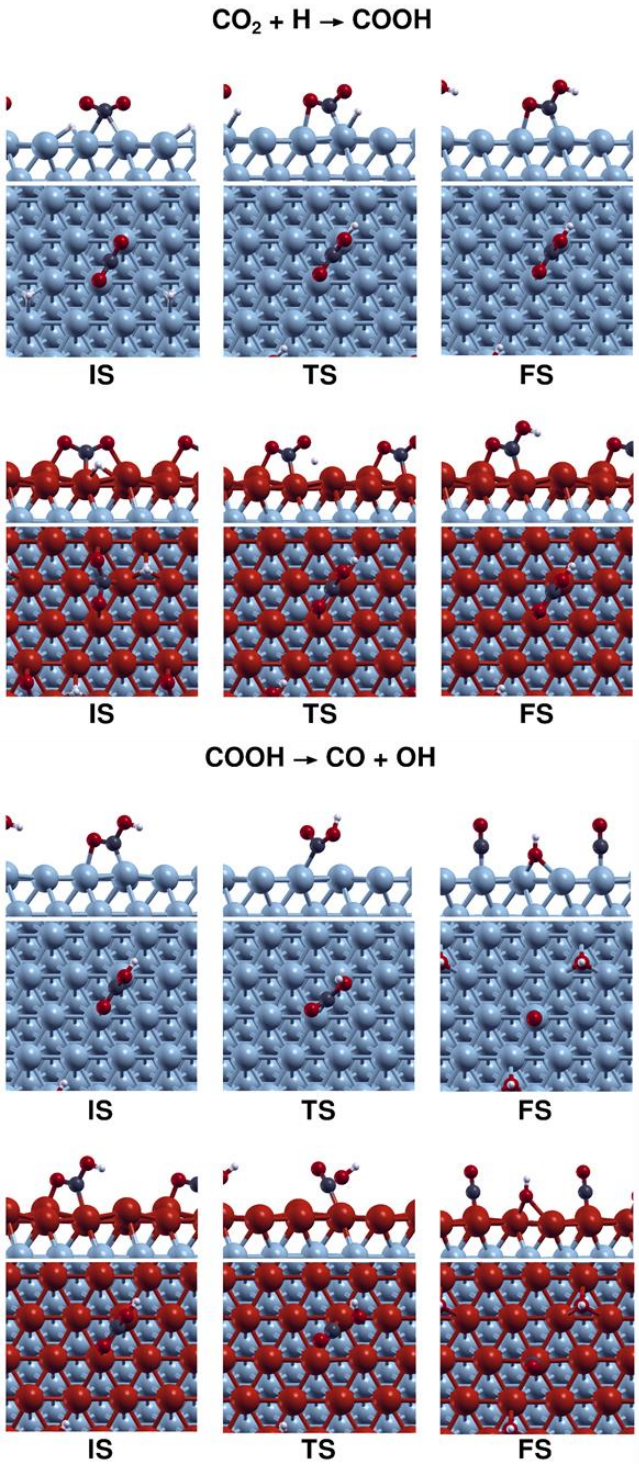

Figure 35. IS, TS and FS for the CO_2 dissociation via carboxylate mechanism on Co(111) and FeCo(111) surfaces.

Within the format mechanism including HCOO formation and its dissociation to HCO and O, the CO_2 dissociation takes place as described in Equation 4.6 and 4.7.

$$CO_2 + H \rightarrow HCOO \quad (4.6)$$

$$HCOO \rightarrow HCO + O \quad (4.7)$$

Figure 36 shows that the activation energy for HCOO formation decreased from 71 kJ.mol^{-1} for Co(111) to 51 kJ.mol^{-1} for FeCo(111), while increasing the reaction energy from -74 kJ.mol^{-1} to -55 kJ.mol^{-1}. These results indicate that the rate of the formate mechanism on the FeCo(111) surface will be significantly increased than the redox mechanism.

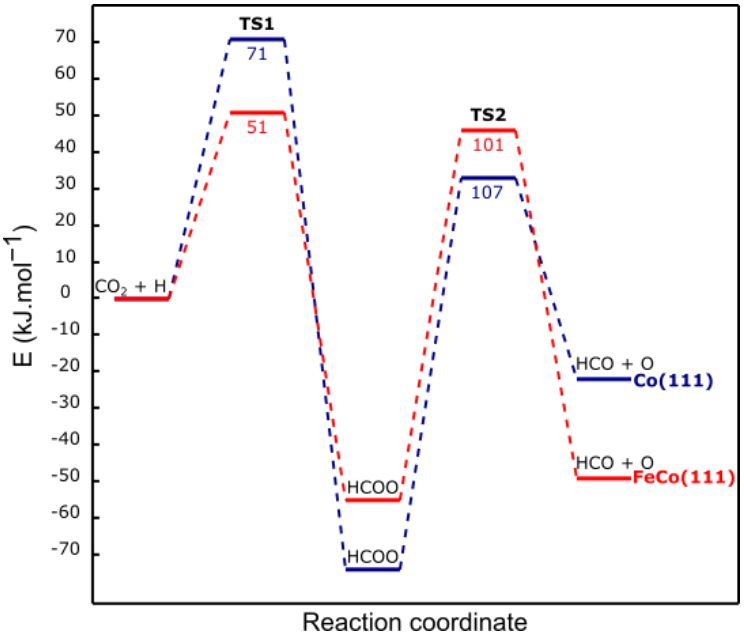

Figure 36. Potential energy diagram for CO_2 dissociation via formate mechanism on Co(111) and FeCo(111) surfaces.

The HCOO intermediate is expected to dissociate into HCO molecule and atomic O on the catalyst surface. On the Co(111) surface, this mechanism proceeded with an activation energy of 107 kJ.mol^{-1} and a reaction energy 52 kJ.mol^{-1}. On the FeCo(111) surface, the activation energy increased to 101 kJ.mol^{-1}, while the exothermicity of the reaction increased to 6 kJ.mol^{-1}. It demonstrated that the Fe-doping on cobalt resulted in a slight reduction in the activation energy of this reaction, making the reaction more

exothermic with the addition of iron on cobalt catalyst. This results indicate that formate mechanism is expected to be kinetically less favourable compared to the redox mechanism on both the FeCo(111) and Co(111) surfaces.

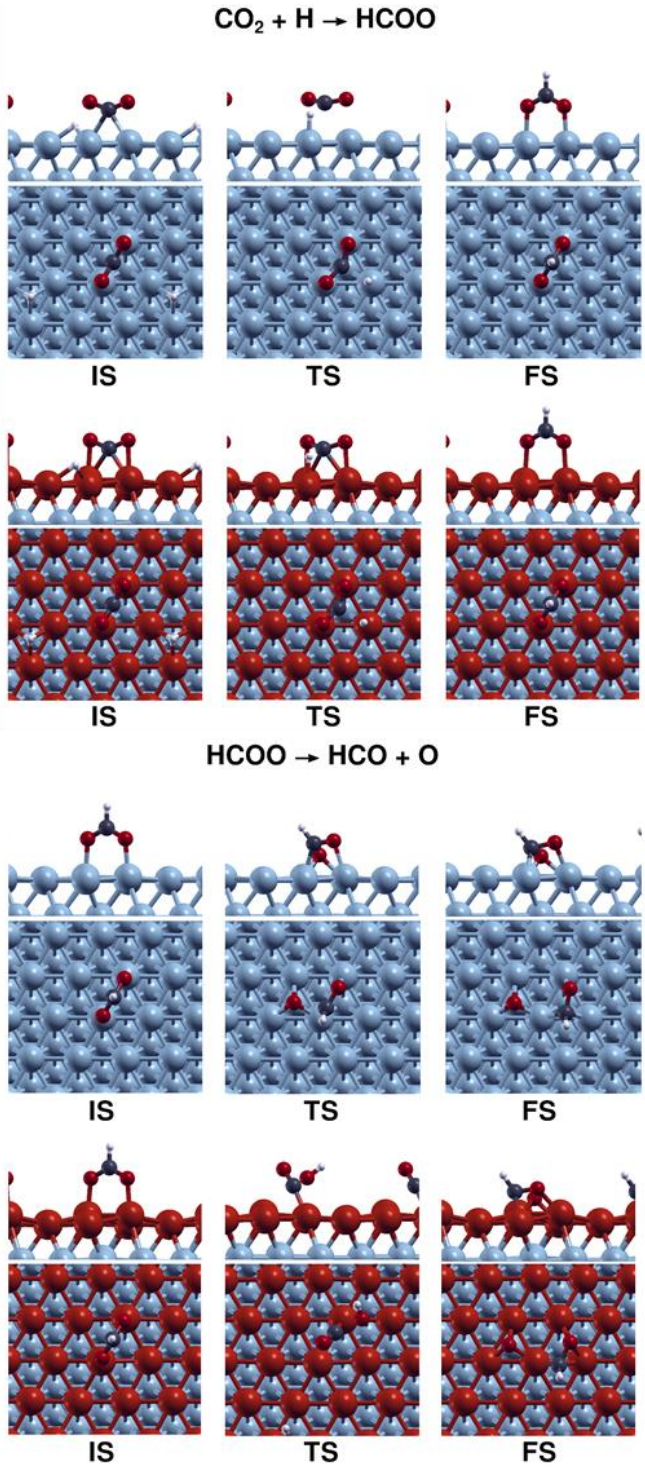

Figure 37. IS, TS and FS for the CO_2 dissociation via formate mechanism on Co(111) and FeCo(111) surfaces.

The corresponding IS, TS, and FS geometries of CO_2 dissociation via formate mechanism and the dissociation of HCOO into HCO and O on Co(111) and FeCo(111) surfaces are provided in Figure 37. It demonstrates that adsorbed CO_2 on FeCo(111) surface was located closer to the catalyst surface than that on Co(111) surface, leading to reduced activation energy for both redox and formate mechanisms.

As given in this section, three different reaction pathways for carbon dioxide dissociation were investigated and their reaction and activation energies were calculated on both pure and iron doped cobalt (111) surfaces. To determine which reaction pathway is more kinetically favorable, Figure 38 provides a comparative analysis of the reaction pathways and their activation energies comparatively on two distinct surfaces. As can be seen in the same figure, the direct mechanism for CO_2 dissociation was found to be more kinetically favorable on both Co(111) and Fe Co(111) surfaces when compared to the carboxylate and formate mechanisms. In the context of the carboxylate and formate mechanisms, the activation energy for the carboxylate mechanism increased with the addition of iron to the cobalt surface, while the activation energy for formate mechanism decreased. In line with a computational study that employed the Co(0001) surface as a model in the DRM [81], it is anticipated that the formate mechanism is expected to occur on Co(111) surface due to its manageable energy requirement and the high hydrogen coverage on the surface. The formate mechanism can also be preferred on the FeCo(111) surface due to its reasonable activation energy on this surface. However, it is important to note that the CO_2 dissociation is expected to be perform dominantly via redox mechanism on bimetallic surface due to an increase in the energy difference between the formate and redox mechanisms on Co(111) and FeCo(111) surfaces from 10 $kJ.mol^{-1}$ to 34 $kJ.mol^{-1}$.

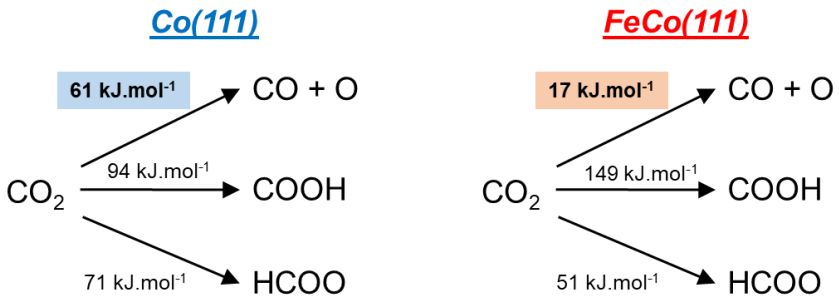

Figure 38. Calculated activation energies for reaction pathways of CO_2 dissociation on two surfaces.

4.3.3. CO Dissociation

CO dissociation on the catalyst surface occurs through two pathways, namely direct and H-assisted mechanisms. The reaction mechanisms and corresponding results for these two mechanisms on both surfaces are provided below.

4.3.3.1. CO Dissociation via Direct Mechanism

The direct mechanism of CO dissociation takes place as described in Equation 4.8. Carbon monoxide should be decomposed into both atomic C and O in this pathway.

$$CO \rightarrow C + O \tag{4.8}$$

Energy profiles for CO dissociation on the Co(111) vs FeCo(111) is shown in Figure 39. As seen in Figure 39, the direct dissociation of CO on the FeCo(111) surface was more exothermic than on the Co(111) surface, with a significant decrease in the activation energy from 267 kJ/mol to 173 kJ/mol. Due to an increase in the atomic C and O adsorption energies, it is an expected result that CO dissociation became more exothermic. These results indicate that this reaction is not feasible under low temperature conditions for CO_2 hydrogenation on both Co(111) and FeCo(111) surfaces. Furthermore, the corresponding IS, TS, and FS geometries of direct CO dissociation on Co(111) and FeCo(111) surfaces are provided in Figure 40.

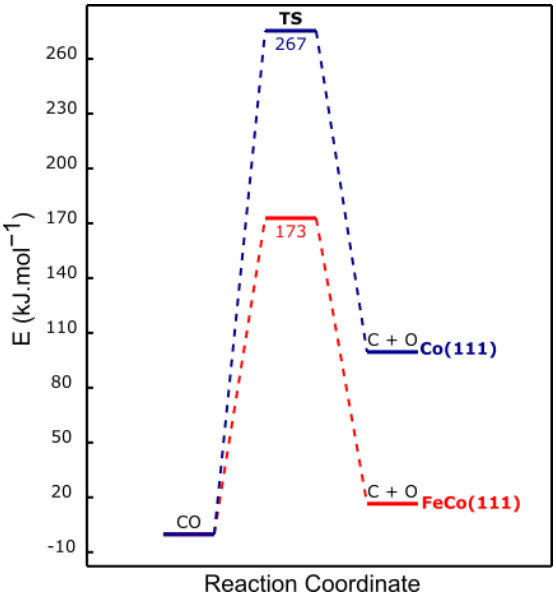

Figure 39. Potential energy diagram for CO dissociation via direct mechanism on Co(111) and FeCo(111) surfaces.

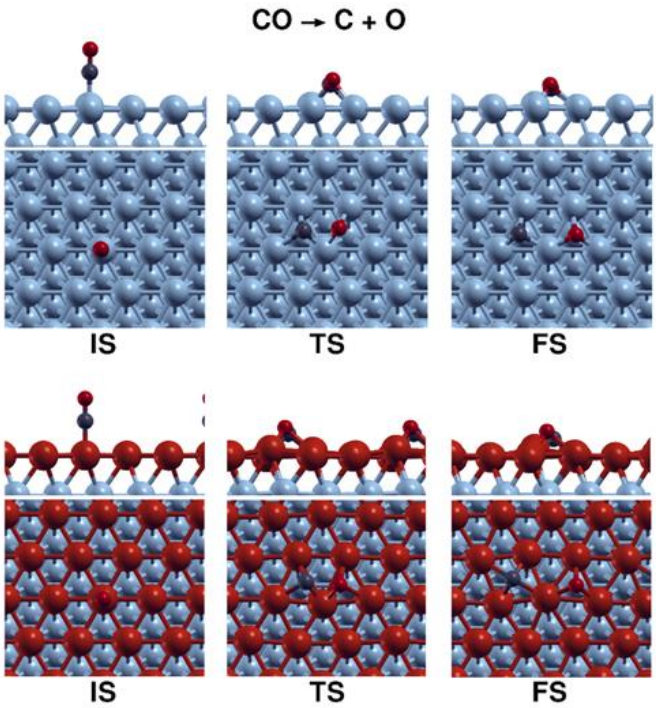

Figure 40. IS, TS and FS for the CO dissociation via direct mechanism on Co(111) and FeCo(111) surfaces.

4.3.3.2. CO Dissociation via H-assisted Mechanism

The H-assisted dissociation of CO takes place as described in Equation 4.9 and 4.10. The dissociation of HCO would produce CH and O intermediates. The resulting CH intermediate could react with H to form CH_2 and the formed atomic O reacts with atomic H to form OH intermediate.

$$CO + H \rightarrow HCO \quad (4.9)$$

$$HCO \rightarrow CH + O \quad (4.10)$$

The activation energy for HCO formation through the hydrogenation of CO, via the H-assisted pathway, on the FeCo(111) was found to be slightly higher (3 $kJ.mol^{-1}$) than that of the Co(111) surface. The reaction energies for the formation of HCO were calculated on the Co(111) and FeCo(111) surfaces, resulting in values of 96 $kJ.mol^{-1}$ and 97 $kJ.mol^{-1}$, respectively. This result indicates that the addition of Fe resulted in a slight decrease in the rate of H-assisted CO dissociation.

Figure 41 shows that HCO formation on the FeCo(111) surface can occur with a slight increase in activation energy compared to the Co(111) surface. Fe-doping on Co(111) resulted in a 30 kJ/mol decrease in the activation energy for the dissociation of the HCO intermediate. These results show that the CO dissociation on FeCo(111) will occur by the H-assisted mechanism. Moreover, the relevant IS, TS, and FS geometries for the CO dissociation via H-assisted mechanism on Co(111) and FeCo(111) surfaces are presented in Figure 42.

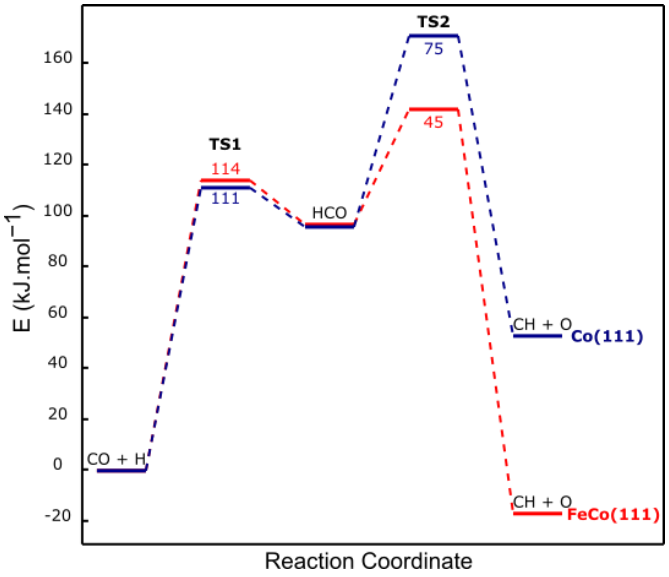

Figure 41. Potential energy diagram for CO_2 dissociation via H-assisted mechanism on Co(111) and FeCo(111) surfaces.

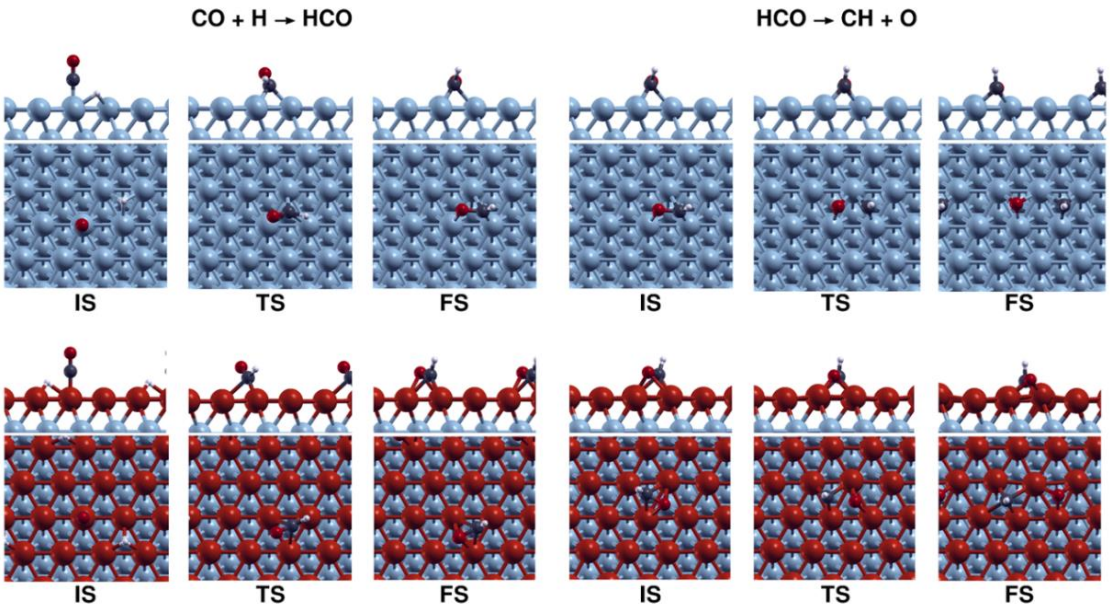

Figure 42. IS, TS and FS for the CO dissociation via H-assisted mechanism on Co(111) and FeCo(111) surfaces.

To determine which reaction pathway is more kinetically favorable among two reaction mechanisms for CO dissociation, a comparative analysis of the reaction pathways and their activation energies on Co(111) and FeCo(111) surfaces is summarized in Figure 43. Due to the relatively high energy of direct CO dissociation, the CO

dissociation via the H-assisted pathway was found to be more kinetically favorable on both Co(111) and Fe Co(111) surfaces compared to the direct dissociation mechanism.

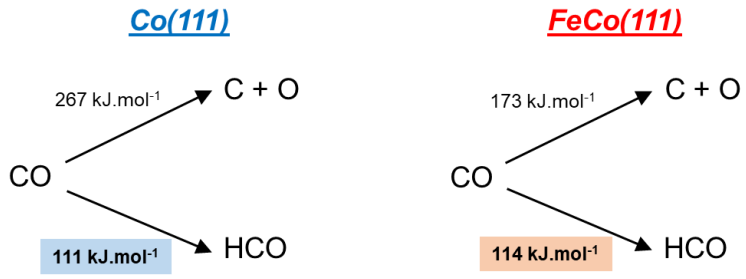

Figure 43. Calculated activation energies for reaction pathways of CO dissociation on two surfaces.

In terms of the CO_2 and CO hydrogenation, Fe-doping resulted in the slowdown of the hydrogenation of both CO2 and CO molecules. Furthermore, as CO formation via CO_2 dissociation was promoted by bimetallic surface, the surface CO coverage is expected to highly dominant on the FeCo(111) than on Co(111) surface. Due to the higher activation energy for HCO formation and the lower activation energy of HCO dissociation into CH and O, the surface HCO coverage is expected to be decrease on the bimetallic surface as a consequence of the Fe-doping on cobalt catalyst.

Overall, these results demonstrate that surface modification via Fe-doping on Co(111) promoted the surface CO coverage and kinetics of CO_2 and CO dissociation, while the surface H coverage was relatively low. Furthermore, Fe-doping resulted in an increase in the activation energy for rate-limiting step, HCO formation, leading to a decrease in the overall activity for CO_2 hydrogenation. Moreover, the comparison between CO adsortion energy and the activation energy for its dissociation via H-assisted mechanism indicates that the Fe-doping inhibited the desorption of CO from the surface. For this reason, it is unlikely that CO can be produced as product on the FeCo(111) surface. This suggests that the FeCo(111) surface may not be the primary contributor to the observed CO selectivity in experimental studies [51].

4.3.4. CH_4 Formation

Methane would be formed through the sequential hydrogenation of atomic C which could be formed via dissociation of CO on the catalyst surface. Then the C atom can undergo sequential hydrogenation to form methane. In these hydrogenation reactions, CH, CH_2, CH_3, and CH_4 species are formed via Equation 4.11, 4.12, 4.13 and 4.14, respectively. The reaction mechanisms and corresponding results on both surfaces are provided below. The pathways for formation of CH_4 on Co(111) and FeCo(111) were modeled as well as the geometries of the IS, TS, and FS are shown in Figure 45.

$$C + H \rightarrow CH \quad (4.11)$$

$$CH + H \rightarrow CH_2 \quad (4.12)$$

$$CH_2 + H \rightarrow CH_3 \quad (4.13)$$

$$CH_3 + H \rightarrow CH_4 \quad (4.14)$$

As can be seen in Figure 44, the formation of CH intermediate on the Co(111) surface proceeded with an activation energy of 68 kJ.mol^{-1}, and a reaction energy of -49 kJ.mol^{-1}. On the FeCo(111) surface, this reaction proceeded with an activation energy of 86 kJ.mol^{-1}, and a reaction energy of -11 kJ.mol^{-1}. The activation energy for the formation of CH intermediate on Co(111) was found to be 18 kJ.mol^{-1} lower than that on Fe-doped Co(111), suggesting that the incorporation of Fe into the Co made the formation of CH intermediate more challenging. In the context of the hydrogenation of CH, the activation energy and reaction energy of CH_2 formation on Co(111) were determined to be 48 and 12 kJ.mol^{-1}, respectively, whereas on the FeCo(111) surface, these values were 67 and 48 kJ.mol^{-1}, respectively. The activation energy in the second step (Equation 4.12) of CH_4 formation was increased by 19 kJ.mol^{-1} on FeCo(111) compared to that in corresponding step on pure Co(111). The formation of CH_3 on the Co(111) surface proceeded with an activation energy of 45 kJ.mol^{-1} and a reaction energy of -39 kJ.mol^{-1}, whereas on the FeCo(111) surface, these values were found as 65 kJ.mol^{-1} and 2 kJ.mol^{-1}, respectively. The activation energies for both CH_3 and CH_4 formation were increased by 20 kJ.mol^{-1}

on FeCo(111) compared to that in corresponding steps on pure Co(111). In the context of the formation of CH_4, the reaction on Co(111) surface proceeded with an activation energy of 90 kJ.mol^{-1} and a reaction energy of -52 kJ.mol^{-1}, whereas on the FeCo(111) surface, these values were found as 110 kJ.mol^{-1} and 0 kJ.mol^{-1}, respectively. Based on these results, the change in the activation energies of methane formation on those surfaces was in the range of 18-20 kJ.mol^{-1}. Consequently, the activation energies for CH_x (x=1-4) formation follow the order of CH_4 > CH > CH_2 > CH_3 on both Co(111) and FeCo(111) surfaces. The corresponding reaction geometries including IS, TS and FS of these elementary reactions are given in Figure 45.

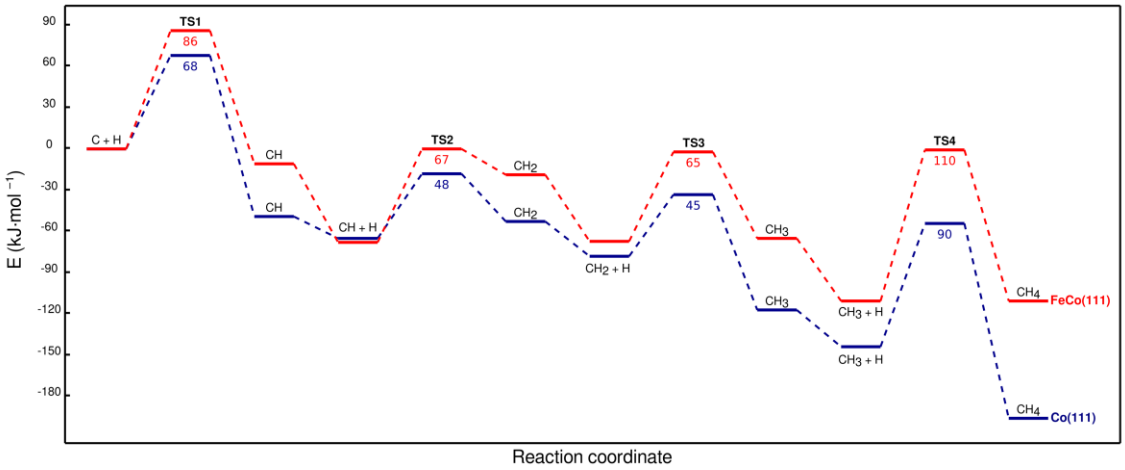

Figure 44. Potential energy diagram for CH_4 formation on Co(111) and FeCo(111) surfaces.

These results indicate that hydrogenation of C and CH_x species are slowed down by the Fe-doping on cobalt catalyst. Consequently, Fe-doping resulted in a decrease in the hydrogenation ability of the catalyst surface. The activation energy for rate-limiting step in methane formation, which is the CH_3 hydrogenation, was feasible on both pure and Fe-doped cobalt surfaces. This led to the production of methane as C_1 product on the FeCo(111) surface. However, the presence of iron atoms on the cobalt surface resulted in a reduction in the formation of methane. As consistent with the results of this study, an experimental study conducted by Gnanamani et al. demonstrated that the addition of iron on cobalt led to a reduction in methane selectivity and H_2 consumption [51].

In terms of the removal of atomic carbon from the surface, which is the important issue for the coke formation, Fe-doping resulted in a decrease in the rate of carbon build-up on the surface, due to an increase in the activation energy for the rate-limiting step. Based on the results of this study, atomic C on the surface can be removal from the surface via the formation of methane. Since coke formation on the surface involves a complex mechanism and is significantly influenced by temperature and structure, our findings do not precisely indicate the effect of Fe on coke formation. Further reasearch is needed to gain a better understanding of coke formation using modeling of surface and subsurface reactions for the formation of C-C bonds using DFT calculation and microkinetic modeling.

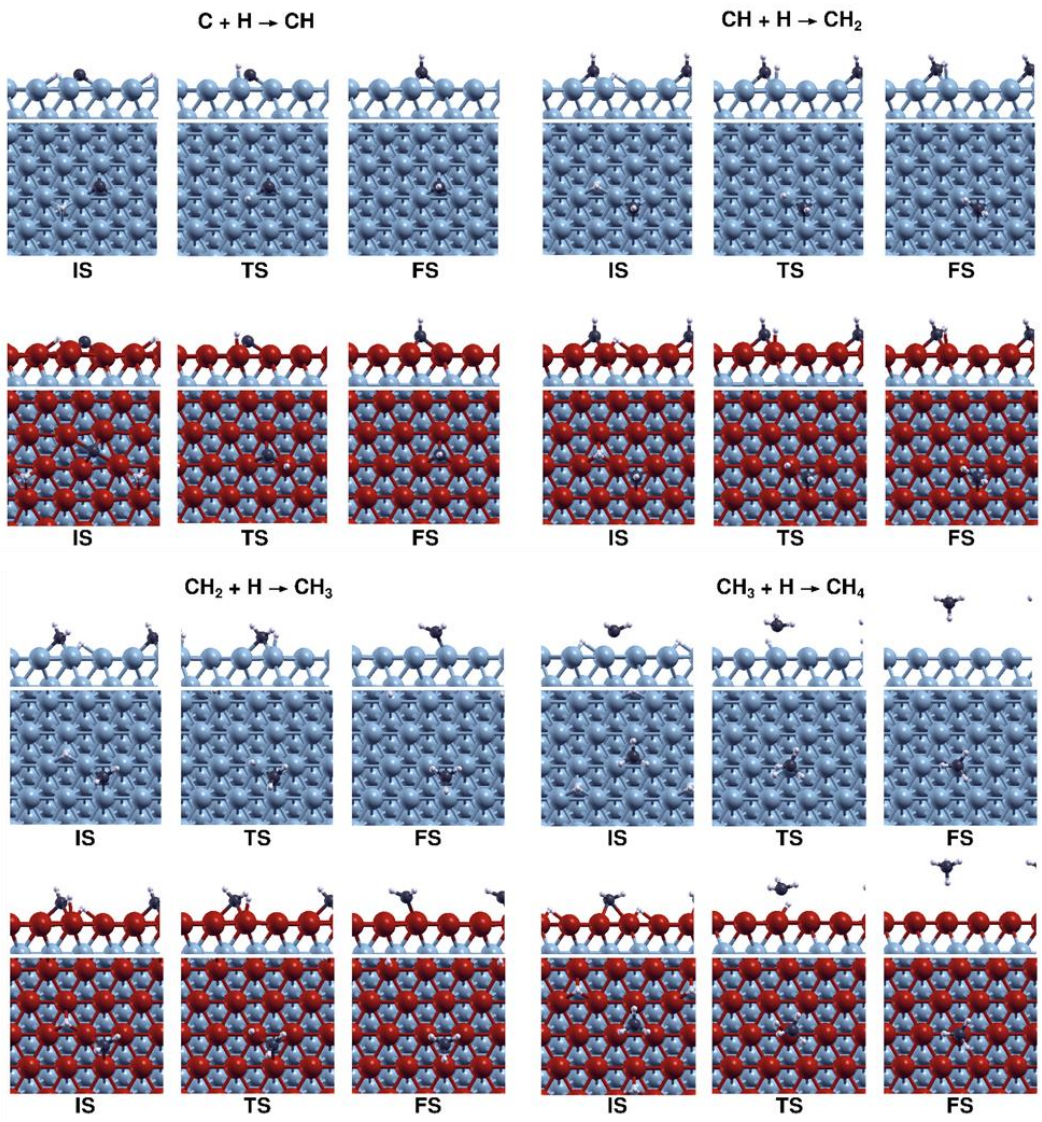

Figure 45. IS, TS and FS for the CH_4 formation on Co(111) and FeCo(111) surfaces.

4.3.5. CH_3OH Formation

Methanol is produced through the sequential hydrogenation of HCO, which could be formed through various pathways including the dissociation of CO via H-assisted path to form H_2CO, H_3CO, or H_3COH intermediates or the oxygenation of CH_2 and CH_3, and coupling of CH_3 and OH to form H_2CO, H_3CO, and H_3COH intermediates, respectively. The hydrogenation of HCO intermediate leads to the formation of H_2CO intermediate. In the subsequent reaction (Equation 4.18), H_2CO reacts with H to form H_3CO intermediate. Finally, H_3CO intermediate is hydrogenated to form H_3COH intermediate. The reaction mechanisms and corresponding results on both surfaces are provided below.

$$HCO + H \rightarrow H_2CO \quad (4.15)$$

$$CH_2 + O \rightarrow H_2CO \quad (4.16)$$

$$H_2CO \rightarrow CH_2 + O \quad (4.17)$$

$$H_2CO + H \rightarrow H_3CO \quad (4.18)$$

$$CH_3 + O \rightarrow H_3CO \quad (4.19)$$

$$H_3CO + H \rightarrow H_3COH \quad (4.20)$$

$$CH_3 + OH \rightarrow H_3COH \quad (4.21)$$

H_2CO intermediate which is required to produce methanol could be obtained from the reaction of CH_2 and O (Equation 4.16). Both CH_2 and O species were formed on the catalyst surface through the dissociation of CO and CO_2, as well as CH_x hydrogenation. In addition, Figure 47 shows that the optimized reaction geometries for the formation of H_2CO intermediate is formed via hydrogenation of HCO intermediate.

As can be observed in the PED shown in Figure 46, the activation energy for H_2CO formation through the hydrogenation of HCO on FeCo(111) was significantly higher (28 $kJ.mol^{-1}$) compared to that on the Co(111) surface. In the context of the formation of H_3CO intermediate, this reaction proceeded on the FeCo(111) surface with an activation energy of 51 $kJ.mol^{-1}$ and a reaction energy of -50 $kJ.mol^{-1}$. Conversely, on the Co(111) surface, these values were determined as 42 $kJ.mol^{-1}$ and -83 $kJ.mol^{-1}$, respectively. The activation energy of 177 kJ/mol on the FeCo(111) surface slowed down the further

hydrogenation of H_3CO to form H_3COH, with a reaction energy of 94 kJ.mol^{-1}. In contrast, this reaction occured on the Co(111) surface with a lower activation energy of 160 kJ.mol^{-1} and a reaction energy of 56 kJ.mol^{-1}. These findings suggest that methanol formation is not favorable on both Co(111) and FeCo(111) surfaces.

Although the activation energy for H_3CO formation via H_2CO hydrogenation is feasible, methanol cannot be produced due to its high activation energies on both Co(111) and FeCo(111) surfaces. These findings are consistent with a DFT study related on methanol steam reforming on Co(0001) surface [83] and a experimental study on CO_2 hydrogenation on cobalt catalyst [25].

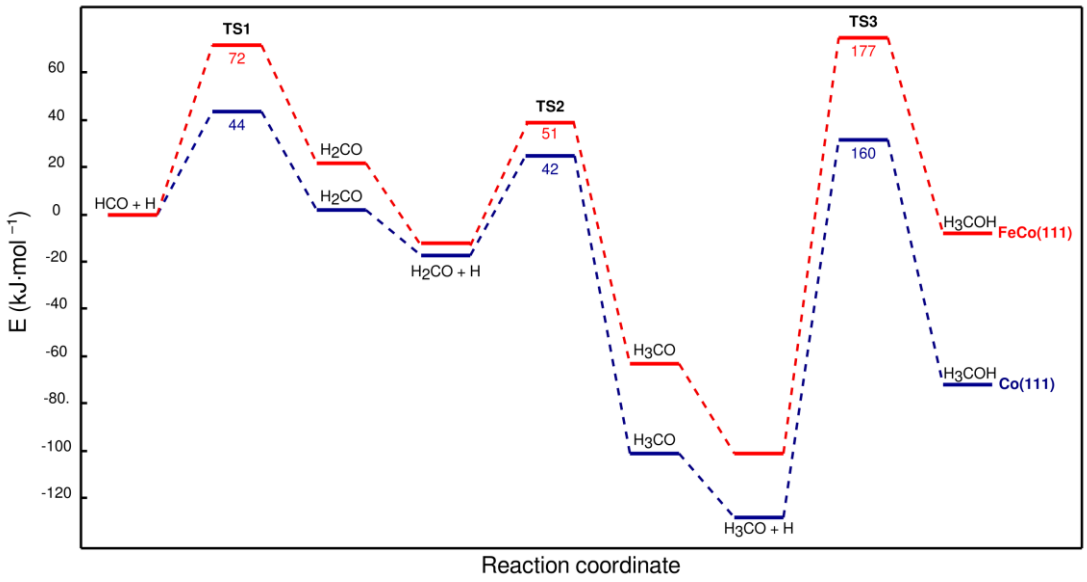

Figure 46. Potential energy diagram for H_3COH formation on Co(111) and FeCo(111) surfaces.

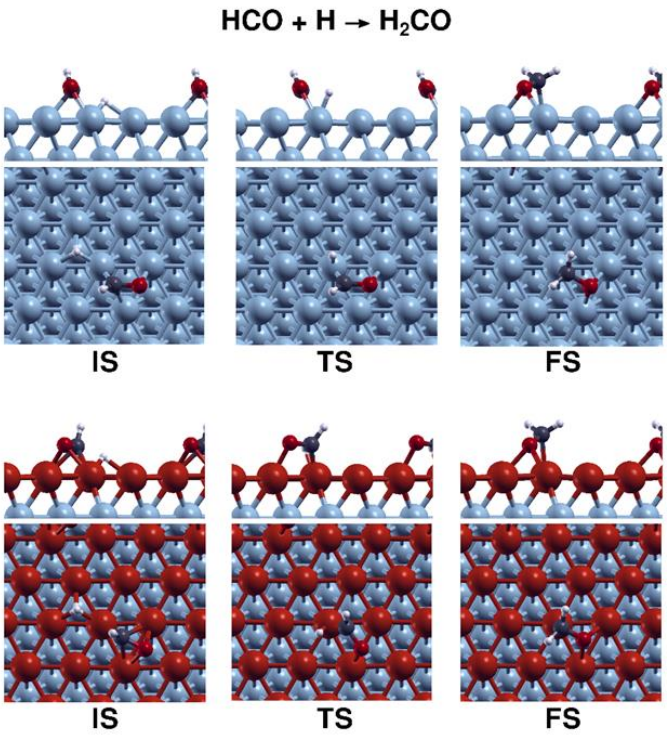

Figure 47. IS, TS and FS for the H_2CO formation on Co(111) and FeCo(111) surfaces.

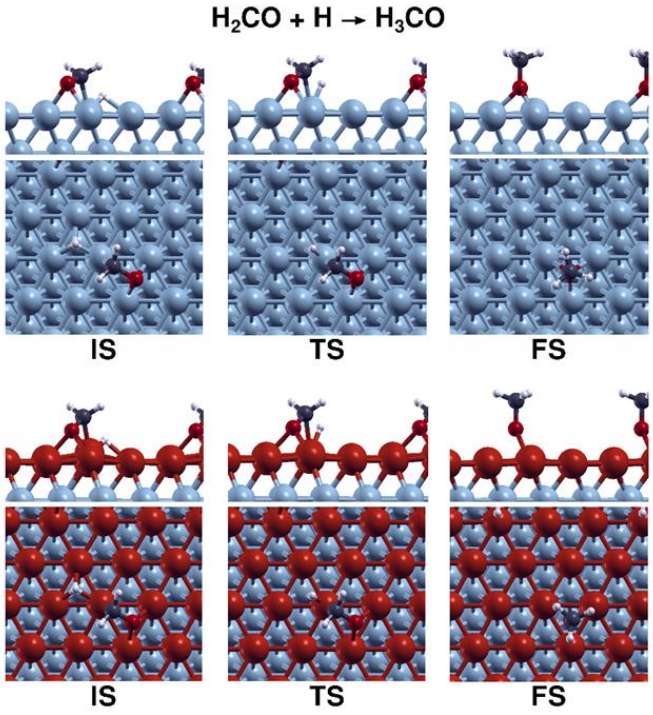

Figure 48. IS, TS and FS for the H_3CO formation on Co(111) and FeCo(111) surfaces.

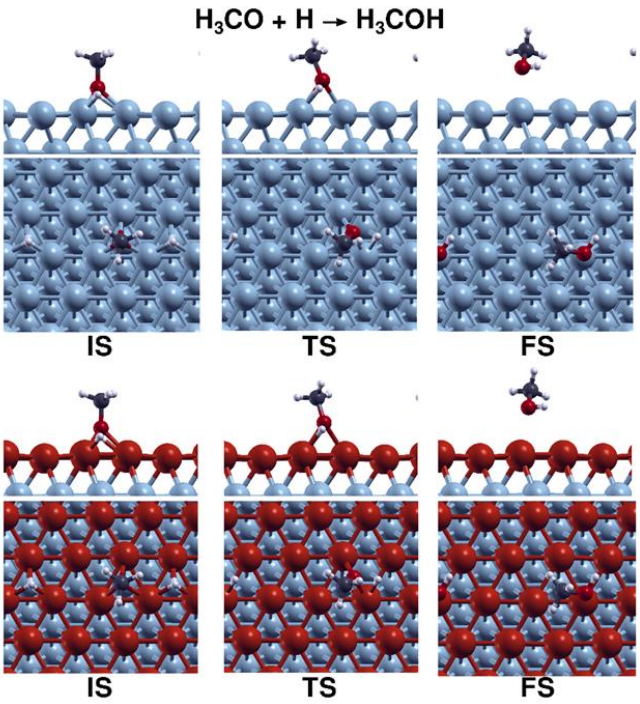

Figure 49. IS, TS and FS for the H_3COH formation on Co(111) and FeCo(111) surfaces.

In the context of the oxidation of CH_x species, the H_2CO formation through the coupling of CH_2 and O on Co(111) and FeCo(111) surfaces was associated with notably higher activation energy of 124 kJ.mol^{-1} and 150 kJ.mol^{-1}, respectively. It demonstrated that the dissociation of H_2CO into CH_2 and O was found to be slightly promoted by the FeCo(111) surface compared to the Co(111) surface.

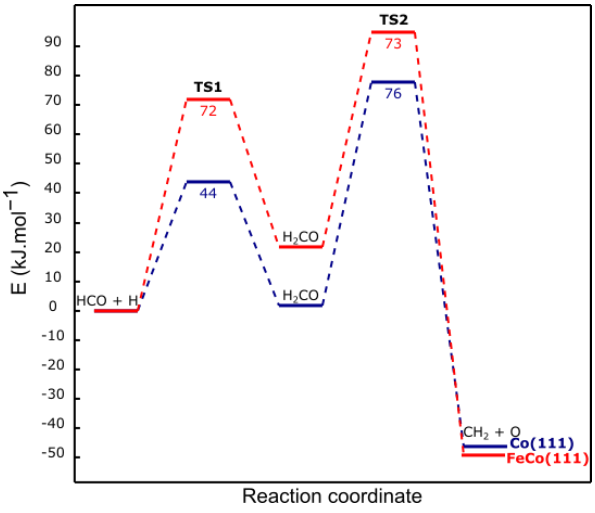

Figure 50. Potential energy diagram for formation and dissociation of H_2CO intermediate on Co(111) and FeCo(111) surfaces.

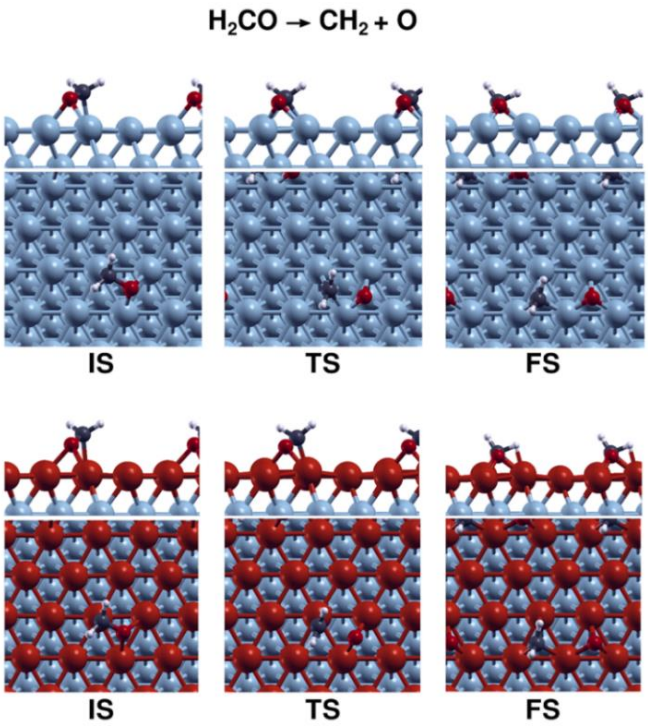

Figure 51. IS, TS and FS for the H_2CO dissociation on Co(111) and FeCo(111) surfaces.

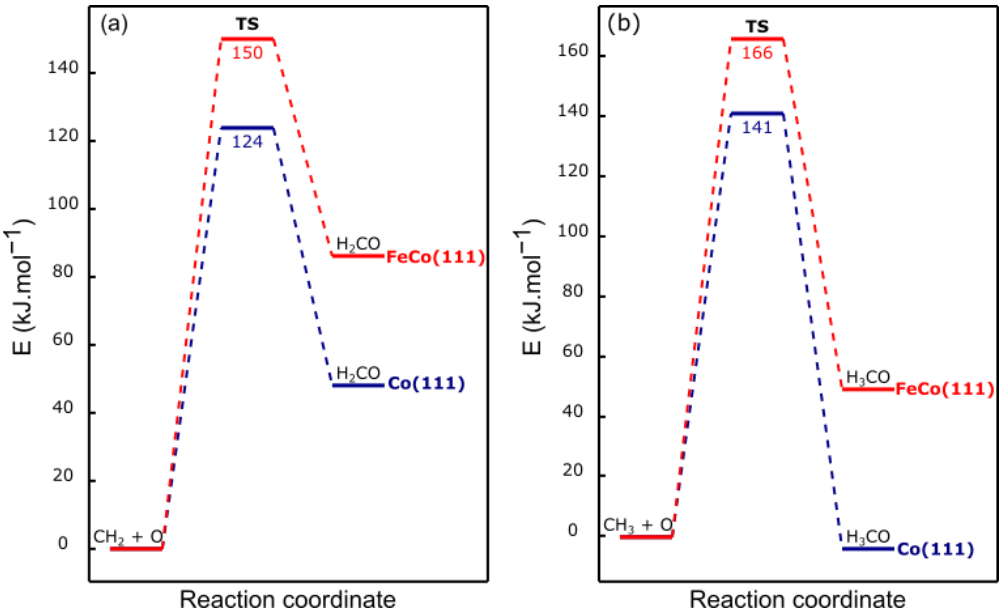

Figure 52. Potential energy diagram for H_2CO (a) and H_3CO (b) formation via CH_x oxidation on Co(111) and FeCo(111) surfaces.

The formation of H_3CO intermediate through the coupling of CH_3 and O on FeCo(111) surface proceeded with an activation energy of 166 $kJ.mol^{-1}$ and a reaction

energy 49 kJ.mol^{-1}, whereas on the Co(111) surace, these values were found as 141 kJ.mol^{-1} and -4 kJ.mol^{-1}, respectively. Furthermore, the coupling of CH_3 and OH on those surfaces exhibited significantly high activation energies of 196 and 238 kJ.mol^{-1}, respectively. These results indicate that the formed CH_2 and CH_3 species do not readily react with O or OH species on pure Co and Fe- doped Co surfaces due to their impractical activation energies at low-temperature reaction conditions for CO_2 hydrogenation.

4.3.6. H_2O Formation

Water can be formed through the reaction of surface intermediates such as O, H, and OH as a by-product in hydrogenation of CO_2 or CO. In this study, the formation of water is investigated with two distinct pathways, specifically the hydrogenation of atomic oxygen and OH coupling mechanisms. The reaction mechanisms and corresponding results on both surfaces are provided below.

The pathways for formation of H_2O via hydrogenation of atomic O mechanism and OH coupling mechanism on Co(111) and FeCo(111) were modeled as well as the geometries of the initial state (IS), transition state (TS), and final state (FS) are shown in Figure 54 and 56, respectively.

4.3.6.1. H_2O Formation via Hydrogenation of Atomic Oxygen

The formation of water through the atomic O hydrogenation mechanism is shown in Equation 4.22 and 4.23.

$$O + H \rightarrow OH \quad (4.22)$$

$$OH + H \rightarrow H_2O \quad (4.23)$$

The formation of OH on the Co(111) surface proceeded with an activation energy of 124 kJ.mol^{-1} and a reaction energy of 6 kJ.mol^{-1}, whereas on the FeCo(111) surface, there values were found as 168 kJ.mol^{-1} and 50 kJ.mol^{-1}, respectively. The activation energy for OH formation was consistent with a study in the literature that found as the activation energy for OH formation on Co(0001) surface [85]. These findings indicate that OH formation on FeCo(111) was inhibited by its sizeable activation energy.

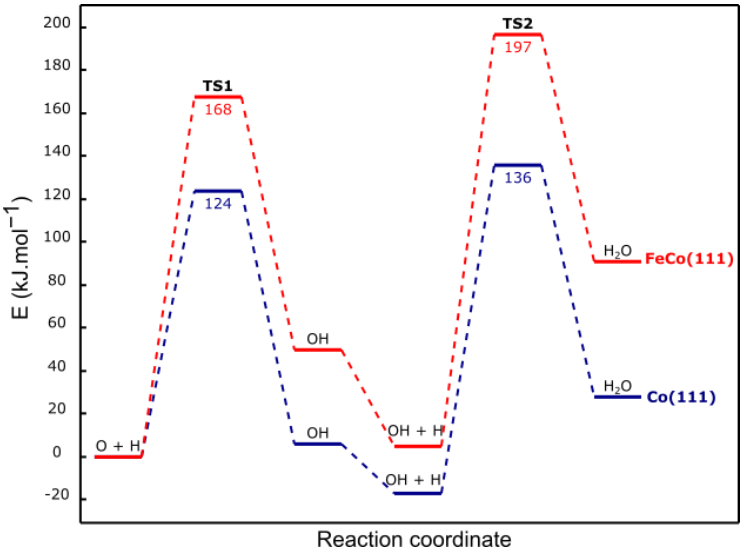

Figure 53. Potential energy diagram for H_2O formation via the hydrogenation of atomic O on Co(111) and FeCo(111) surfaces.

It is important to note that the surface oxygen cannot be removed as water from these surfaces. The inhibition of oxygen removal may lead to the accumulation of oxygen or the formation of oxygenated products. However, as discussed in the previous section, the formation of oxygenated compounds is hindered by both Co(111) and FeCo(111) surfaces.

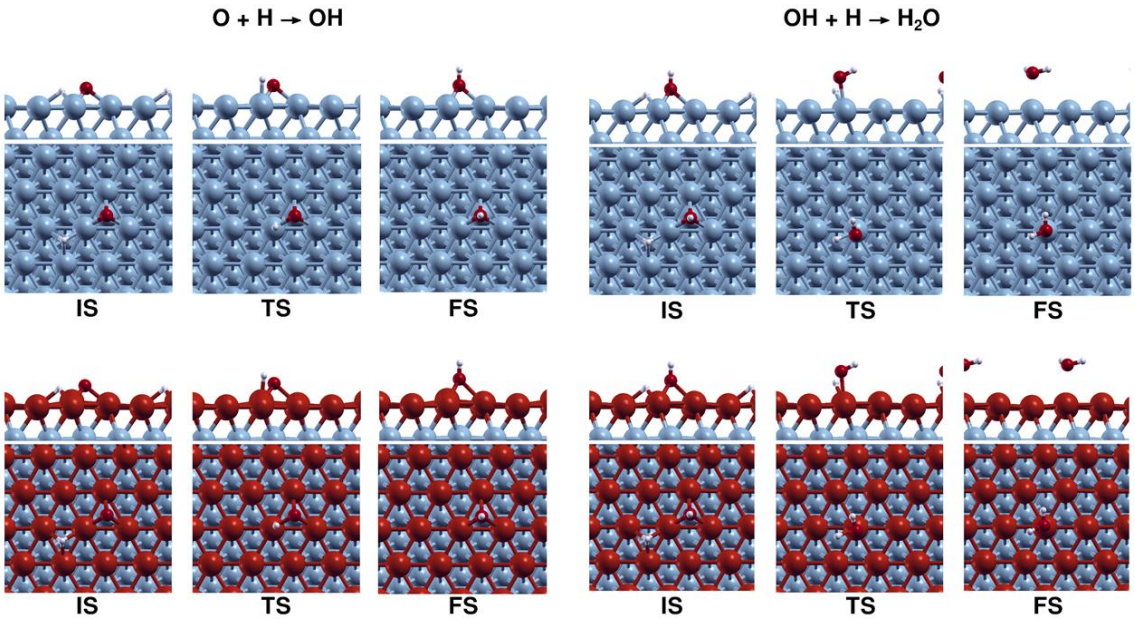

Figure 54. IS, TS and FS for the H_2O formation via hydrogenation of atomic oygen on Co(111) and FeCo(111) surfaces.

4.3.6.2. H_2O Formation via OH Coupling Mechanism

The formation of water by the OH coupling mechanism is shown in Equation 4.24.

$$OH + OH \rightarrow H_2O + O \qquad (4.24)$$

PED for OH coupling, as presented in Figure 55, demonstrates that the activation energy for OH coupling on FeCo(111) decreased by 8 kJ.mol^{-1} compared to the Co(111) surface, while the reaction energy became more endothermic by 4 kJ.mol^{-1}. Even though the activation energies for OH coupling on both Co(111) and FeCo(111) werw determined to be 40 kJ.mol^{-}1 and 48 kJ.mol^{-1}, respectively, which are feasible under low-temperature CO_2 hydrogenation conditions, this reaction was hindered due to the inhibition of OH formation. However, it is also reported that H_2O formation proceeded via OH coupling instead of OH hydrogenation on cobalt surface when OH groups are formed on the surface in the literature [85].

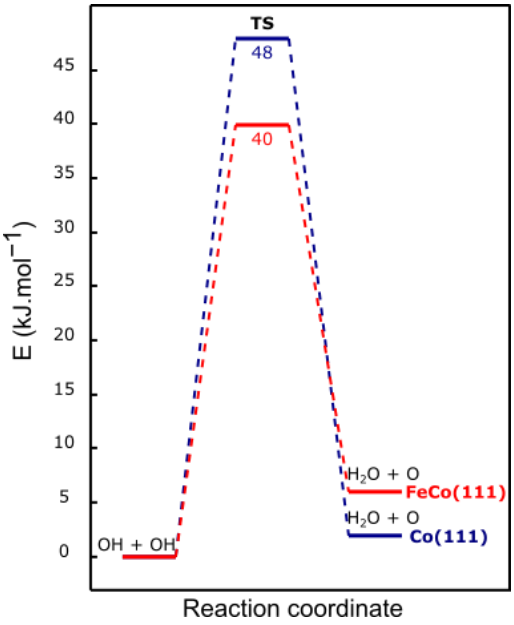

Figure 55. Potential energy diagram for formation H_2O via OH coupling on Co(111) and FeCo(111) surfaces.

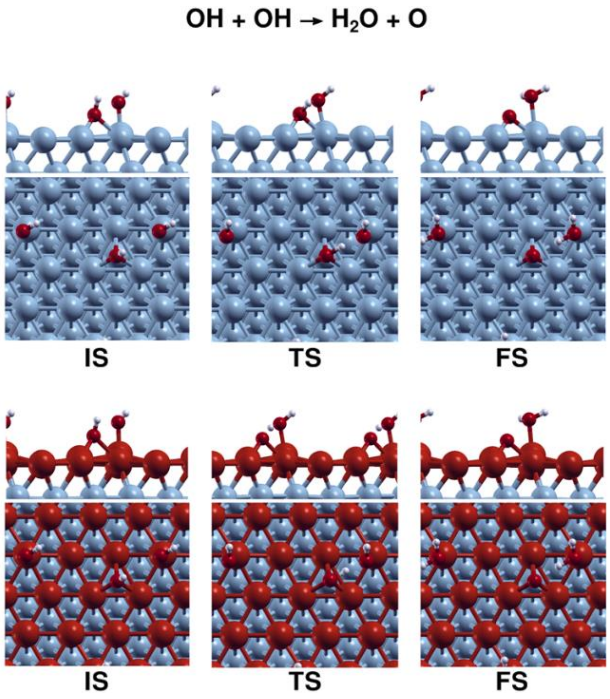

Figure 56. IS, TS and FS for the H_2O formation via OH coupling on Co(111) and FeCo(111) surfaces.

All elementary reactions investigated in this study are collected in Figure 57, along with the activation energies for Co(111) and FeCo(111) surfaces.

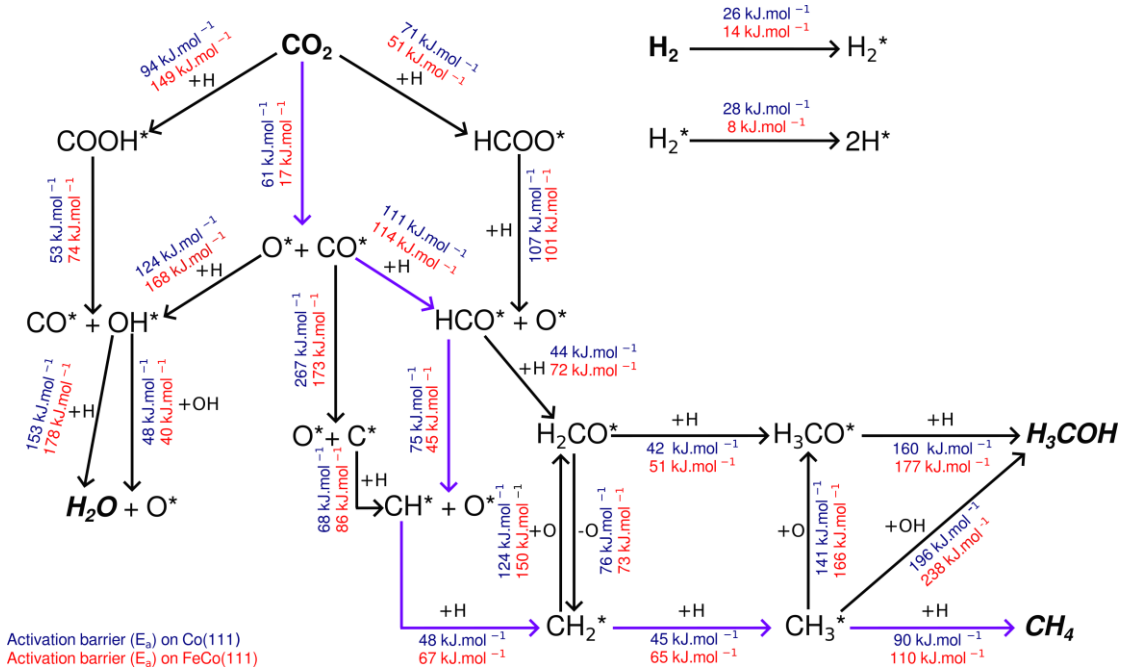

Figure 57. All the modeled reactions and their activation energies for both pure and Fe-doped Co(111) surfaces with emphasis on the dominant pathway illustrated by purple arrow.

Overall, the catalytic performance of the Fe-doped Co(111) surface has been examined in terms of the activity, selectivity and stability in this detail for the first time in the literature. Regarding the activity, bimetallic FeCo(111) surface exhibited lower overall catalytic activity compared to the monometallic Co(111) surface due to an increase in the activation energy of rate-limiting step. In terms of the selectivity, methane formation is expected to increase on the bimetallic surface among the C_1 products. However, due to the increase in the activation energy for methane formation of FeCo(111) and the lower surface H coverages compared to the monometallic Co(111) surface, an increase in the selectivity for unsaturated hydrocarbons are expected on the bimetallic FeCo(111) surface. Concerning the stability of the catalyst, the inhibition of the surface oxygen is expected to result in change in the catalyst.

4.4. Bader Charge Analysis

To unveil the electronic structure of the adsorbates and adorbents, the Bader charge analysis was carried out in this study. The formation of a bimetallic catalyst from two different metals changes the electronic properties of the catalyst surface. The change in the electronic properties of the surface affects the adsorption energies of the adsorbates, leading to a modification in the catalytic activity. The total Bader charges of adsorbates on Co(111) and FeCo(111) were collected in Table 4.

As can be seen in the Table 4, all intermediates are negatively charged, indicating that the adsorbed species withdraw electrons from the catalyst surface. These results on the Co(111) surface are in line with the findings of Jeske and Kizilkaya et al. [79], Santos-Carballal et al. [86] and Liu et al. [87] demonstrated that certain intermediates, such as adsorbed CO and H, withdraw the electron density from the pure Co(111) surface. As the catalyst surface was a Fe-doped Co surface, the addition of Fe resulted in additional electronic charge accumulation on all intermediates examined in this study, except H_3COH. It indicates that the addition of Fe increased the electron density of the adsorbates, signifying a transfer from the electrons of iron atoms to the adsorbates. The presence of iron on the cobalt surface resulted in the formation of distinct charges on the surface species. The Bader charges of CO_2, H_2, and CO on FeCo(111) surface were -0.85, -0.01, and -0.49, respectively, while the Bader charges of CO_2, H_2, and CO on Co(111) surface were -0.65, -0.01, and -0.39 respectively. Both CO and CO_2 became slightly less negative by 0.10 and 0.20 e^- on the FeCo(111) surface than that on Co(111) surface. These results indicate that the charge on the main reactants of CO_2 hydrogenation increased with the incorporation of Fe on the Co(111) surface. However, there was no change in the Bader charge of H_2 on either Co(111) or FeCo(111) surfaces. The Bader charge for methane increased by 50% with the doping of Fe on the cobalt surface. The highest increase in total Bader charge was calculated for H_2O with a 1400% increase in FeCo(111) surface. In contrast, the charge of H_3COH decreased by 25% on the Fe doped Co(111) surface compared to the pure Co(111) surface. It shows that the presence of Fe on the surface slighly withdrew the electrons from the adsorbed methanol.

The observed increase in the adsorption energy of the species on the FeCo(111) surface is in line with the corresponding increase in the charge on the adsorbates. This

result can be attributed to the presence of Fe atoms which donated electron to adsorbates on the surface. The ability of the absorbates to interact with and withdraw electrons from the Fe atom on the 1 ML FeCo(111) surface contributed to the adsorption process on the surface. As can be seen in Table 5, the sum of total charges of adsorbates on the surfaces and the top two layers were almost zero. This finding implies that the electronic charges play a substantial role on both surfaces, predominantly involving the first two layers. This insight provides valuable information about the relationship between electrostatic interaction of the surface and the adsorption energies of the species.

Table 4. Total Bader charges (q) on adsorbates on Co(111) and FeCo(111) surfaces, along with the calculated difference (Δq).

Adsorbate	**q on Co(111) (e^-)**	**q on FeCo(111) (e^-)**	**Δq (%)**
H	-0.41	-0.49	20
C	-0.90	-1.10	22
O	-1.05	-1.14	9
CO	-0.39	-0.49	26
CO_2	-0.65	-0.85	31
H_2	-0.01	-0.01	0
OH	-0.64	-0.70	9
CH	-0.74	-0.92	24
CH_2	-0.63	-0.77	22
CH_3	-0.43	-0.50	16
CH_4	-0.02	-0.03	50
H_2O	-0.02	-0.30	1400
HCO	-0.76	-0.97	28
COOH	-1.02	-1.30	27
HCOO	-0.57	-0.74	30
H_2CO	-0.69	-0.80	16
H_3CO	-0.63	-0.68	8
H_3COH	-0.04	-0.03	-25

*Negative charge values indicate that charge transfer occurs from surface to the adsorbate.

On the FeCo(111) surface, Fe acted as an electron donor for both the adsorbate and the other cobalt layers of the slab. As illustrated in Table 58, the first layer composed of Fe atoms on FeCo(111) catalyst surface exhibited a significant positive charge compared to the first layer of Co(111) catalyst surface. Furthermore, when the Bader charge values on the top two layers of the monometallic and bimetallic cobalt catalysts were compared with the charges of adsorbates. Moreover, the Fe atoms on the FeCo(111) surface charged

both the adsorbate and other layers on the catalyst, in contrast to Co(111) surface. These findings indicate that Fe played a distinct role as an electron donor on the FeCo(111) surface, exhibiting unique charge distribution characteristics in comparison to the Co(111) surface.

The electronic charges of surfaces without adsorbates derived from DFT calculations were utilized to visualize the electronic charge distribution of the iron additive cobalt catalyst surface in comparison to pure cobalt catalyst surface, as illustrated in Figure 58. These figures were generated using Visualisation of Electronic Structural Analysis (VESTA) software [88]. The yellow color indicates charge accumulation, and the cyan color indicates charge depletion. Based on the pure cobalt surface, Figure 58 shows the charge formed between Fe and Co atoms in the first two layers of Fe addition. It indicated that charge depletion occurred between Fe and Co atoms on the bimetallic FeCo(111) surface when there was no adsorbate on the surface.

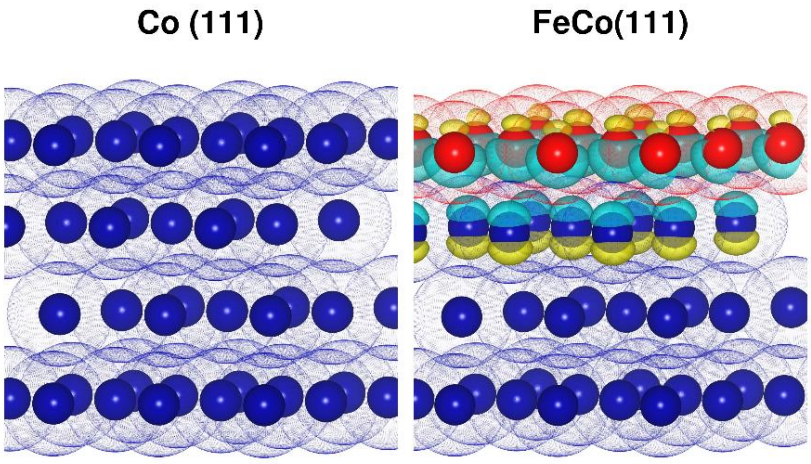

Figure 58. The electronic charge distribution of clean and iron doped (1 ML) cobalt surfaces without adsorbate.

Similarly, the electronic charge distribution for CO adsorbed Co(111) and FeCo(111) surfaces are provided in Figure 59, facilitating an examination of the calculated charge distribution and highlighting the distinctions between pure and iron-doped cobalt surfaces.

Figure 59 demonstrates the charge accumulation occured for CO induced on both Co(111) and FeCo(111) surfaces. This figure illustrates that the CO molecule adsorbed on FeCo(111) surface possessed higher electron density compared to the pure cobalt surface. It demonstrated that the introduction of Fe on Co resulted in an increased accumulation of charge on the CO molecule, as Fe atoms donated its own electrons.

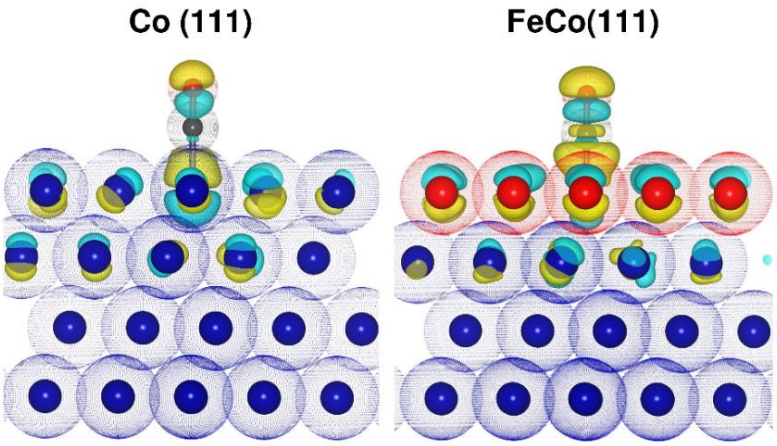

Figure 59. The electronic charge distribution of clean and 1 ML iron-doped cobalt surfaces with adsorbed CO molecule.

The electron donation from Fe atoms to both Co atoms in the second layer and adsorbed species was attributed to Lewis basic character of Fe. To further deepen the understanding of changes in the electronic charge during catalysis, the analysis of electronic charge transfer from Fe atoms to adjacent Co atoms and adsorbates was performed, and these results were presented in Table 5.

Table 5. Electronic charges on Co(111) vs FeCo(111) surfaces under adsorbate coverages.

	Charge (e^-) on Co(111)		**Charge (e^-) on FeCo(111)**		
	Adsorbate	**Co**	**Adsorbate**	**Co**	**Fe**
H	-0.41	0.43	-0.49	-0.46	0.93
C	-0.90	0.90	-1.10	-0.43	1.51
O	-1.05	1.06	-1.14	-0.43	1.55
CO	-0.39	0.40	-0.49	-0.48	0.94
CO_2	-0.65	0.66	-0.85	-0.45	1.27
H_2	-0.01	0.02	-0.01	-0.44	0.43
OH	-0.64	0.65	-0.70	-0.43	1.11
CH	-0.74	0.73	-0.92	-0.46	1.35
CH_2	-0.63	0.63	-0.77	-0.47	1.22
CH_3	-0.43	0.45	-0.50	-0.46	0.94
CH_4	-0.02	0.04	-0.03	-0.44	0.44
H_2O	-0.02	0.03	-0.30	-0.43	0.71
HCO	-0.76	0.77	-0.97	-0.45	1.40
COOH	-1.02	1.04	-1.30	-0.48	1.75
HCOO	-0.57	0.58	-0.74	-0.44	1.16
H_2CO	-0.69	0.70	-0.80	-0.46	1.24
H_3CO	-0.63	0.63	-0.68	-0.43	1.09
H_3COH	-0.04	0.05	-0.03	-0.43	0.44

CHAPTER 5

CONCLUSIONS

A comprehensive investigation of FeCo bimetallic catalysts for CO_2 hydrogenation was conducted using periodic DFT calculations in this study. The aim of the study is to examine the effect of Fe doping on cobalt surfaces and its catalytic performance in the conversion of CO_2 into C_1 products, specifically CH_4, CO, H_2CO, CH_3OH, and H_2O. Based on the experimental literature and our calculations, which are based on enhanced CO adsorption energies, bimetallic FeCo(111) surface is utilized as the bimetallic FeCo catalyst model in DFT calculations to understand its structure-activity relationship for CO_2 hydrogenation. This model represents Fe atoms segregated onto the monometallic cobalt surface in bimetallic FeCo catalysts. In this study, the results on this surface were compared with those on Co(111) surface to perform a comparative analysis.

Based on the results of DFT calculations, Fe doping enhanced the adsorption strength of all surface species. Due to the relatively high adsorption energy of CO_x species, it can be expected that the ratio of adsorbed CO_x/H species on the bimetallic surface will be higher compared to the Co(111) surface. Although the FeCo(111) surface results in decreased activation energies for direct CO_2 dissociation, leading in increased CO and O coverages on the surface, a slight increase in the activation energy for the rate-limiting step could be expected to decrease the overall catalytic activity.

In the context of product selectivity, the FeCo(111) surface slows down the production of hydrogenated products due to their relatively high activation energies and low atomic H coverages. This behaviour is attributed to the high electron-donating ability of Fe atoms to both cobalt atoms and adsorbates. This finding indicates that the electronic charge of the catalyst can be adjusted to obtain a balance between activity of CO_2 and the activation energies for hydrogenation reactions. The enhanced adsorption strength of CO intermediate and high activation energies for CH_4 and H_3COH slow down their selectivities on the bimetallic FeCo(111) surface. Even though these products are experimentally observed in the literature, the results of this study indicate that the (111) facet of FeCo catalysts may not be responsible for their production. Moreover, the inhibition of oxygen removal from the catalyst surface is the main effect of the Fe-doping

on the Co(111) surface during CO_2 hydrogenation. In conclusion, the structural evaluation of bimetallic FeCo surfaces towards iron oxide and mixed iron-cobalt oxide phases can be expected, resulting in a various selectivity characteristic of bimetallic FeCo nanoparticles.

Overall, this thesis provides the first atomic-level insights for the effect of Fe doping on the cobalt surface in terms of the relationship between the structure and activity of the catalyst. These findings are expected to aid in development of high-performance bimetallic catalysts for conversion of CO_2.

The content of this thesis was published under the title “Atomic-Scale Insights into Carbon Dioxide Hydrogenation over Bimetallic Iron–Cobalt Catalysts: A Density Functional Theory Study” in Catalysts (10.3390/catal13111390).

REFERENCES

[1] Shashank Bahri, Anna Maria Venezia, Sreedevi Upadhyayula, Utilization of greenhouse gas carbon dioxide for cleaner Fischer-Tropsch diesel production, *J. Clean. Prod.* 228 (2019) 1013–1024.

[2] R.M. Cuéllar-Franca, A. Azapagic, Carbon capture, storage and utilisation technologies: A critical analysis and comparison of their life cycle environmental impacts, *J. CO_2 Util*. 9 (2015) 82–102. https://doi.org/10.1016/j.jcou.2014.12.001.

[3] M. Takht Ravanchi, S. Sahebdelfar, Catalytic conversions of CO_2 to help mitigate climate change: Recent process developments, *Process Saf. Environ. Prot.* 145 (2021) 172–194. https://doi.org/10.1016/j.psep.2020.08.003.

[4] B.Y.R. Monastersky, Global carbon dioxide levels near worrisome milestone, *Nature.* 497 (2013). https://doi.org/10.1038/497013a.

[5] Y.H. Choi, Y.J. Jang, H. Park, W.Y. Kim, Y.H. Lee, S.H. Choi, J.S. Lee, Carbon dioxide Fischer-Tropsch synthesis: A new path to carbon-neutral fuels, *Appl. Catal. B Environ*. 202 (2017) 605–610. https://doi.org/10.1016/j.apcatb.2016.09.072.

[6] M.D. Porosoff, J.G. Chen, Trends in the catalytic reduction of CO_2 by hydrogen over supported monometallic and bimetallic catalysts, *J. Catal.* 301 (2013) 30–37. https://doi.org/10.1016/j.jcat.2013.01.022.

[7] S. De, A. Dokania, A. Ramirez, J. Gascon, Advances in the Design of Heterogeneous Catalysts and Thermocatalytic Processes for CO_2 Utilization, *ACS Catal.* 10 (2020) 14147–14185. https://doi.org/10.1021/acscatal.0c04273.

[8] Y. Wang, D. He, H. Chen, D. Wang, Catalysts in electro-, photo- and photoelectrocatalytic CO_2 reduction reactions, *J. Photochem. Photobiol. C Photochem. Rev*. 40 (2019) 117–149. https://doi.org/10.1016/j.jphotochemrev.2019.02.002.

[9] T. Taseska, W. Yu, M.K. Wilsey, C.P. Cox, Z. Meng, S.S. Ngarnim, A.M. Müller, Analysis of the Scale of Global Human Needs and Opportunities for Sustainable Catalytic Technologies, *Top. Catal.* 66 (2023) 338–374. https://doi.org/10.1007/s11244-023-01799-3.

[10] E. Alper, O. Yuksel Orhan, CO_2 utilization: Developments in conversion processes, *Petroleum*. 3 (2017) 109–126. https://doi.org/10.1016/j.petlm.2016.11.003.

[11] C. Liu, T.R. Cundari, A.K. Wilson, CO_2 reduction on transition metal (Fe, Co, Ni, and Cu) surfaces: In comparison with homogeneous catalysis, *J. Phys. Chem. C.* 116 (2012) 5681–5688. https://doi.org/10.1021/jp210480c.

[12] C.H. Bartholomew, Fundamentals of Industrial Catalytic Processes, 2nd edn (2015).

[13] M. Aresta, A. Dibenedetto, E. Quaranta, State of the art and perspectives in catalytic processes for CO_2 conversion into chemicals and fuels : The distinctive contribution of chemical catalysis and biotechnology, *J. Catal.* 343 (2016) 2–45. https://doi.org/10.1016/j.jcat.2016.04.003.

[14] S. Roy, A. Cherevotan, S.C. Peter, Thermochemical CO_2 Hydrogenation to Single Carbon Products: Scientific and Technological Challenges, *ACS Energy Lett.* 3 (2018) 1938–1966. https://doi.org/10.1021/acsenergylett.8b00740.

[15] R.P. Ye, J. Ding, W. Gong, M.D. Argyle, Q. Zhong, Y. Wang, C.K. Russell, Z. Xu, A.G. Russell, Q. Li, M. Fan, Y.G. Yao, CO_2 hydrogenation to high-value products via heterogeneous catalysis, *Nat. Commun.* 10 (2019). https://doi.org/10.1038/s41467-019-13638-9.

[16] E.C. Ra, K.Y. Kim, E.H. Kim, H. Lee, K. An, J.S. Lee, Recycling Carbon Dioxide through Catalytic Hydrogenation: Recent Key Developments and Perspectives, *ACS Catal.* 10 (2020) 11318–11345. https://doi.org/10.1021/acscatal.0c02930.

[17] Y.J. Wong, H.H. Halim, N.F. Khairudin, T.N. Pham, S.E.M. Putra, Y. Hamamoto, K. Inagaki, I. Hamada, A.R. Mohamed, Y. Morikawa, Dry Reforming of Methane on Cobalt Catalysts: DFT-Based Insights into Carbon Deposition Versus Removal, *J. Phys. Chem.* C. 125 (2021) 21902–21913. https://doi.org/10.1021/acs.jpcc.1c04819.

[18] K. Zhao, M. Calizzi, E. Moioli, M. Li, A. Borsay, L. Lombardo, R. Mutschler, W. Luo, A. Züttel, Unraveling and optimizing the metal-metal oxide synergistic effect in a highly active $Co_x(CoO)_{1-x}$ catalyst for CO_2 hydrogenation, *J. Energy Chem.* 53 (2020) 241–250. https://doi.org/10.1016/j.jechem.2020.05.025.

[19] X. Fan, Z. Liu, Y.A. Zhu, G. Tong, J. Zhang, C. Engelbrekt, J. Ulstrup, K. Zhu, X. Zhou, Tuning the composition of metastable $Co_xNi_yMg_{100-x-y}(OH)(OCH_3)$ nanoplates for optimizing robust methane dry reforming catalyst, *J. Catal.* 330 (2015) 106–119. https://doi.org/10.1016/j.jcat.2015.06.018.

[20] Y. Liu, Y. Chen, H. Yu, F. Guan, Z. Hou, D. Cui, Y. Zhang, Bimetallic Ni-Co catalysts for co-production of methane and liquid fuels from syngas, *Catal. Today.* 369 (2021) 167–174. https://doi.org/10.1016/j.cattod.2020.05.011.

[21] J. Sehested, K.E. Larsen, A.L. Kustov, A.M. Frey, T. Johannessen, T. Bligaard, M.P. Andersson, J.K. Nørskov, C.H. Christensen, Discovery of technical methanation catalysts based on computational screening, *Top. Catal.* 45 (2007) 9–13. https://doi.org/10.1007/s11244-007-0232-9.

[22] P. Sebastián-Pascual, I. Jordão Pereira, M. Escudero-Escribano, Tailored electrocatalysts by controlled electrochemical deposition and surface nanostructuring, *Chem. Commun.* 56 (2020) 13261–13272. https://doi.org/10.1039/d0cc06099b.

[23] J.A. Keith, V. Vassilev-Galindo, B. Cheng, S. Chmiela, M. Gastegger, K.R. Müller, A. Tkatchenko, Combining Machine Learning and Computational Chemistry for Predictive Insights into Chemical Systems, *Chem. Rev*. 121 (2021) 9816–9872. https://doi.org/10.1021/acs.chemrev.1c00107.

[24] H. Jahangiri, J. Bennett, P. Mahjoubi, K. Wilson, S. Gu, A review of advanced catalyst development for Fischer-Tropsch synthesis of hydrocarbons from biomass derived syn-gas, *Catal. Sci. Technol.* 4 (2014) 2210–2229. https://doi.org/10.1039/c4cy00327f.

[25] A. V. Puga, On the nature of active phases and sites in CO and CO_2 hydrogenation catalysts, *Catal. Sci. Technol.* 8 (2018) 5681–5707. https://doi.org/10.1039/c8cy01216d.

[26] M. Tavares, G. Westphalen, J.M. Araujo Ribeiro de Almeida, P.N. Romano, E.F. Sousa-Aguiar, Modified fischer-tropsch synthesis: A review of highly selective catalysts for yielding olefins and higher hydrocarbons, *Front. Nanotechnol.* 4 (2022). https://doi.org/10.3389/fnano.2022.978358.

[27] A.H. Hatta, A.A. Jalil, N.S. Hassan, M.Y.S. Hamid, A.F.A. Rahman, L.P. Teh, D.

Prasetyoko, A review on recent bimetallic catalyst development for synthetic natural gas production via CO methanation, *Int. J. Hydrogen Energy*. 47 (2022) 30981–31002. https://doi.org/10.1016/j.ijhydene.2021.10.213.

[28] T. Lin, F. Yu, Y. An, T. Qin, L. Li, K. Gong, L. Zhong, Y. Sun, Cobalt Carbide Nanocatalysts for Efficient Syngas Conversion to Value-Added Chemicals with High Selectivity, *Acc. Chem. Res*. 54 (2021) 1961–1971. https://doi.org/10.1021/acs.accounts.0c00883.

[29] K.T. Rommens, M. Saeys, Molecular Views on Fischer-Tropsch Synthesis, *Chem. Rev.* (2022). https://doi.org/10.1021/acs.chemrev.2c00508.

[30] Sonal, E. Ahmad, S. Upadhyayula, K.K. Pant, Biomass-derived CO_2 rich syngas conversion to higher hydrocarbon via Fischer-Tropsch process over Fe–Co bimetallic catalyst, *Int. J. Hydrogen Energy*. 44 (2019) 27741–27748. https://doi.org/10.1016/j.ijhydene.2019.09.015.

[31] J. Van de Loosdrecht, F.G. Botes, I.M. Ciobica, A. Ferreira, P. Gibson, D.J. Moodley, A.M. Saib, J.L. Visagie, C.J. Weststrate, J.W. Niemantsverdriet, Fischer-Tropsch Synthesis: Catalysts and Chemistry, Elsevier Ltd., 2013. https://doi.org/10.1016/B978-0-08-097774-4.00729-4.

[32] I.C. ten Have, B.M. Weckhuysen, The active phase in cobalt-based Fischer-Tropsch synthesis, *Chem Catal*. 1 (2021) 339–363. https://doi.org/10.1016/j.checat.2021.05.011.

[33] D.B. Bukur, B. Todic, N. Elbashir, Role of water-gas-shift reaction in Fischer–Tropsch synthesis on iron catalysts: A review, *Catal. Today*. 275 (2016) 66–75. https://doi.org/10.1016/j.cattod.2015.11.005.

[34] L. Zhang, Y. Dang, X. Zhou, P. Gao, A. Petrus van Bavel, H. Wang, S. Li, L. Shi, Y. Yang, E.I. Vovk, Y. Gao, Y. Sun, Direct conversion of CO_2 to a jet fuel over CoFe alloy catalysts, *Innovation*. 2 (2021) 100170. https://doi.org/10.1016/j.xinn.2021.100170.

[35] X. Nie, H. Wang, M.J. Janik, Y. Chen, X. Guo, C. Song, Mechanistic Insight into C-C Coupling over Fe-Cu Bimetallic Catalysts in CO_2 Hydrogenation, *J. Phys. Chem. C.* 121 (2017) 13164–13174. https://doi.org/10.1021/acs.jpcc.7b02228.

[36] A.I. Tsiotsias, N.D. Charisiou, I. V. Yentekakis, M.A. Goula, Bimetallic ni-based catalysts for CO_2 methanation: A review, *Nanomaterials.* 11 (2021) 1–34. https://doi.org/10.3390/nano11010028.

[37] C. Perego, R. Bortolo, R. Zennaro, Gas to liquids technologies for natural gas reserves valorization : The Eni experience, *Catal. Today*. 142 (2009) 9–16. https://doi.org/10.1016/j.cattod.2009.01.006.

[38] M. V. Landau, N. Meiri, N. Utsis, R. Vidruk Nehemya, M. Herskowitz, Conversion of CO_2, CO, and H_2 in CO_2 Hydrogenation to Fungible Liquid Fuels on Fe-Based Catalysts, *Ind. Eng. Chem. Res.* 56 (2017) 13334–13355. https://doi.org/10.1021/acs.iecr.7b01817.

[39] T. Riedel, G. Schaub, K.W. Jun, K.W. Lee, Kinetics of CO_2 hydrogenation on a K-promoted Fe catalyst, *Ind. Eng. Chem. Res.* 40 (2001) 1355–1363. https://doi.org/10.1021/ie000084k.

[40] C.G. Visconti, M. Martinelli, L. Falbo, L. Fratalocchi, L. Lietti, CO_2 hydrogenation to hydrocarbons over Co and Fe-based Fischer-Tropsch catalysts, *Catal. Today*. 277 (2016) 161–170. https://doi.org/10.1016/j.cattod.2016.04.010.

[41] N. Utsis, R. Vidruk-Nehemya, M. V. Landau, M. Herskowitz, Novel bifunctional catalysts based on crystalline multi-oxide matrices containing iron ions for CO_2 hydrogenation to liquid fuels and chemicals, *Faraday Discuss.* 188 (2016) 545–563. https://doi.org/10.1039/c5fd00174a.

[42] M.K. Gnanamani, H.H. Hamdeh, W.D. Shafer, D.E. Sparks, B.H. Davis, Fischer-tropsch synthesis: Effect of potassium on activity and selectivity for oxide and carbide Fe catalysts, *Catal. Letters.* 143 (2013) 1123–1131. https://doi.org/10.1007/s10562-013-1110-7.

[43] Isa Shahroudbari, Y. Sarrafi, Y. Zamani, Study of Carbon Dioxide Hydrogenation to Hydrocarbons Over Iron-Based Catalysts: Synergistic Effect, *Catal. Ind.* 13 (2021) 317–324. https://doi.org/10.1134/S2070050421040085.

[44] T. Numpilai, T. Witoon, N. Chanlek, W. Limphirat, G. Bonura, M. Chareonpanich, J. Limtrakul, Structure–activity relationships of Fe-Co/K-Al_2O_3 catalysts calcined at different temperatures for CO_2 hydrogenation to light olefins, *Appl. Catal. A Gen.* 547 (2017) 219–229. https://doi.org/10.1016/j.apcata.2017.09.006.

[45] Y. Daga, A.C. Kizilkaya, Mechanistic Insights into the Effect of Sulfur on the Selectivity of Cobalt-Catalyzed Fischer–Tropsch Synthesis: A DFT Study, *Catalysts.* 12 (2022). https://doi.org/10.3390/catal12040425.

[46] S. Govender, T.G. Gambu, T. van Heerden, E. van Steen, Mechanistic pathways for oxygen removal on Pt-doped Co(111) in the Fischer-Tropsch reaction, *Catal. Today.* 342 (2020) 142–151. https://doi.org/10.1016/j.cattod.2019.02.001.

[47] M. Wang, G. Zhang, J. Zhu, W. Li, J. Wang, K. Bian, Y. Liu, F. Ding, C. Song, X. Guo, Unraveling the tunable selectivity on cobalt oxide and metallic cobalt sites for CO_2 hydrogenation, *Chem. Eng. J.* 446 (2022) 137217. https://doi.org/10.1016/j.cej.2022.137217.

[48] V.R. Calderone, N.R. Shiju, D. Curulla-ferrø, S. Chambrey, A. Khodakov, A. Rose, J. Thiessen, A. Jess, G. Rothenberg, De Novo Design of Nanostructured Iron–Cobalt Fischer–Tropsch Catalysts, *Angew. Chem.* (2013) 4397–4401. https://doi.org/10.1002/anie.201209799.

[49] C.F. Toncón-Leal, J.F. Múnera, J.J. Arroyo-Gómez, K. Sapag, Fe, Co and Fe/Co catalysts supported on SBA-15 for Fischer-Tropsch Synthesis, *Catal. Today.* 394–396 (2022) 150–160. https://doi.org/10.1016/j.cattod.2021.07.023.

[50] A. Griboval-constant, A. Butel, V. V Ordomsky, P.A. Chernavskii, A.Y. Khodakov, Cobalt and iron species in alumina supported bimetallic catalysts for Fischer – Tropsch reaction, *Appl. Catal. A, Gen.* 481 (2014) 116–126. https://doi.org/10.1016/j.apcata.2014.04.047.

[51] M.K. Gnanamani, G. Jacobs, H.H. Hamdeh, W.D. Shafer, F. Liu, S.D. Hopps, G.A. Thomas, B.H. Davis, Hydrogenation of Carbon Dioxide over Co-Fe Bimetallic Catalysts, *ACS Catal.* 6 (2016) 913–927. https://doi.org/10.1021/acscatal.5b01346.

[52] B.W.J. Chen, L. Xu, M. Mavrikakis, Computational Methods in Heterogeneous Catalysis, *Chem. Rev.* 121 (2021) 1007–1048. https://doi.org/10.1021/acs.chemrev.0c01060.

[53] A.J. Cohen, P. Mori-s, W. Yang, Challenges for Density Functional Theory, *Chem. Rev.* 112 (2012) 289–320.

[54] W. Kohn, L.J. Sham, Self-Consistent Equations Including Exchange and

Correlation Effects, *Phys. Rev.* 140 (1965) 1113–1138.

[55] M. Cafiero, L. Adamowicz, Molecular structure in non-Born-Oppenheimer quantum mechanics, *Chem. Phys. Lett.* 387 (2004) 136–141. https://doi.org/10.1016/j.cplett.2004.02.006.

[56] G. Kresse, J. Furthmüller, Efficient iterative schemes for ab initio total-energy calculations using a plane-wave basis set, *Phys. Rev. B.* 54 (1996) 11169–11186. https://doi.org/10.1103/PhysRevB.54.11169.

[57] P.E. Blöchl, Projector augmented-wave method, *Phys. Rev. B.* 50 (1994) 17953–17979. https://doi.org/10.1103/PhysRevB.50.17953.

[58] G. Henkelman, B.P. Uberuaga, H. Jónsson, Climbing image nudged elastic band method for finding saddle points and minimum energy paths, J. Chem. Phys. 113 (2000) 9901–9904. https://doi.org/10.1063/1.1329672.

[59] J.-X. Liu, H.-Y. Su, D.-P. Sun, B.-Y. Zhang, W.-X. Li, Crystallographic Dependence of CO Activation on Cobalt Catalysts: HCP versus FCC Supporting Information, *J. Am. Chem. Soc.* 135 (2013) 16284−16287.

[60] S. Mourdikoudis, K. Simeonidis, M. Angelakeris, I. Tsiaoussis, O. Kalogirou, C. Desvaux, C. Amiens, B. Chaudret, Effect of air exposure on structural and magnetic features of FeCo nanoparticles, *Mod. Phys. Lett. B.* 21 (2007) 1161–1168. https://doi.org/10.1142/S0217984907013869.

[61] G.Y. and N.T. Yanbing Li, Yingluo He , Kensei Fujihara, Chengwei Wang, Xu Sun, Weizhe Gao, Xiaoyu Guo, Shuhei Yasuda, A Core-Shell Structured Na/Fe@Co Bimetallic Catalyst for Light-Hydrocarbon Synthesis from CO_2 Hydrogenation, *J. Catal.* 13 (2023) 1090.

[62] N. Eom, M.E. Messing, J. Johansson, K. Deppert, General Trends in Core-Shell Preferences for Bimetallic Nanoparticles, *ACS Nano.* 15 (2021) 8883–8895. https://doi.org/10.1021/acsnano.1c01500.

[63] A.S. Sandupatla, A. Banerjee, G. Deo, Optimizing CO2 hydrogenation to methane over CoFe bimetallic catalyst: Experimental and density functional theory studies, *Appl. Surf. Sci.* 485 (2019) 441–449. https://doi.org/10.1016/j.apsusc.2019.04.217.

[64] A.S.M. Ismail, M. Casavola, B. Liu, A. Gloter, T.W. Van Deelen, M. Versluijs, J.D.

Meeldijk, O. Stéphan, K.P. De Jong, F.M.F. De Groot, Atomic-Scale Investigation of the Structural and Electronic Properties of Cobalt-Iron Bimetallic Fischer-Tropsch Catalysts, *ACS Catal.* 9 (2019) 7998–8011. https://doi.org/10.1021/acscatal.8b04334.

[65] W. Wang, E. Toshcheva, A. Ramirez, G. Shterk, R. Ahmad, M. Caglayan, J.L. Cerrillo, A. Dokania, G. Clancy, T.B. Shoinkhorova, N. Hijazi, L. Cavallo, J. Gascon, Bimetallic Fe-Co catalysts for the one step selective hydrogenation of CO_2 to liquid hydrocarbons, *Catal. Sci. Technol.* 13 (2023) 1527–1540. https://doi.org/10.1039/d2cy01880b.

[66] P. Rochana, J. Wilcox, A theoretical study of CO adsorption on FeCo(100) and the effect of alloying, *Surf. Sci.* 605 (2011) 681–688. https://doi.org/10.1016/j.susc.2011.01.003.

[67] A. Tavasoli, M. Trépanier, R.M. Malek Abbaslou, A.K. Dalai, N. Abatzoglou, Fischer-Tropsch synthesis on mono- and bimetallic Co and Fe catalysts supported on carbon nanotubes, *Fuel Process. Technol.* 90 (2009) 1486–1494. https://doi.org/10.1016/j.fuproc.2009.07.007.

[68] D.J. Duvenhage, N.J. Coville, Fe:Co/TiO_2 bimetallic catalysts for the Fischer-Tropsch reaction: Part 3: The effect of Fe:Co ratio, mixing and loading on FT product selectivity, *Appl. Catal. A Gen.* 289 (2005) 231–239. https://doi.org/10.1016/j.apcata.2005.05.008.

[69] R.W. Dorner, D.R. Hardy, F.W. Williams, B.H. Davis, H.D. Willauer, Influence of gas feed composition and pressure on the catalytic conversion of CO_2 to hydrocarbons using a traditional cobalt-Based fischer-Tropsch catalyst, *Energy and Fuels.* 23 (2009) 4190–4195. https://doi.org/10.1021/ef900275m.

[70] R. Satthawong, N. Koizumi, C. Song, P. Prasassarakich, Bimetallic Fe-Co catalysts for CO_2 hydrogenation to higher hydrocarbons, *J. CO_2 Util.* 3–4 (2013) 102–106. https://doi.org/10.1016/j.jcou.2013.10.002.

[71] R. Satthawong, N. Koizumi, C. Song, P. Prasassarakich, Light olefin synthesis from CO_2 hydrogenation over K-promoted Fe-Co bimetallic catalysts, *Catal. Today.* 251 (2015) 34–40. https://doi.org/10.1016/j.cattod.2015.01.011.

[72] G. Kresse, J. Hafner, Ab-initio molecular dynamics for liquid metals, *Phys. Rev. B.*

47 (1993) 558–561. https://doi.org/10.1103/PhysRevB.47.558.

[73] Y. Zhang, W. Yang, Comment on "generalized gradient approximation made simple," *Phys. Rev. Lett.* 80 (1998) 890. https://doi.org/10.1103/PhysRevLett.80.890.

[74] G.T.K.K. Gunasooriya, A.P. Van Bavel, H.P.C.E. Kuipers, M. Saeys, CO adsorption on cobalt: Prediction of stable surface phases, *Surf. Sci.* 642 (2015) L6–L10. https://doi.org/10.1016/j.susc.2015.06.024.

[75] J.D. Pack, H.J. Monkhorst, Special points for Brillouin-zone integrations, *Phys. Rev. B.* 16 (1977) 1748–1749. https://doi.org/10.1103/PhysRevB.16.1748.

[76] P. Van Helden, I.M. Ciobîcə, R.L.J. Coetzer, The size-dependent site composition of FCC cobalt nanocrystals, *Catal. Today.* 261 (2016) 48–59. https://doi.org/10.1016/j.cattod.2015.07.052.

[77] S. Amaya-Roncancio, D.H. Linares, H.A. Duarte, K. Sapag, DFT Study of Hydrogen-Assisted Dissociation of CO by HCO, COH, and HCOH Formation on Fe(100), *J. Phys. Chem. C.* 120 (2016) 10830–10837. https://doi.org/10.1021/acs.jpcc.5b12014.

[78] S.H. Ma, Z.Y. Jiao, T.X. Wang, X.Q. Dai, Ab initio study on the adsorption of oxygen on Co(111) and its subsurface incorporation, *Eur. Phys. J. B.* 88 (2015) 2–9. https://doi.org/10.1140/epjb/e2014-50292-0.

[79] K. Jeske, A.C. Kizilkaya, I. López-Luque, N. Pfänder, M. Bartsch, P. Concepción, G. Prieto, Design of Cobalt Fischer-Tropsch Catalysts for the Combined Production of Liquid Fuels and Olefin Chemicals from Hydrogen-Rich Syngas, *ACS Catal.* 11 (2021) 4784–4798. https://doi.org/10.1021/acscatal.0c05027.

[80] B. Zijlstra, R.J.P. Broos, W. Chen, G.L. Bezemer, I.A.W. Filot, E.J.M. Hensen, The vital role of step-edge sites for both CO activation and chain growth on cobalt fischer-tropsch catalysts revealed through first-principles-based microkinetic modeling including lateral interactions, *ACS Catal.* 10 (2020) 9376–9400.

[81] H. Huang, Y. Yu, M. Zhang, Mechanistic insight into methane dry reforming over cobalt: A density functional theory study, *Phys. Chem. Chem. Phys.* 22 (2020) 27320–27331. https://doi.org/10.1039/c9cp07003f.

[82] S. Chen, J. Zaffran, B. Yang, Dry reforming of methane over the cobalt catalyst: Theoretical insights into the reaction kinetics and mechanism for catalyst deactivation, *Appl. Catal. B Environ.* 270 (2020). https://doi.org/10.1016/j.apcatb.2020.118859.

[83] W. Luo, A. Asthagiri, Density functional theory study of methanol steam reforming on Co(0001) and Co(111) surfaces, *J. Phys. Chem. C.* 118 (2014) 15274–15285. https://doi.org/10.1021/jp503177h.

[84] A.C. Kizilkaya, J.W. Niemantsverdriet, C.J. Weststrate, Oxygen Adsorption and Water Formation on Co(0001), *J. Phys. Chem. C.* 120 (2016) 4833–4842. https://doi.org/10.1021/acs.jpcc.5b08959.

[85] C.J. Weststrate, D. Sharma, D.G. Rodríguez, H.O.A. Fredriksson, J.W. Niemantsverdriet, Water Formation Kinetics on Co(0001) at Low and Near-Ambient Hydrogen Pressures in the Context of Fischer-Tropsch Synthesis, *J. Phys. Chem. C.* (2022). https://doi.org/10.1021/acs.jpcc.2c08092.

[86] D. Santos-Carballal, A. Cadi-Essadek, N.H. de Leeuw, Catalytic Conversion of CO and H_2 into Hydrocarbons on the Cobalt Co(111) Surface: Implications for the Fischer-Tropsch Process, *J. Phys. Chem. C.* 125 (2021) 11891–11903. https://doi.org/10.1021/acs.jpcc.1c00254.

[87] B. Liu, W. Li, Y. Xu, Q. Lin, F. Jiang, X. Liu, Insight into the Intrinsic Active Site for Selective Production of Light Olefins in Cobalt-Catalyzed Fischer-Tropsch Synthesis, *ACS Catal.* 9 (2019) 7073–7089. https://doi.org/10.1021/acscatal.9b00352.

[88] K. Momma, F. Izumi, VESTA: A three-dimensional visualization system for electronic and structural analysis, *J. Appl. Crystallogr.* 41 (2008) 653–658. https://doi.org/10.1107/S0021889808012016.

[89] G.T.K.K. Gunasooriya, A.P. Van Bavel, H.P.C.E. Kuipers, M. Saeys, Key Role of Surface Hydroxyl Groups in C-O Activation during Fischer-Tropsch Synthesis, *ACS Catal.* 6 (2016) 3660–3664. https://doi.org/10.1021/acscatal.6b00634.

[90] C. Chen, Q. Wang, G. Wang, B. Hou, L. Jia, D. Li, Mechanistic insight into the C_2 hydrocarbons formation from Syngas on fcc-Co(111) surface: A DFT study, *J. Phys. Chem. C.* 120 (2016) 9132–9147. https://doi.org/10.1021/acs.jpcc.5b09634.

APPENDIX A

GAS PHASE ENERGIES

Table 6. Gas phase energies for various adsorption species.

Species	Bare Energy (eV)
CO_2	-17.14
CO	-11.35
H_2	-7.06
H_2O	-12.20
CH_4	-22.59
H_3COH	-26.60
COOH	-18.61
HCOO	-18.32
HCO	-13.53

APPENDIX B

COMPARISON OF ADSORPTION ENERGIES ON COBALT SURFACES

Table 7. Comparison of the adsorption energies ($kJ.mol^{-1}$) of the adsorbates examined on the surface of the Co(111) catalyst in the literature.

Adsorbate	**Co(111)[a]**	**Co(111)[b]**	**Co(0001)[c]**
H	-278 (fcc)	-270 (fcc)	-288 (fcc)
C	-633 (hcp)	-614 (hcp)	-705 (hcp)
O	-556 (hcp)	-539 (hcp)	-602 (hcp)
CO	-132 (top)	-130 (top)	-184 (hcp)
CO_2	-19 (bridge via C)	-16	-2
H_2	-6 (top)	NA	-45 (top)
OH	-329 (hcp)	-327 (hcp)	-354 (hcp)
CH	-561 (hcp)	-597 (hcp)	-665 (hcp)
CH_2	-362 (fcc)	-385 (hcp)	-421 (hcp)
CH_3	-166 (hcp)	-211 (hcp)	-228 (hcp)
CH_4	-13.5 (top)	NA	-6 (top)
H_2O	-28 (top)	-30 (top)	-42 (top)
HCO	-187 (hcp via O and C)	-174 (fcc)	-243 (hcp via O and C)
COOH	-211 (bridge via C)	NA	-223 (bridge via C)
HCOO	-311 (bridge via C)	NA	-252 (bridge via C)
H_2CO	-58 (fcc via O)	-35 (top via O)	-96 (hcp via O)
H_3CO	-284 (hcp)	NA	-303 (hcp)
H_3COH	-39 (top via O)	NA	-35 (top via O)

[a] This study.
[b] [89]
[c] [90]

APPENDIX C

COMPARISON OF ACTIVATION AND REACTION ENERGIES ON COBALT SURFACES

Table 8. Comparison of the activation energies and reaction energies ($kJ.mol^{-1}$) of the reactions examined on the surface of the Co(111) catalyst in the literature.

Elementary Reaction	E_a			ΔE		
	Co(111)[a]	Co(111)[b]	Co(111)[c]	Co(111)[a]	Co(111)[b]	Co(111)[c]
$H_2 \rightarrow H_2$	26	NA	NA	13	NA	NA
$H_2 \rightarrow H + H$	28	NA	NA	-59	NA	NA
$CO_2 \rightarrow CO + O$	61	20[f]	50[e]	-77	-111[f]	-90[e]
$CO_2 + H \rightarrow COOH$	94	NA	136[e]	-18	NA	24[e]
$COOH \rightarrow CO + OH$	NA	NA	58[e]	NA	NA	-110[e]
$CO_2 + H \rightarrow HCOO$	71	NA	82[e]	-74	NA	-40[e]
$HCOO \rightarrow HCO + O$	NA	NA	112[e]	NA	NA	58[e]
$CO \rightarrow C + O$	276	235	238	100	NA	106
$CO + H \rightarrow HCO$	111	143 (125[f])	91 (125[e])	96	(111[f])	80 (109[e])
$HCO \rightarrow CH + O$	75	58	87 (71[e])	-43	NA	-35 (-58[e])
$O + H \rightarrow OH$	124	121 (131[f])	99[d]	6	(20[f])	10[d]
$OH + H \rightarrow H_2O$	153	147 (146[f])	114[d]	44	(57[f])	30[d]
$OH + OH \rightarrow H_2O$	48	75 (30[f])	27[d]	2	(-11[f])	-17[d]
$C + H \rightarrow CH$	68	NA	84[e]	-49	NA	-39[e]
$CH + H \rightarrow CH_2$	48	NA	60[e]	12	NA	23[e]
$CH_2 + H \rightarrow CH_3$	45	NA	53[e]	-39	NA	-36[e]
$CH_3 + H \rightarrow CH_4$	90	NA	92[e]	-52	NA	-25[e]
$HCO + H \rightarrow H_2CO$	44	45 (46[f])	25 (42[e])	2	(24[f])	5 (8[e])
$CH_2 + O \rightarrow H_2CO$	124	NA	197 (124[e])	48	NA	55 (43[e])
$H_2CO \rightarrow CH_2 + O$	76	41	142	-48	NA	-55
$H_2CO + H \rightarrow H_3CO$	42	(37[f])	NA	-83	(-56[f])	NA
$CH_3 + O \rightarrow H_3CO$	141	NA	156[e]	-4	NA	8[e]
$H_3CO + H \rightarrow H_3COH$	160	140[f]	164[e]	56	57[f]	62[e]
$CH_3 + OH \rightarrow H_3COH$	196	NA	212[e]	42	NA	65[e]